Study and design of process parameters for additive manufacturing of PEEK and C-PEEK parts for aeronautical applications

Politecnico di Bari

Department of Mechanics, Mathematics and Management

Ph.D. Program

SSD: ING-IND/16–TECHNOLOGIES AND MANUFACTURING SYSTEMS

Final Dissertation

Study and design of process parameters for additive manufacturing of PEEK and C-PEEK parts for aeronautical applications

---

by

Triminì Valentina

Supervisors:

Prof. Gianluca Percoco

Ing. Stefano Giuseppe Corvaglia

Co-supervisor:

Dott.ssa Sara Varetti

Coordinator of Ph.D. Program:

Prof. Giuseppe Casalino

Course 37, 01/11/2021-31/10/2024

Politecnico di Bari

Department of Mechanics, Mathematics and Management
MECHANICAL AND MANAGEMENT ENGINEERING

Ph.D. Program

SSD: ING-IND/16–TECHNOLOGIES AND MANUFACTURING SYSTEMS

Final Dissertation

Study and design of process parameters for additive manufacturing of PEEK and C-PEEK parts for aeronautical applications

---

by

Triminì Valentina :

Referees:

Prof. Eric MacDonald

Prof. Douglas Smith

Supervisors:

Prof. Gianluca Percoco

Ing. Stefano Giuseppe Corvaglia

Coordinator of Ph.D Program:

Prof. Giuseppe Casalino

Course n°37, 01/11/2021-31/10/2024

Preface

The Ph.D. thesis presented was carried out in collaboration with Leonardo S.p.A., Aerostructures Division, of based in Grottaglie (TA) and with the "Interdisciplinary Additive Manufacturing (IAM) Lab" of Politecnico di Bari, based in Taranto.

The results of the research has been published in four papers in international journals and conferences , in which the candidate is author.

- "Influence of Process Parameters of 3D Printed PEEK on Crystallinity and Mechanical Performances" Triminì, V., Varetti, S., Percoco, G., Corvaglia, S., Gallo, N., Scavo, I. (2023). In: Lopresto, V., Papa, I., Langella, A. (eds) Dynamic Response and Failure of Composite Materials. DRAF 2022. Lecture Notes in Mechanical Engineering. Springer, Cham.

- "Evaluation of the influence of process parameters on crystallinity and tensile strength of 3D printed PEEK parts" Triminì, V., Varetti, S., Percoco, G., Corvaglia, S.G., Gallo, N., Scavo, I., Proceedings of the Institution of Mechanical Engineers, Part C: Journal of Mechanical Engineering Science. 2023

- "Compressive strength behavior of gyroid lattice structures in 3D-printed CF-PEEK" Triminì, V., Varetti, S., Percoco, G., Corvaglia, S.G., Scavo, I., Gallo, N., Book of Abstracts, (p. 98) of the ICSAAM23 Conference, 2023

- "Investigation of compressive isotropy in 3D printed C-PEEK gyroid structures" Triminì, V., Varetti, S., Corvaglia, S.G., Gallo, N., Percoco, G., Proceedings of the SAMPE Europe Conference, 2024

During the PhD period, two other publications were made, whose content is not part of the present dissertation.

- "Study on the influence of process parameters on surface properties of additively manufactured parts" Varetti, S., Boccaccio, M., Triminì, V., Scavo, I., Flora, F., Acerra, F. and Corvaglia, S. G., Proceedings of the ICCM23 Conference, 2023

- "Low-cost method to reduce interlayer voids in Material Extrusion: in situ layer-by-layer solvent application" Saqlain Iqbal, M., Stano, G., Triminì, V., Percoco, G., The International Journal of Advanced Manufacturing Technology, Volume 133, pages 5333–5342, 2024

Abstract

The growing need for more sustainable solutions has led research in the aeronautical and aerospace fields to the production of increasingly lighter and more efficient aircraft. For lightening purposes, advanced composite materials made of carbon fibers and epoxy resins were developed. Nevertheless, the use of thermoplastics as a valid alternative to thermosets, has the advantage of being easily processable, repairable and recyclable. The most interesting thermoplastic materials for the aerospace industry are the so-called " technopolymers", such as polyariletherketones (PAEK) family, which combine high mechanical, thermal and chemical resistance with very low weight. One of the most sustainable ways to process these materials are Additive Manufacturing technologies (AM), and in particular the Fused Filament Fabrication (FFF) technique.

The present work is an in-depth study on the optimization of FFF process parameters and possible strategies aimed at resolving the technological limitations for the printing of Polyether-ether ketone (PEEK) and Carbon-PEEK parts making them usable for lightening purposes in the aeronautical sector.

In the first part of the study, the optimal process conditions for the 3D printing of 100% dense PEEK parts are found by characterizing both mechanical and structural properties of printed coupons. It was discovered that the mechanical performances are strongly dependent on PEEK degree of crystallinity. Therefore, by varying the process temperatures and the printing speed, it is possible to control the crystallization, customizing the mechanical properties and possible applications.

Subsequently, the research activity was focused on the enhancement of the interlayer adhesion in 3D printed parts by means of atmospheric plasma superficial treatments. The study was carried out on both Polycarbonate (PC) and PEEK because they have very similar features and processing issues. The choice of treatment parameters was made by studying the plasma-induced improvement in wettability through several analyses. The interlayer adhesion of both untreated and treated PC samples was verified by mechanical tests, and an improvement of about 30% in strength was achieved.

The last part was dedicated on the study of 3D printed Gyroid structures made of Carbon PEEK for both the optimization of the compressive strength-to-weight ratio and the enhancement of mechanical isotropy. The specimens were printed by varying the infill density, and the results were compared to the Gibson-Ashby model, finding a compressive behavior similar to bending-dominated lattice structures. The strength-to-weight ratio was optimized for a density of 70% allowing a saving of 30% of material and time and it was found that isotropy in compression is possible for a density of 25%. It was studied also the response of gyroid lattice structures in the impact absorption when used as core pattern in sandwich-like panels. The absorbed impact energy increased as the infill density increased while the gyroid was not damaged but was detached from the impacted skin. Non-destructive inspection (NDI) highlighted that the extent of the detachment increased with the impact energy. However, further investigation for the optimization and characterization of sandwich panels is necessary.

The results presented in this thesis work pave the way towards a turning point in the engineering and manufacturing of molds, tools and end-use products for aeronautics.

To my beloved family

I can do all things through Him who strengthens me.

(Philippians 4:13)

Acknowledgement

The PhD experience has been filled with a wide range of emotions, sometimes conflicting, but it has ultimately led to professional growth and personal enrichment, both culturally and individually. Now that this path has come to the end, all I can do is thank everyone who stood by me and supported me, especially during the difficult moments that, as with everything, are inevitable. I would like to express my gratitude to all those who believed in me and trusted me from the beginning: my supervisor, Prof. Gianluca Percoco, and everyone who welcomed me into the world of Leonardo S.p.A., my company supervisor, Eng. Stefano Corvaglia, Eng. Nicola Gallo, and all my colleagues from R&ED. I would also like to thank my colleagues, the researchers of Leonardo Labs in Grottaglie, who allowed me to learn so much, to collaborate in creating a pleasant and fun working environment, and to feel part of a complex system like that of research within the company. Among all of them, a special thanks goes to Sara: you were a point of reference not only for work aspects, but above all for your humanity, understanding and patience.

I would like to thank the research group of Prof. Gianluca Percoco, the guys with whom I have built friendship, respect, and trust, with whom I had the opportunity to collaborate, and who supported me during this PhD.
I would like to thank all the operators and technicians who helped me during the tests to collect the data presented in this thesis.

Lastly, I thank my beloved Gianluca and my family, who have always supported my choices and sustained me in difficulties, I owe everything to them and I dedicate this achievement, especially to my mother, who has been my guiding star, a source of inspiration, an example of resilience, courage, strength, and hope. I am sure that, even though she cannot be physically close to me, she is celebrating with me for having completed this journey and for having achieved such a significant goal.

Thank you all.

Ringraziamenti

Il dottorato di ricerca è stato un percorso ricco di emozioni, talvolta contrastanti, che ha portato ad una crescita professionale e ad un arricchimento sia dal punto di vista culturale che personale. Ora che questo percorso è giunto al termine, non posso fare altro che ringraziare tutti coloro che mi sono stati vicini e mi hanno sostenuto soprattutto nei momenti di difficoltà che, come in tutte le cose, non mancano mai. Vorrei esprimere la mia gratitudine verso tutti coloro che hanno creduto in me e mi hanno dato fiducia sin dall'inizio, il mio tutor Prof Gianluca Percoco, e a tutti coloro che mi hanno accolta nella realtà di Leonardo S.p.A., il mio tutor aziendale Ing. Stefano Corvaglia, Ing. Nicola Gallo e tutti i colleghi di R&ED. Vorrei ringraziare tutti i colleghi dei Leonardo Labs a Grottaglie che mi hanno permesso di imparare tanto, di collaborare creando un ambiente lavorativo piacevole e divertente, e di sentirmi parte di un sistema complesso come quello della ricerca all'interno dell' azienda. Tra tutti loro un ringraziamento speciale lo rivolgo a Sara: sei stata un punto di riferimento non solo per l'aspetto lavorativo, ma soprattutto per la tua umanità, comprensione e pazienza.

Ringrazio il gruppo di ricerca del Prof. Gianluca Percoco, i ragazzi con i quali ho instaurato rapporti di amicizia, stima e fiducia, con i quali ho avuto l'opportunità di collaborare e che mi sono stati di supporto durante questo percorso.
Ringrazio tutti gli operatori e i tecnici che mi hanno aiutato durante i test per raccogliere i dati presentati in questa tesi.

Infine, ringrazio il mio amato Gianluca e la mia famiglia che hanno sempre sostenuto le mie scelte e supportato nelle difficoltà, a loro devo tutto e dedico questo traguardo, in particolare alla mia mamma che è stata per me la stella polare, fonte di ispirazione, esempio di resilienza, coraggio, forza e speranza. Sono certa che anche se non potrà essere vicina a me fisicamente, lei starà gioendo con me per aver portato a termine questo percorso e per essere riuscita a raggiungere un grande obiettivo.

Grazie a tutti voi.

Index

1 Introduction

In the field of aviation, finding the best compromise between weight reduction and high mechanical properties is one of the most challenging goals. Therefore, aeronautical and aerospace engineers are continuously looking for materials that have good toughness, stiffness, good resistance to abrasion, impact and corrosion phenomena and that are lighter than metals. In this perspective, composite materials are studied in depth because of their lightness and very high performances. [1]
Composite materials used in the aeronautical field typically consist of a thermosetting matrix, such as epoxy resin, reinforced with glass, carbon or aramid fibers. [2] [3] [4] However, the need to make production processes more sustainable and faster and to recover materials at the end of the aircraft life is driving research to replace thermosets with thermoplastics. [2] The latter bring many benefits, in fact, they have good damage tolerance, they are weldable, recyclable and processable by out of autoclave (OOA) technologies.

Among those thermoplastics, Poly Aryl Ether Ketone (PAEK) polymer family would be the best candidate for thermosets replacement. [5] Indeed, they have high mechanical performances, high chemical and thermal resistance. The most well-known thermoplastic belonging to the PAEK family is Polyether-ether ketone (PEEK) which is already used as matrix for composite structural parts. However, this material is still much expensive than epoxy resins and its processing is made difficult by the high melting temperature (343°C) leading to high processing times and costs. [6]

To reduce costs related to material consumption and production logistics, it is possible to process PEEK and Carbon fiber reinforced PEEK (C-PEEK) using more sustainable methods such as Additive Manufacturing (AM). [6] Among AM technologies, the Fused Filament Fabrication (FFF) is a material extrusion process that allows the building of a three-dimensional part by means of layer-by-layer deposition of molten thermoplastic material. However, also for the FFF of PEEK part, an accurate process parameter optimization is needed.

1.1 Aim of the research

The aim of this work is to optimize the FFF process parameters for the manufacturing of PEEK and C-PEEK parts having maximum mechanical performances, minimum weight and absence of defects. To achieve this goal, first a design of experiment was conducted with the aim to study the FFF process parameters that most influence the structural features and mechanical performances of PEEK parts. For this part the most performing FFF machine available in the company was used.
After this first characterization, it was found that the optimized printing conditions however do not allow obtaining 100% full parts without defects, due to technological limits. The latter are mainly related to weak interlayer adhesion and the shrinkage of the extruded polymer during the cooling phase.

To overcome these limits, a study for improving the interlayer adhesion by plasma-induced chemical functionalization, crystallization and ablation was carried out. In particular, the research work was dedicated to the study of the effects of atmospheric plasma treatments on surface energy enhancement of 3D printed PC and PEEK which exhibit more or less the same manufacturing issues.

This preliminary study on the improvement of 3D printing of PEEK has served to better understand the behavior of this material, the process parameters and measures to be adopted for the optimal manufacturing of this challenging technopolymer. Thus, it was useful for continuing the activities with the printing of more complex and interesting structures, from the point of view of mechanical properties, based on Carbon-PEEK (C-PEEK).

Specifically, the last part of the work was entirely dedicated to the possibility of obtaining structural lightening without substantial loss of mechanical performances, using gyroid-lattice structures. For this purpose, compression and impact behavior of gyroid infill pattern was studied at different infill percentages. For this part of the study, it was decided to use C-PEEK as feeding material because, thanks to the presence of chopped carbon fibers, it exhibits less shrinkage and warping issues making it easier to print than pure PEEK. In fact, in this part of the work, it was possible to use a less performing printer which works with a heated building bed and an unheated chamber.

2 State of the art

This chapter offers a brief review of the materials used in aeronautical applications, the challenges relating to structural lightening of aircrafts for modern aeronautical and environmental needs, and the future perspectives on manufacturing processes and materials.

2.1 Lightweight materials for aeronautical applications

The aeronautical industry is focused on improving aircraft performance, fuel efficiency, and sustainability while reducing costs. A key objective is to reduce aircraft weight, which directly impacts fuel consumption and CO_2 emissions. [7] Traditionally, aluminum and steel have been used in aircraft construction due to their strength and low cost, but their weight, susceptibility to fatigue, and corrosion make them less ideal for modern needs. [8], [9], [10] Fatigue leads to structural failures over time, increasing maintenance costs, while corrosion in harsh environments requires protective treatments. [11] Additionally, metals are isotropic, limiting design flexibility, and their manufacturing processes are energy-intensive and costly.

As the aviation industry evolves, there is growing demand for lightweight, high-performance materials. Composites are emerging as a solution, offering weight savings that enhance fuel efficiency and operational capacity, especially in new technologies for urban air mobility (UAM) like electric vertical take-off and landing (eVTOL) aircraft. [12] While aluminum and steel will still be used in some areas of the aircrafts, the limitations of traditional metals highlight the need for innovation in materials science to meet the future demands of aviation. [13]

The need for "metal replacement" in aerospace and aeronautical engineering aims to substitute metals with high-performance polymer-based composites. These materials must offer strong mechanical and thermal resistance while minimizing density. As shown in the Ashby diagrams, mechanical strength generally increases with material density (Figure 2.1 a). Another aspect to be considered is the range of service temperatures that, for low density materials, is evidently restricted if compared to metals (Figure 2.1 b). Advanced composites, widely used in aeronautics, have high strength-to-weight ratio, excellent fatigue and corrosion resistance, high temperature resistance, close to metallic alloys, properties that depend on the specific composition of the material. [14]

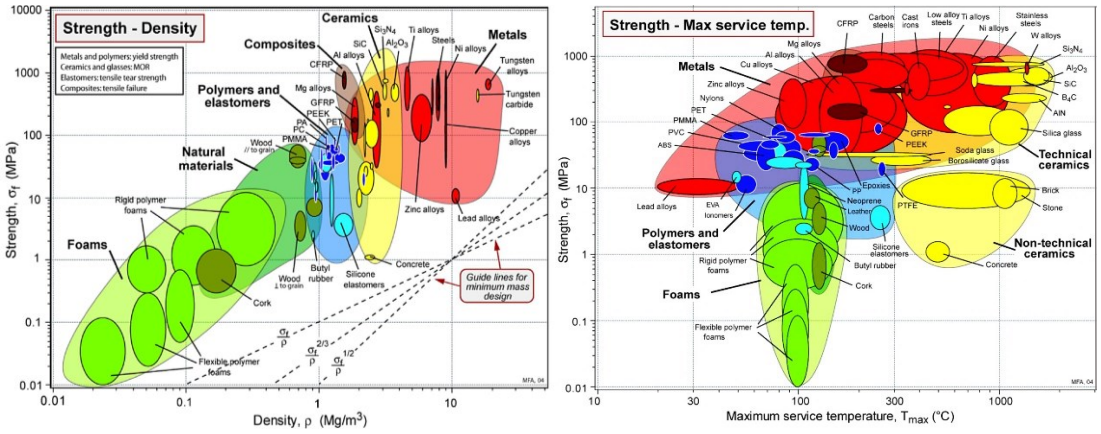

Figure 2.1: Ashby diagrams a) strenght vs. density and b) strenght vs. maximum service temperature. [14]

Typically, the composite materials are made of two (or more) chemically distinct, insoluble and easily distinguishable phases: a polymeric matrix and a disperse reinforcing material (like carbon, glass, or aramid fibers or particles). [2], [3], [4]The final properties depend on the properties of the constituent phases, their proportions, and the geometry of the fibers (shape, size, distribution and orientation), which can be tailored to suit specific loads. This results in highly directional mechanical behavior, allowing the material to be optimized for specific solicited direction. Typically, advanced composites are made of continuous high modulus fibers held together by an essentially homogeneous matrix. In Figure 2.2 a representative image of a lamina with unidirectional fibers is shown.

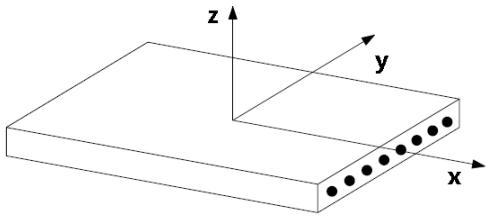

Figure 2.2: Lamina with unidirectional fibers.

The matrix not only shapes the material but also transfers loads, protects the fibers, maintains fiber orientation, and resists to cracks propagation and impact damage. Moreover, the matrix composition affects properties like resistance to shear, compression, heat, humidity, and UV rays, while the mechanical strength is mainly influenced by the quantity of fibers oriented in the direction subjected to stress. The main classification of composites depends on the type of polymer matrix: thermosetting or thermoplastic.

2.1.1 Thermosetting advanced composites

The first polymeric composites widely used for aircraft fuselages and wings were thermosetting (TS) matrix composites reinforced with discontinuous, unidirectional or intertwined synthetic fibers. [15] Thermosetting matrices in advanced composite materials used for aeronautics are polymer resins that undergo an irreversible chemical transformation when cured, providing structural integrity and thermal stability to composites. These matrices typically include epoxy, phenolic, bismaleimide (BMI), and polyimide resins. The epoxy resins are the most common and widely used due to their excellent mechanical properties, strong adhesion, and resistance to environmental degradation. However, for interior components, such as seats, overhead bins, and floor panels, and areas requiring fire protection, the phenolic resins are more indicated thanks to their flame resistance and low smoke emissions. Bismaleimide (BMI) offers higher temperature resistance than epoxies, often used in parts exposed to extreme temperatures, like engine components, instead polyimides provide even greater temperature resistance, suitable for applications above 250°C, such as in aerospace heat shields and high-performance aircrafts. [16] The matrices, combined with reinforcing fibers, allow to create tailored lightweight, strong, and heat-resistant composite materials essential for modern aeronautics.

These TS composites are widely used in constructing primary aircraft structures like fuselages, wings, stabilizers, and control surfaces. [17] Advanced composites are increasingly used in modern engine designs, including composite fan blades and casings in turbofan engines. These materials help create more efficient engines with improved resistance to fatigue and damage from foreign objects. [18]

The main types of TS advanced composites are listed below:

- *Carbon Fiber Reinforced Polymers (CFRP):* CFRP composites are commonly used for advanced applications in the aviation and aerospace industries. These materials consist of carbon fibers embedded in a polymer matrix, usually an epoxy resin. CFRPs are valued for their high strength-to-weight ratio, stiffness, and environmental resistance. When compared to metals, they reduce aircraft weight by 20-40%, which significantly improves fuel efficiency and operational performance. [2]

- *Glass Fiber Reinforced Polymers (GFRP):* Glass fibers, although less stiff and strong than carbon fibers, offer good toughness, impact resistance, and are cost-effective. GFRPs are often used for less demanding components or where greater flexibility is required, such as radomes (protective covers for radar antennas) and other non-structural parts. [3]
- *Aramid Fiber Reinforced Polymers (AFRP):* Aramid fibers, known by trade names like Kevlar, are lightweight and provide excellent impact resistance and energy absorption. AFRP is suitable for applications requiring ballistic protection and high-impact areas of aircraft, such as leading edges of wings. [4]
- *Hybrid Composites:* Hybrid composites combine different fibers, such as carbon and glass, within the same matrix. This allows for a balanced combination of cost, strength, and other properties. Hybrid materials are optimized to provide mechanical performance specific to certain areas of the aircraft, allowing for localized tuning of stiffness, strength, and weight. [19]

Once cured, thermosetting matrices offer significant advantages:

- high thermal stability being able to withstand high temperatures without losing structural integrity up to their degradation temperature (generally between 200-400°C);
- chemical resistance to solvents, fuels, and corrosive chemicals, offering long-lasting performance in harsh environments;
- dimensional stability, being able to maintain their shape and do not soften or deform under heat or stress, ensuring a high level of safety and reliability over time.

Furthermore, the mechanical properties of the final component can be tailored by a proper layup of plies (i.e. foils of pre-impregnated fibers in uncured resin) oriented along the directions of loads to which the part will be subjected. Prepreg layup is a very delicate procedure that can introduce defects and voids within the composite part. This procedure can be done either manually for small parts or automated via Automated Tape Placement (ATP) for large parts such as fuselages, a technique that guarantees less material waste. While ATP allows for precise placement and compaction of the composite material, the thermosetting resin used needs to undergo a curing cycle to achieve its final strength and structural integrity. The autoclave provides the heat and pressure required to initiate and

complete the polymerization process, transforming the resin from a viscous state into a solid, cross-linked structure. Moreover, autoclave helps remove any trapped air or voids between the layers of composite material, ensuring uniform consolidation and bonding between layers. The autoclave cure process requires long times, usually more than 20 hours, and high energy supply. [20]

Therefore, despite their advantages, these composites present challenges such as manufacturing complexity and the need for specialized inspection methods. The required manufacturing processes, autoclaving and vacuum bagging, increase production time, energy consumption and costs. Furthermore, non-destructive testing (NDT) methods, such as ultrasonic, thermographic techniques and computed tomography are needed to detect internal defects, like delaminations or voids, which could compromise the material's performance and safety. [20] Another issue relating to thermosets is the irreversibility of the polymerization (curing), in fact, thermosetting resins cannot be reshaped or reprocessed making repairs and modifications challenging.

Future research is focused on improving automated manufacturing processes with an in-situ consolidation and out-of-autoclave (OOA) curing techniques to reduce costs and enhance consistency. [21] [22] Additionally, there is growing interest in developing smart materials capable of monitoring and reporting their own structural health, or the use of thermoplastic composites as valid alternative to thermosetting materials. [23]

2.1.2 Thermoplastic advanced composites

In the 1980s and 1990s, following the development of high-performance thermoplastic polymers (TP), a strong interest arose, especially from the aerospace industry, for TP matrices also in advanced composites. [24] In fact, as aircraft become more complex and the demand for greener aviation increases, the need for advanced thermoplastic composites has grown significantly. From this point of view, thermoplastic composite materials offer the important advantage of being recyclable, reshaped and easily repairable, when heat is applied, which aligns with the growing trend toward sustainable manufacturing and maintenance.

Considering the mechanical properties, the damage resistance and strength of thermosets are lower when compared to thermoplastics, due to their inherently brittleness. [24] These

issues of TS limit their impact resistance and flexibility, increasing the need for ever-wider use of thermoplastic materials in applications requiring these properties.

The best performing thermoplastic materials which can be used for aeronautical purposes are the technopolymers. The term technopolymer generally refers to a material that can be used as a substitute of other heavier material such as metals. They include both amorphous and semi-crystalline polymers. These plastics, characterized by properties such as high strength, stiffness, impact resistance, fire resistance, high thermal, chemical and corrosion resistance, due to their higher cost compared with common materials, are principally used for advanced purposed in automotive, transportation, electronics, communications aeronautical and aerospace applications. Some of the most important thermoplastic matrices used in aeronautical applications include PEEK (Polyether Ether Ketone), PPS (Polyphenylene Sulfide), PEI (Polyetherimide), PAI (Polyamide-imide), PEKK (Polyetherketoneketone), and Nylon (Polyamide). [25]

PEEK stands out for its high-temperature resistance, maintaining structural integrity up to 250°C, along with excellent mechanical strength and chemical resistance. It is commonly used in aerospace components like engine parts and fasteners due to its balance of properties and recyclability. [26] [27] Similarly, PPS is known for its thermal stability and chemical resistance, tolerating continuous use at around 200°C. Its low flammability and dimensional stability make it ideal for aircraft electrical components and fuel systems. [28] PEI, with its high strength and stiffness, is another commonly used thermoplastic in aerospace, particularly for interior components like seat frames and cabin linings. Its excellent flame-retardant properties meet stringent safety standards in aircraft interiors. [29] PAI offers exceptional mechanical properties, including high tensile strength and wear resistance, even at temperatures up to 260°C, making it a very good material for mechanical components like bearings and gears. [30] Meanwhile, PEKK performs well in high-heat environments, with continuous-use temperatures of up to 260°C, and is often used in structural components where high mechanical performance is crucial. [31] Lastly, Nylon (Polyamide), though with more moderate heat resistance, is valued for its toughness and impact resistance, often used in less demanding aerospace components like brackets and fasteners. [32]

All these high-performing materials, if combined with functional fillers, could significantly change the properties of the pristine material by improving them or adding

new ones. In the last decades, a lot of studies have been performed in order to evaluate how different functional fillers can affect the overall features of the conventional thermoplastic polymers. [33] In particular, it was discovered that the material, type, size and amount of filler inside the matrix can significantly change the properties of the final composite. Functional fillers are classified, based on the material that constitutes them, into 7 groups: carbon-based (carbon fibers, nanotubes, graphene, carbon black...), ceramic powders (Al_2O_3, ZnO, TiO_2, ZrB_2…), metallic powders (Fe, Cu, Al…), glass-based (glass fibers, microspheres, boron glass…), minerals (Zeolites, Montmorillonite, talc…), wood-based and hybrid composites (the combination of more than one filler in the same matrix). These fillers, if dosed appropriately within the matrix, can improve the material properties such as: the mechanical performances (tensile strength, Young's Modulus, flexural strength), the heat capacity, thermal stability and wear resistance. This paves the way for the formulation of a vast range of ever new materials with customized characteristics in relation to the final application. [33]

As regards the production and processing of these materials, it must be highlighted that, when thermoplastic polymers are melted or softened by heating, the molecules interact due to weak secondary bonds. Since the latter are reversible, unlike thermosetting polymers, they allow forming processes that may require repeated heating (e.g. thermoforming and solder joints). Furthermore, as there are no cross-linking reactions as in thermosets, TP composites can be consolidated and formed very quickly. On the other hand, advanced TP polymers require significantly higher consolidation and forming temperatures than common epoxy matrix laminates. [24] This makes process operations more complex and requires the use of equipment and materials suitable for these conditions.

However, thermoplastic composites can be manufactured not only by OOA processes but also by the growing Additive Manufacturing processes, having the main advantage of allowing the production of parts with very complex geometries using only the needed material. [34]

2.2 Additive Manufacturing: opportunities and limits

Additive Manufacturing (AM), also known as 3D printing, is a group of technologies that allow to fabricate objects layer-by-layer directly from digital models, rather than through the traditional subtractive methods that involve cutting, drilling, or molding. AM represents a paradigm shift in manufacturing, with the potential to disrupt the way engineers design and manufacturers produce, facilitating the production of parts having complex geometries, reducing material wastage, and allowing the rapid customization of parts for specific applications. Its diverse methodologies can be classified into distinct technological families, each characterized by specific physical processes, material forms, and application areas. The classification of AM technologies is guided by the mechanisms of material deposition and solidification. The ISO/ASTM 52900 categorizes AM processes into seven primary families, based on these principles. A summary diagram of all additive manufacturing technologies is shown in the following figure.

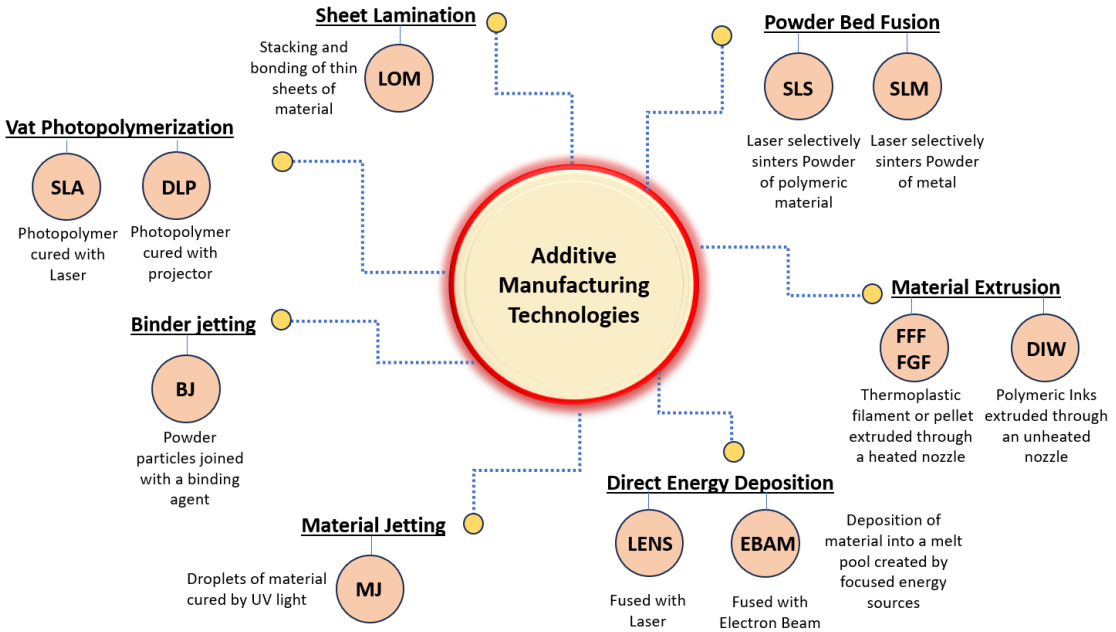

Figure 2.3: Additive manufacturing technologies.

Among all these technologies the Material Extrusion (MatEx) technologies have started gaining a lot of interest in different fields for their simplicity and safety. In MatEx the feeding material is extruded through a nozzle which can be heated or not depending on the type of material. The nozzle moves in the working volume following the coordinates generated by the digital 3D model, depositing the material layer by layer to build the final

workpiece. Once deposited, the material solidifies either by cooling or through chemical reactions. [35]

At the state of the art, there are three main MatEx processes: Fused Filament Fabrication (FFF), Fused Granular Fabrication (FGF) and Direct Ink Writing (DIW), classified according to the chemical type of feeding material (i.e., thermoplastics or photocurable polymers), the original form of the material (i.e., filament, pellet or paste-like material) and the pushing mechanism (i.e. gear-, screw- or piston-assisted extrusion). FGF represents a significant evolution in 3D printing, particularly for processing thermoplastics and composites. FGF employs granules or pellets, offering cost and material versatility advantages. This process is gaining attention due to its potential for high throughput and the ability to utilize a broader range of polymers, including high-performance materials like PEEK, as well as composites reinforced with fibers or nanoparticles. [36] [37] Recent advancements in FGF have focused on optimizing material flow, extrusion precision, and process stability. Improvements in screw extruder design and nozzle control have enabled better control over melt properties, ensuring consistent deposition and minimizing defects. [36] [38] [39] In terms of applications, FGF has found a foothold in industries like aerospace, automotive, and construction, where large-scale parts and custom geometries are needed. [40] Researchers are also exploring its potential for producing multi-material parts, leveraging the ability to blend granules directly in the extruder for graded material properties. [41] However, challenges remain, particularly in achieving fine resolution and minimizing porosity in parts compared to filament-based systems. The current state of FGF also highlights efforts in sustainability, with a focus on recycling polymer waste into granules suitable for printing. [42] Additionally, advancements in polymer science are expanding the range of compatible materials, including bio-based and recyclable options. [42], [43] [44] Overall, FGF is emerging as a complementary technology to FFF, with its unique advantages driving its adoption in both industrial and research contexts. The most widely spread and with the fastest development is certainly FFF technology thanks to the fact that it is very user-friendly and versatile and thanks to the growing range of commercially available filaments. For these reasons, FFF is widely adopted in industries such as aerospace, automotive, and consumer goods, predominantly used for prototyping, tool production, and low-cost, low-volume production of parts. [45] [46]

In Fused Filament Fabrication, a thermoplastic material, initially given in the form of filament wound in coils, is pushed by a pair of counter rotating gears through a nozzle heated at a temperature above the polymer melting point (if semicrystalline) or softening temperature (if amorphous). The fused material is extruded from the nozzle and deposited layer-by-layer on the building plate. Generally, the nozzle head moves in the x and y directions and the build plate moves up and down along the z axis. In addition to the nozzle, many 3D printers can have a heated bed to ensure good adhesion of the first extruded layers and a heated chamber which is needed for polymers that require good thermal stability and slow and controlled cooling during the printing process. The Figure 2.4 shows a schematic representation of a typical FFF machine.

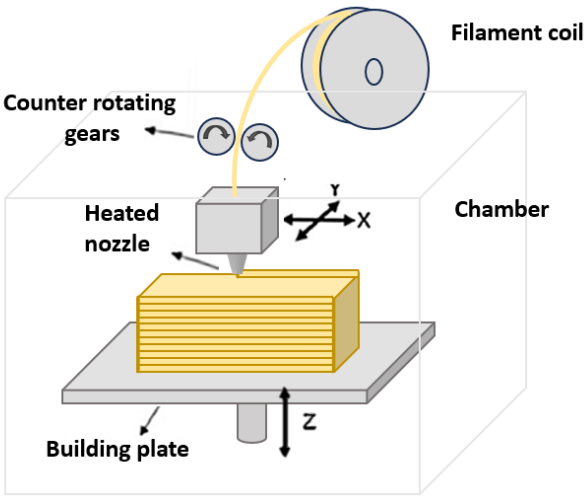

Figure 2.4: Scheme of Fused Filament Fabrication machine.

The additive FFF process brings a lot of opportunities and benefits to manufacturing that make it a key technology for various industries. Firstly, it enables the creation of intricate structures and complex geometries that would be difficult or impossible to achieve with traditional manufacturing techniques. AM technologies use only the material needed to fabricate the object, minimizing material waste compared to subtractive processes. 3D printing also promotes topological optimization, i.e. the design of components with cavities or lattice structures, combining lightness and mechanical strength. This technology allows for the custom production of individual pieces or small series, making mass customization economically feasible. This accelerates the development of new products by allowing the rapid creation of functional prototypes, facilitating the rapid

design iteration, allowing for quick and low-cost modifications directly from digital models (CAD) in response to market feedback or customer requirements.

Another significant advantage is the reduction in production times, thanks to the ability to build components in a single manufacturing step without the need for assembly of multiple parts. Furthermore, this technology lowers production costs for small series and prototypes by eliminating the need for expensive tools like molds and dies. On-demand production and the ability to manufacture components at the point of use simplify the supply chain. FFF also offers the use of a wide range of advanced materials, including polymers, metals (Metal-FFF also known as *Shaping, Debinding and Sintering-SDS*), [47] and composites, which can be specifically formulated for particular applications. All these advantages make FFF an essential technology for modern industries.

However, the technology available today needs to be further refined, still presenting some limitations to overcome and challenges to face. [48] The first challenge is related to the quality assurance: in order to meet industrial standards, defects such as porosity or residual stresses that affect part performance must be minimized and eliminated. Another problem is the fact that AM-produced parts exhibit anisotropic properties, meaning their strength may vary based on orientation. [49] This necessitates careful design of the part, particularly for critical applications. Moreover, the layer-by-layer build process inherently limits the build speed particularly for large parts, making FFF less suitable for high-volume and large-scale manufacturing. Additionally, if better surface finish and dimensional accuracy is needed, FFF-printed parts must be post-processed. [50] [51] This increases time and cost to the manufacturing process. Finally, the FFF technology imposes constraints on materials because not all materials exhibit the required mechanical properties or processing compatibility. Thus, the range of materials available is still limited compared to traditional manufacturing. Much research is focused on the formulation of new thermoplastic-based materials suitable for the FFF process. Another disruptive challenge is linked to the possibility of printing continuous rather than chopped fiber composites, a technology that is still too little widespread. [52]
Since the technology continues to mature, with innovations in materials, printers, process optimization, and post-processing, FFF will increasingly take place in industrial manufacturing.

2.2.1 Strategies to optimize the FFF process

In the Fused Filament Fabrication (FFF) process, welds between stacked layers are formed through the interaction of molecules in the extruded filament, facilitated by high temperatures (as shown in Figure 2.5). Despite using maximum infill, voids can still appear within the layers. These voids, caused by rapid cooling of the molten filaments or insufficient overlap between the extruded and solidified material, weaken the printed parts. Consequently, it is essential to optimize the process to minimize defects and manage internal porosity.

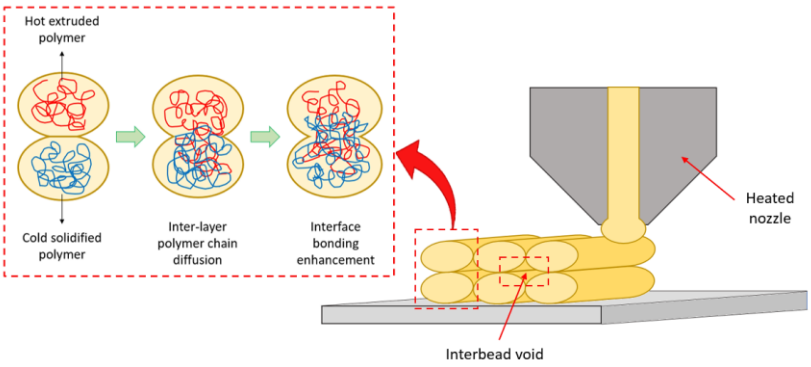

Figure 2.5: Interbead voids in FFF-printed parts.

Another major issue affecting the mechanical properties of FFF printed parts is the weak inter-layer adhesion: ensuring strong adhesion at the interfaces is fundamental to obtain performance comparable with counterparts obtained by other manufacturing technologies such as injection molding.

Several approaches could be employed to improve interlayer adhesion and reduce voids, grouped into 3 main categories:

- pre-manufacturing strategies (including process parameters set in the slicing software or feed material treatments before printing)
- in-situ treatments
- post-processing techniques.

Regarding the pre-production approach, several studies have been conducted to improve adhesion and reduce porosity by optimizing process parameters. Typically, the

performance of FFF printed parts is influenced by various process parameters, including material deposition speed, part orientation, layer thickness, nozzle temperature, and chamber temperature [53]. Optimizing these parameters is particularly crucial for high-performance polymers such as polyether ether ketone (PEEK). The 3D printing of PEEK and its composites is challenging due to their semi-crystalline nature, high melting point, and viscosity [54]. As a result, FFF processing of these materials faces limitations related to significant thermal gradients, residual stress accumulation, and inter-layer adhesion. [55]

Extensive research has been conducted to understand how to fine-tune process parameters for producing high-quality FFF-printed PEEK parts with minimal defects. Printing PEEK poses challenges due to its high melting point and sensitivity to thermal conditions during printing. One crucial factor for achieving successful PEEK parts lies in the proper use of both building bed and chamber heating. These are essential because the 3D printed PEEK layers tend to warp and delaminate if the print environment isn't properly controlled. [56] Heated base plates help in anchoring the part to the build surface, while chamber heating ensures that the part remains above the glass transition temperature throughout the printing process. These combined conditions lead to PEEK components with high crystallinity, enhanced interlayer adhesion, and excellent mechanical properties, such as strength and durability. [57] [58] [59]

Jin et al. highlighted that the degree of crystallinity in PEEK is not only influenced by the printing environment but also by the cooling rate and thermal gradient during the process [60]. Slower cooling rates allow the polymer chains to align more effectively, resulting in greater crystallinity, which is fundamental for achieving high performance in end-use parts. Conversely, rapid cooling can result in lower crystallinity, reducing part strength and potentially introducing defects.

Yang et al. delved deeper into the thermal aspects of FFF-printed PEEK, investigating how different thermal processing conditions affect both crystallinity and mechanical properties. Their research demonstrated that maintaining an ambient temperature higher than PEEK glass transition temperature is critical for ensuring good mechanical performance. Additionally, they discovered that post-processing treatments, such as annealing, could further enhance crystallinity, while also reducing residual stresses and defects that might otherwise compromise part integrity [61].

Wang et al. applied finite element simulations to gain further insight into the PEEK printing process. Their work revealed that adjusting key parameters, such as reducing the layer thickness and slowing down the printing speed, can significantly improve the final part quality. These adjustments lead to higher part density, a smoother surface finish, fewer internal defects, and better bonding between layers and infill filaments. This optimization is crucial for enhancing both the strength and appearance of PEEK parts, making them suitable for demanding industrial applications. Furthermore, the authors emphasize that achieving strong adhesion between printed polymer filaments (inter-layer adhesion) requires the layer thickness to be at least 1.5 times smaller than the nozzle diameter. This adjustment ensures optimal bonding between layers, reducing the likelihood of delamination and improving overall part integrity [62]. Ding et al. reported that printing in a horizontal orientation provides the best mechanical performance for PEEK components, as it allows for more uniform layer stacking. They also noted that increasing the nozzle temperature lowers the melt viscosity, thereby enhancing material flow and improving the part internal density [63].

Rahman et al. explored various filament infill strategies, and their tensile tests revealed that aligning the print direction of the filaments along the loading direction (0° orientation, Figure 2.6 a) results in the best tensile performance for FFF-printed PEEK parts. This orientation aligns the polymer chains more effectively, strengthening the part in the direction of the applied load [64]. Arif et al. confirmed these findings, showing that parts printed with the largest surface area positioned horizontally on the build plate, combined with a 0° infill angle, had significantly higher tensile strength than those with a 90° infill angle, whether oriented horizontally or vertically [65].

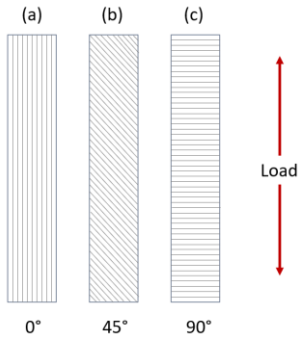

Figure 2.6: Schematic representation of filament infill orientations with respect to the load.

El Magri et al. performed a design of experiments analysis on the main FFF parameters for PEEK printing. By applying the response surface methodology to optimize the

process, they found that nozzle temperature was the most critical factor influencing both tensile properties and crystallinity of the printed parts. Their results indicated that higher nozzle temperatures improve both material strength and crystallinity, crucial for the performance of end-use PEEK parts [20]. Numerous studies have also reported that printing at a nozzle temperature exceeding 400 °C significantly enhances mechanical strength, due to improved adhesion between filaments both within and between layers. [58] [62] [66] [67]

From the study by Liaw et al it emerged that the parameter that most influences the adhesion of the interlayer in PEEK is the nozzle temperature, followed by layer height and waiting time. Furthermore, the same authors demonstrated that post-printing thermal annealing increases crystallinity and flexural modulus but has minimal effect on adhesion, concluding that the bond strength between layers is primarily determined during the printing process. [68]

Another process parameter that can be enabled via slicing software is “ironing”. The heated nozzle passes over the already deposited polymer to heat it while exerting pressure on it, with the aim of flattening and making the surfaces more uniform and smooth before depositing the new layer. The studies by Neuhaus et al and Stano et al confirm that ironing is advantageous in improving the surface quality of the deposited layers, but with the disadvantage of increasing printing times and the possibility of finding unwanted variations in the dimensions of the parts along the growth direction (Z axis). [69] [70]

Other pre-manufacturing approaches can be, for example, the synthesis or formulation of PEEK-based mixtures or the addition of plasticizers. Shang et al modified the molecular structure of PEEK by introducing fluorene-based functional groups in the polymer synthesis phase which break the molecular regularity in order to obtain a slow-crystallizing PEEK. [71] The study by Xu et al shows an increase in adhesion by formulating blends based on PEEK and compatible amorphous PAEK to obtain a PEEK with a greater amorphous phase which is able to diffuse better at the interfaces. [72] Since compared to other polymers used in FFF such as ABS and PLA, PEEK is processed with nozzle temperatures higher than 400°C, common plasticizers that degrade at that temperature cannot be used. However, a fairly recent study by Li et al describes an innovative method that exploits the pyrolysis reactions of polyhedral oligomeric silsequioxane (POSS) to produce benzene derivatives chemically similar to PEEK which act as plasticizers, hindering its crystallization. [73] Post-processing treatments involve

heating the part in such a way as to activate the diffusion of the polymers at the interfaces and induce thermal healing of the defects (porosity). A work by Yang et al compares different thermal post-processing methods carried out on PEEK, showing that the best treatment to increase mechanical resistance is thermal annealing. [61] However, as with ironing, also in this case, the process not only significantly increases the production time of the part, but can significantly deform it. [74] Furthermore, the annealing of semi-crystalline polymers above cold crystallization does not contribute much to the improvement of interlayer adhesion as the increase in the number of crystallites hinders the diffusion of polymer chains at the interfaces. [75]

The most efficient approach is the in situ treatment which allows to improve the adhesion layer by layer directly during the deposition of the material. In situ treatments generally involve a modification of the printing machine in order to add tools capable of transferring energy to the surface through heating, pressure or chemical reactions. Andreu et al integrated a hot roll in their FFF printed to compress and heat each layer homogeneously onto the previous one [76]; several research explored laser-based surface heating method to enhance the interlayer bonding [77] [78] and other approaches involve the integration of pre-heating systems with infrared lamps, that heat the layer on which it is being deposited the melted polymer. [79] [80]

Cold atmospheric plasma surface treatment is one of the most interesting approaches thanks to its versatility for the treatment of several materials providing chemical activation without the need for a vacuum environment. [81] Zarei et al [82] exploited an Argon plasma torch to enhance wettability of 3D printed scaffold made of PLA with CaCO3 micro-particles; Narahara et al used an Helium plasma plume to treat PLA, founding an improvement in surface energy of about 75%; [83] Nastuta et al examined the impacts of He and Ar atmospheric pressure plasma jet on the chemical composition and wettability properties of acrylonitrile butadiene styrene (ABS) surfaces, founding an improvement in wettability up to 60% for both working gases. [84] To date atmospheric plasma treatment has still been little studied for the improvement of interlayer adhesion in FFF printed technopolymers. An example found in literature is the study by McLouth et al to improve the wetting characteristics and bond strength of ULTEM 9085 using atmospheric plasma, obtaining an increase in strength of 35%. [85]

Building on the findings of these previous studies, the first part of the research presented in this thesis focused on maintaining constant parameters such as printing orientation, layer thickness, nozzle diameter, and infill density, while varying key factors like printing speed, nozzle temperature, and chamber temperature. This approach was aimed at assessing how these changes impact the crystallinity and tensile properties of FFF-printed PEEK parts. By optimizing these variables, this study seeks to contribute to the broader understanding of how to manufacture PEEK components with superior mechanical performance and minimal defects. Subsequently, wanting to apply the plasma treatment approach to improve interlayer adhesion, a study was conducted on both Polyether (etherketone) and Polycarbonate to understand the phenomena that act on the surface of the material to improve its wettability.

2.2.2 Atmospheric Plasma treatment

Atmospheric plasma functionalization is an advanced surface treatment technique used to enhance adhesion between materials, particularly in applications involving polymers, composites, and metals. This method involves generating a plasma - a highly reactive ionized gas - at atmospheric pressure, which interacts with the surface of the material to be treated. Unlike traditional plasma treatments, which require a vacuum environment, atmospheric plasma offers the convenience of being performed in open air, making it more practical and cost-effective for industrial use.

Atmospheric plasma increases the surface energy of materials, making them more receptive to adhesives, coatings, or other substrates. This is particularly beneficial for low-surface-energy materials like plastics, which exhibit very low wettability.

During the plasma treatment, the energetic particles (ions, electrons, and radicals) in the plasma collide with the surface of material, breaking molecular bonds and introducing new functional groups that enable the formation of new bonds. These polar groups are hydroxyl (-OH), carboxyl (-COOH), and carbonyl (-C=O), and thanks to the presence of oxygen and hydrogen atoms they will form H-bonds with the next layer. This modification improves the surface's chemical activity, roughness, and wettability, creating a better foundation for bonding with other materials. In addition to chemical changes, atmospheric plasma can also physically clean the surface by removing

contaminants such as oils, dust, and organic residues, further improving adhesion performance.

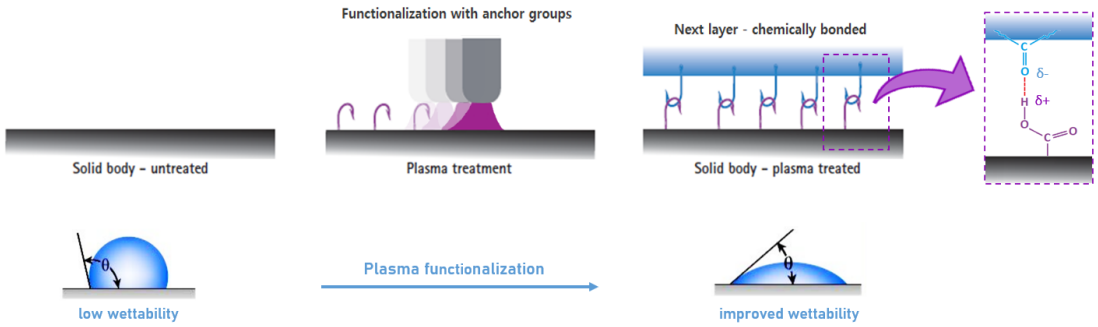

Figure 2.7: : Schematic representation of the cold-atmospheric plasma functionalization. [86]

The adhesion improvements achieved through plasma functionalization result in more durable bonds, which can withstand mechanical stresses, thermal cycling, and environmental factors better than untreated materials.

Furthermore, as a dry, solvent-free process, atmospheric plasma functionalization is an eco-friendly alternative to traditional surface treatments, reducing the use of hazardous chemicals and minimizing waste. Atmospheric plasma functionalization is a versatile and efficient surface treatment technique that significantly enhances the adhesion between materials, especially in challenging applications where strong adhesion is required. Its ability to modify the surface at a molecular level without the need for chemicals or extensive equipment makes it a highly attractive option for industries seeking improved performance and sustainability.

In FFF 3D printing, as seen in the previous paragraph, one common challenge is the relatively weak adhesion between printed layers, which can result in reduced mechanical strength, particularly along the Z-axis (the vertical direction). Atmospheric plasma treatments offer a promising solution to improve inter-layer adhesion in FFF printed parts, especially when working with high-performance polymers like PEEK or other engineering thermoplastics.

Atmospheric plasma treatment works by modifying the surface of the printed layers as they are deposited. The plasma interacts with the surface, enhancing its chemical and physical properties, which ultimately improves the bonding between subsequent layers. Here's how it happens:

- *Surface Activation:* Plasma treatment activates the surface of each printed layer by introducing polar functional groups and increasing surface energy. This activation makes the layer more chemically reactive and better able to bond with the next deposited layer.
- *Improved Wettability:* The increased surface energy from the plasma treatment enhances the wettability of the surface. As a new layer is extruded, it can spread more easily over the activated surface, leading to improved contact and bonding between the layers.
- *Surface Cleaning:* Plasma treatment also removes contaminants, such as dust, residual oils, or degraded polymer material, from the surface of the layers. These contaminants can hinder adhesion, so cleaning the surface in real-time ensures that each layer bonds more effectively.
- *Micro-structuring of the Surface:* Atmospheric plasma can introduce subtle roughness or micro-textures on the surface of the printed layer. This mechanical interlocking effect further improves adhesion between layers, increasing the overall strength of the printed part.

By improving the adhesion between layers, plasma treatment results in printed parts with better mechanical integrity, reducing the likelihood of delamination or weak points in the Z-axis. High-performance polymers like PEEK, PEI, or PPSU often face adhesion challenges due to their chemical resistance and low surface energy. With better inter-layer adhesion, the printed parts are more durable and resistant to mechanical stress, making them suitable for high-stress or load-bearing applications. Moreover, stronger inter-layer adhesion allows for more complex geometries and larger parts to be printed with consistent quality, even across long print durations.

Plasma treatment can be integrated into the FFF process, allowing each layer to be treated as it is printed, making the approach compatible with continuous, automated production without significant time delays. In fact, it is an almost instantaneous treatment that can be carried out at the same time as the deposition of the material during printing.

2.3 Trabecular structures

As already introduced in the previous paragraphs, the main objective of this thesis is to optimize the 3D printing process and the produced parts for lightening purposes, making the most of the potential of this production methodology and trying to overcome its limitations. Some interesting approaches for lightening purposes, in addition to metal replacement with thermoplastics and composite materials that exhibit a high strength-to-weight ratio, [87] could be the topological optimization and the use of lattice structures. Topological optimization is a procedure for optimizing the design of parts in such a way that superfluous material that is not subject to loads is removed, keeping it only where it is needed. Similarly, it is possible to vary the weight and mechanical properties of a part by using lattice structures (like foams) with different geometries and/or densities of cells. In this way, it is possible to lighten the part without changing its design and sometimes without significantly changing its performance.

Foam cells are classified into two types: open cells, where the cells are interconnected by struts, and closed cells, where the cells are enclosed by thin walls. The angles at which the struts and faces meet play a crucial role in determining the cell's mechanical behavior. According to the Gibson-Ashby model, the mechanical properties of foam are expressed as relative values compared to those of an equivalent solid of the same dimensions and material. The compressive strength and compressive modulus related to density are calculated as a power-law trend using Eq. 1 and Eq. 2, respectively.

$$\frac{\sigma}{\sigma_0} = C_1 \left(\frac{\rho}{\rho_0}\right)^m \qquad \text{Eq. 1}$$

$$\frac{E}{E_0} = C_2 \left(\frac{\rho}{\rho_0}\right)^n \qquad \text{Eq. 2}$$

Where:

σ, E and ρ are the strength, elastic modulus and infill density of the lattice structure respectively;

C1, *C2*, m and n are proportionality coefficients and exponents of the relationship and could be determined by the nonlinear regression fitting of the data and least squares method.

The model allows to interpret the mechanical behavior of lattice structures by dividing them into two categories: bending-dominated structures (BDS) and stretching-dominated structures (SDS), see Figure 2.8. In BDS the bending stresses are not balanced due to insufficient struts, so the structure fails in shear bands resulting from the collapse of unitary cells. In SDS the struts are enough to resist bending stresses, therefore they only collapse due to axial stresses. The ideal BDS have m equal to 1,5 and n equal to 2; instead ideal SDS have both m and n equal to 1.

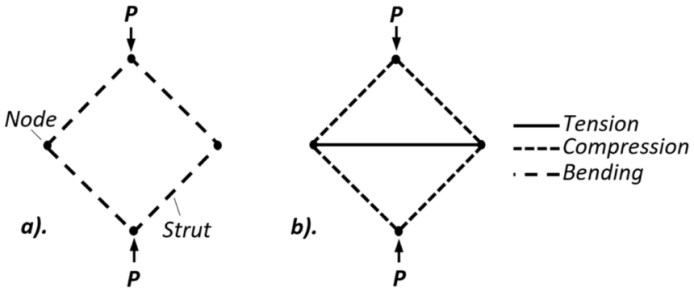

Figure 2.8: Scheme of loads distribution in BDS (a) and SDS (b). [88]

The most commonly varied characteristic of trabecular structures is the shape of the cells. Examples include body-centered cubic (bcc) cells, body-centered cubic with vertical struts along the Z-axis (bccz), face-centered cubic (fcc), and face and body-centered cubic with vertical struts along the Z-axis (fccz), which are geometries formed by the intersection of struts.

However, very interesting cellular structures are the Triply Periodic Minimal Surfaces (TPMS). The TPMS are a special class of minimal surfaces, which are surfaces with zero mean curvature at every point. The mean curvature at any point on a surface is the average of the curvatures in two orthogonal directions. For a minimal surface, *zero mean curvature* means that the surface is perfectly balanced and does not bend more in one direction than the other. Minimal surfaces are those that locally minimize surface area under certain boundary conditions. "Triply periodic" refers to their repeating structure in three independent spatial directions. [89] In fact, they are periodic in three dimensions, meaning that they can be tiled throughout space without gaps. They repeat in the x, y, and z directions at regular intervals, often forming lattice-like structures. TPMS tend to have intricate geometries with smooth shapes. These structures often contain labyrinthine voids and are embedded within a periodic framework. Their shapes are often challenging to describe using elementary functions and are typically defined through complex

mathematical representations or numerical approximations. They exhibit a high degree of symmetry: they belong to specific crystallographic groups and are often invariant under various symmetry operations such as reflections, rotations, and translations. [90] This symmetry and the high surface-to-volume ratio make them of interest in material science and engineering applications.

Examples of widely known TPMS are Gyroid, Schwarz Diamond, Schwarz Primitive, Lidinoid and Neovius, described below. [91]

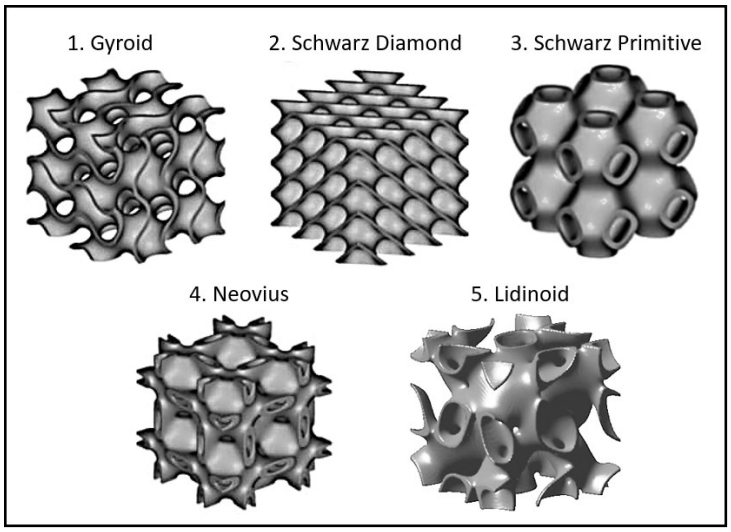

Figure 2.9: Representation of some TPMSs.

- *Gyroid*: This surface is non-self-intersecting and does not have mirror symmetry. It has a unique chiral structure and appears in materials like certain liquid crystals and biological systems (e.g., butterfly wings).
- *Schwarz Diamond*: A TPMS with a structure similar to the atomic arrangement in diamonds. It forms a labyrinthine network of interconnected surfaces.
- *Schwarz Primitive*: A highly symmetric structure where cubic cells repeat periodically. It is named after the mathematician Hermann Schwarz.
- *Neovius*: A surface with relatively simple geometry and high symmetry, related to the Schwarz P surface but with more voids or "pockets."
- *Lidinoid*: A complex minimal surface with triply periodic symmetry but with a more intricate network of surfaces and tunnels.

The use of lattices is due to the particular characteristics that these structures have compared to the dense material. In fact, TPMS-like structures can be used to create materials with tailored mechanical properties. For example, gyroids can lead to high

strength and low-density materials, mimicking the structure of bones or biological tissues, they are therefore perfect candidates not only for lightweighting applications but also to meet the requirements of multifunctional materials in terms of energy absorption, heat transfer and thermal insulation. [92] [93] [94]

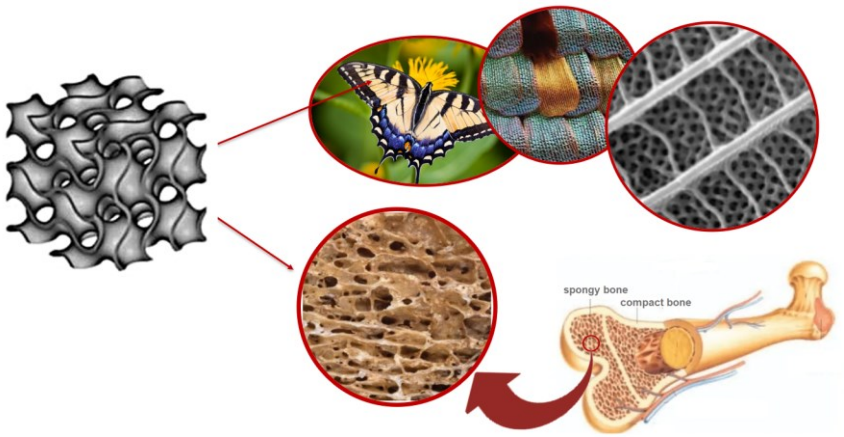

Figure 2.10: Gyroid a structure bio-inspired by the microstructures of butterfly wings and the open porosity in spongy bone.

Generally, the compressive strength of cellular structures makes them ideal for structural applications, especially when the load is aligned with the cell shape.
A common example is sandwich panels, which are widely used in aerospace because their low density provides mechanical strength while minimizing weight. These structures consist of two thin, stiff face sheets (skins) bonded to a lightweight core material, such as foam or honeycomb, as shown in Figure 2.11. The core and surfaces are typically bonded together with adhesive.

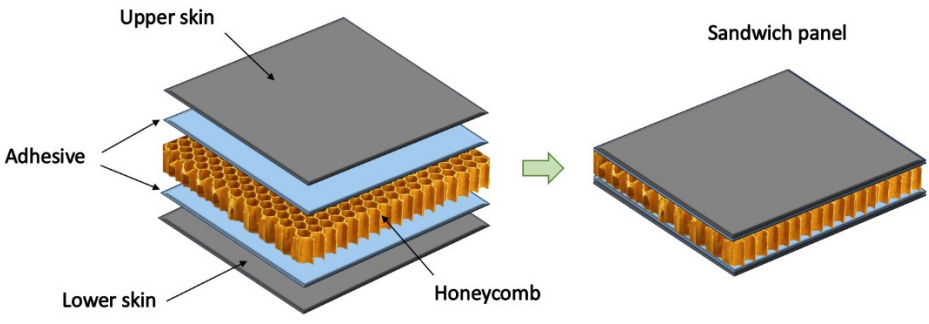

Figure 2.11: Sandwich panel structure.

The key benefits that arise from the use of sandwich structures in the aeronautical and aerospace industry are:

- The ability to provide exceptional strength while remaining lightweight.

- The core material provides thickness and rigidity, while the composite face sheets offer strength. This combination creates structures that are highly stiff, resisting bending and deformation under load. [95]

- Improved Impact Resistance: sandwich structures are designed to absorb and dissipate energy efficiently.

- Thermal and Acoustic Insulation: the core structures, especially foam or honeycomb, thanks to the presence of air inside the cavities, provide natural insulation against temperature fluctuations [96] and noise [97], which is crucial for maintaining a stable environment within aerospace vehicles.

Moreover, by tailoring materials and geometries of the sandwich structures allows engineers to design structures that meet specific performance criteria, such as optimized strength, weight, or stiffness in certain areas. sandwich structures were invented to address several key challenges and requirements that traditional materials could not fully meet. As a consequence, they have attracted a lot of interest in many industries (automotive, biomedical, aerospace...) and are widely used for a lot of applications in satellites, [98] aircraft interiors, [99], [100] wings [101] and so on. [102] [103] Recent research studies have highlighted that the trabecular core geometry has a significant impact on the overall mechanical performances of sandwich structures. [104] For example, it was studied that by engineering the cellular core in terms of shape, size, and density, mechanical behavior and energy absorption capability of the sandwich can be improved. [105]

In this context, additive manufacturing offers the possibility of creating sandwich structures having a cellular core with very complex geometries that could never be recreated using traditional subtractive technologies.

2.3.1 3D printing of TPMS porous structures

The development of the Fused Filament Fabrication is always growing not only thanks to the expansion of the range of extrudable materials (thermoplastics, composites, metals/alloys, and ceramics) [106] [107] and to the increasingly advanced 3D printing machines, but also to the progressive improvement of slicing software which make

possible to establish the process parameters that will give certain properties to the printed part. Two parameters that can affect the mechanical properties of the printed parts are: infill density and infill pattern [61] [108]. Aloyaydi et al. investigated the effect of infill patterns on the mechanical response of 3D printed poly-lactic acid (PLA), finding that different infill strategies significantly affect the tensile strength and elasticity. [109] Moradi et al. examined honeycomb infill patterns for FFF, optimizing production parameters and characterizing mechanical properties such as compressive strength and density. [110] Kiendl and Gao focused on how raster layup controls toughness and strength in FFF-printed PLA, providing insights into customizing mechanical characteristics through layer orientation. [111] Nabipour and Akhoundi explored the impact of FFF parameters, like layer thickness and infill density, on tensile strength in ABS/Cu composites. [112] These studies highlight the importance of infill patterns, which directly influence the structural integrity, energy absorption, and production efficiency in FFF processes.

The most common filling patterns are simple geometric structures, that allow durable construction combined with high print speeds, such as grid, straight, honeycomb and cubic. These patterns have the advantage of the possibility to lighten the printed parts by reducing the infill density, but they have as drawback that none of them have the characteristic of being isotropic, so an in-depth study of design for manufacturing is required if certain mechanical characteristics must be respected.

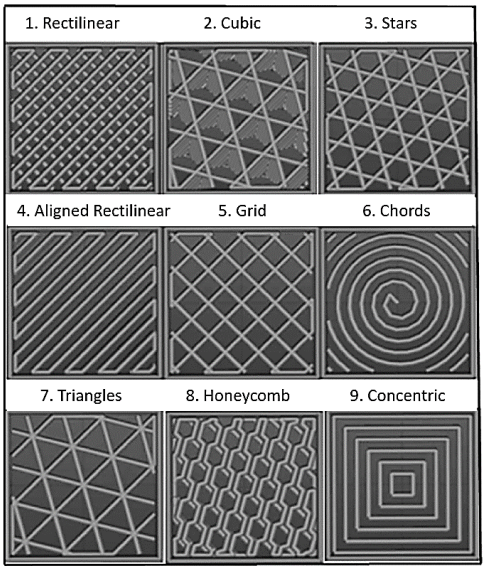

Figure 2.12: The most common infill patterns for FFF process.

As explained in paragraph 2.2.1, the degree of anisotropy in FFF-printed parts is primarily caused by the weak adhesion between layers along the build direction (z axis), and is heavily influenced by process parameters such as layer height, raster angle, printing speed, and nozzle temperature [113], [114], [115], [116]. To achieve specific mechanical properties in a 3D printed component, particularly in relation to load-bearing directions, it is crucial to properly orient the part within the print volume during both the design and slicing stages. [117] [118] This consideration often requires a thorough analysis of the process parameters and may necessitate the use of additional materials for supports. Once the print is complete, these supports must be removed, which not only generates waste material but can also pose difficulties in removal, often requiring additional post-processing steps. These steps increase both the production time and the overall cost of the part.

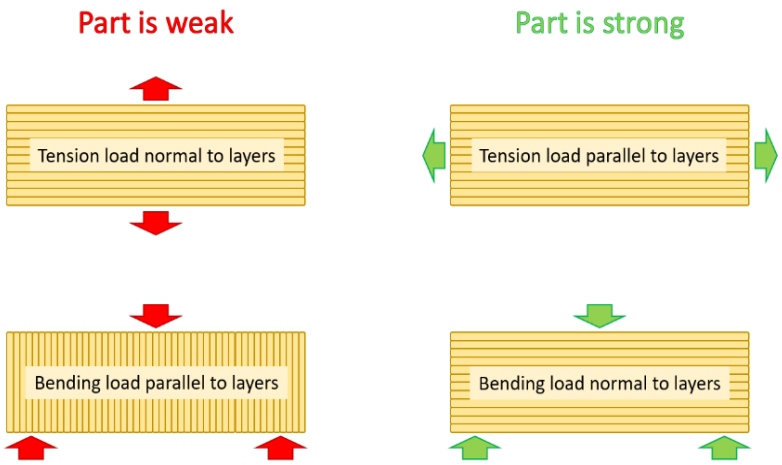

Figure 2.13: Mechanical anisotropy in 3D printed parts.

Among the most interesting infill patterns that have been implemented on slicing software, one of the best known is the gyroid. This structure exhibits an enhanced FFF manufacturability thanks to the fact that the wall inclination of the unit cells varies continually layer by layer, thus it is a self-supporting structure that does not require any additional supporting material. [119] Gyroid infill pattern was inspired by a 2017 MIT study, where researchers designed one of the strongest and lightest materials available using graphene [120].

The gyroid structure is mathematically-defined by trigonometric functions (Eq.3) that satisfy the equation Eq.4 [121]:

$$\Phi(\mathrm{x},\mathrm{y},\mathrm{z}) = \sin(\omega_x\, x)\cos(\omega_y y) + \sin(\omega_z z)\cos(\omega_x x) + \sin(\omega_y y)\cos(\omega_z z) \qquad \text{Eq.3}$$

$$\Phi(\mathrm{x},\mathrm{y},\mathrm{z}) = \mathrm{K} \qquad \text{Eq.4}$$

Where:

$\mathrm{x},\mathrm{y},\mathrm{z}$ are the Cartesian coordinates

$\omega_x, \omega_y, \omega_z$ are the cell frequencies in the x,y,z directions respectively

The surfaces thus defined divide the space into two domains whose volume fractions can be varied by adjusting the value of K. When K is equal to 0 the two volumes are identical. [122] The mathematically defined gyroid unit cells expand isotropically in all three dimensions (x, y, z) which, in contrast to all other patterns, means that it has the same resistance in all directions. [123].

While gyroids inherently possess isotropic properties, this can be compromised by the intrinsic anisotropy of the material used (such as in composites) and by the anisotropic nature of FFF technology. However, by carefully optimizing the process parameters in such a way as to obtain the best possible interlayer adhesion and the best balance between the unit cell size and the stresses to be supported, the gyroid infill pattern could significantly reduce, and in some cases, nearly eliminate, the anisotropy typically found in 3D printed parts.

Nowadays, the gyroid infill is attracting a lot of interest in the biomedical field for the 3D printing of artificial bones, scaffolds for regenerative medicine, and orthopedic implants [124] [125] [126] but it could be very promising for several application fields such as aeronautics, aerospace, automotive, transportation and defense. The advantages of applying it to 3D printing for aerospace and aeronautical purposes are: a very good combination of high strength and low printing time; almost isotropic strength in all directions (x,y,z); excellent energy absorption capability and high fracture toughness; high compressive and tensile strength despite less density and material usage (in comparison to other infill patterns) [127] [128]. Thus, the final result is a 3D printed part with high strength-to-weight ratio. Moreover, it was studied that the mechanical responses of gyroid lattice structures depend above all on the geometric characteristics of

the unit cells and not only on the material they are made of [129]. It was found that the compressive strength is mainly affected by cells volume fraction (i.e. infill density), cell size, wall thickness and the inclination angle of the struts with respect to the axial direction [121], [130], [131], [132]. The main conclusion is that the smaller and denser the structures, the greater the mechanical performances.

It is well known that gyroids have an extraordinary ability to absorb energy thanks to their geometric complexity. [133] During an impact, the structure distributes the forces over a larger surface, reducing pressure peaks in specific areas and preventing catastrophic failure. [134] This makes them ideal for scenarios where dynamic stress resistance is required. In addition to absorbing physical impact energy, gyroid structures can be used to absorb acoustic and vibrational energy, reducing mechanical vibrations and noise. [135] This also makes them useful in acoustic applications or improving comfort in vehicles. The possibility of regulating the porosity of the gyroid structures allows to save material without compromising the mechanical resistance. This aspect is advantageous from an economic point of view, especially for expensive materials or in advanced applications where weight reduction is critical.

In order to develop sandwich structures that have certain properties for specific purposes, such as impact resistance or energy absorption, it is important to first study their mechanical behavior by varying some parameters like core geometries and volumetric densities. In this thesis work, the compressive behavior of FFF-printed gyroid lattice structures was well analyzed, also along the x and y directions, varying cell size and solid volume fraction, to evaluate which solution is more suitable for the realization of a sandwich panel with gyroid core to be tested by low-velocity impact test.

3 Materials and Methods

In this chapter, the materials and 3D printers used for this research study are presented explaining their main features and properties. Furthermore, the experimental setup for atmospheric plasma treatment and instrumentation used for thermal, chemical, mechanical and microscopic characterizations are briefly described.

3.1 Materials

3.1.1 Polyether(ether ketone) - PEEK

Among the most interesting high-performance thermoplastic materials, the class of *polyaryletherketones* (PAEK) [27] and their derivatives are experiencing growing use in the field of 3D printing thanks to the development of advanced 3D printers that allow their processability. Polyarylether- ketones are obtained by joining phenylether groups with phenylketone groups and both the percentage ratio and the way in which these two groups are arranged in the final polymer identify the various constituents of this family and their respective properties. In Table 3.1 different PAEK with their chemical structure are listed.

The amount of ketone groups in the main polymer chain greatly influences the final PAEK properties, increasing both the melting temperature (Tm) and the glass transition temperature (Tg). [136] In fact, the Ph-(C=O) bonds in ketone group are less flexible than Ph-O in ether one, thus the macromolecular chains rigidity increases and consequently the Tg as well. This limited chain mobility also reduces the degree of crystallinity of the final polymer that generally can reach a maximum of 40% obtainable only in very controlled process conditions (high melt temperatures and low cooling rates). If the polymer experiences rapid cooling conditions it is also possible to determine the total absence of crystals and a consequent 100% amorphous phase. Polyether(ether ketone) thanks to its high ether-to-ketone ratio is semi-crystalline, reaching 35% of crystallinity in optimum cooling conditions, instead Polyether (ketone ketone) is less crystalline and it is commonly found in its amorphous state.

Considerable care is required in PEEK processing because the degree of crystallization and crystalline morphology (structure), influence a lot the mechanical properties of

produced components. In addition, it exhibits greater shrinkage variations than amorphous PEKK. [137] Therefore, the 3D printing of PEEK is more complex and requires in-depth study for the choice of the process parameters if the objective is to obtain a part with reduced presence of defects (voids, warpage, shrinkage) and residual stresses, but optimized physical-chemical and structural characteristics.

Functional groups a) Phenylether group 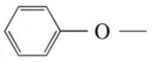 b) Phenylketone group 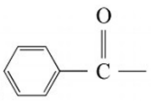		
Polymeric structure	**Name**	**a) : b)**
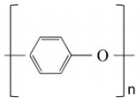	Polyphenylether (PPE)	1 : 0
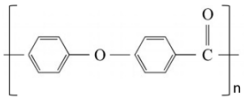	Polyetherketone (PEK)	1 : 1
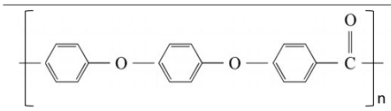	Polyether(etherketone) (PEEK)	2 : 1
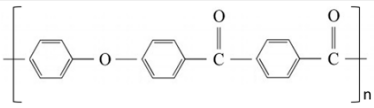	Polyether(ketoneketone) (PEKK)	1 : 2

Table 3.1: Chemical structure of different PAEK with their ratio of Phenylether and Phenylketone groups.

The integration of fibers into polymer matrices represents a transformative approach in material extrusion additive manufacturing. The mechanical and physical properties of fiber-reinforced composites are closely linked to the aspect ratio, orientation, and interfacial bonding of the reinforcing fibers. [138] [139] Longer fibers generally lead to superior mechanical properties, such as higher tensile and flexural strength, by bridging stress zones within the polymer. [140], [141] However, the use of long fibers introduces processing challenges, including nozzle clogging and uneven deposition, particularly in fused filament fabrication (FFF) methods. [34], [106] Continuous fiber-reinforced composites, often fabricated from continuous fibers embedded in thermoplastic matrices, demonstrate exceptional mechanical performance but are limited in printability. These limitations stem from a narrow range of processing parameters, fiber dislocation, poor matrix wetting, and the need for post-processing to achieve adequate fiber-matrix adhesion. [140]

In contrast, short fiber-reinforced polymers provide a balance between performance and manufacturability, especially in material extrusion AM. Short fibers enhance processability due to their reduced impact on viscosity and their compatibility with standard extrusion equipment. While composites with short fibers exhibit lower mechanical performance compared to those with continuous fibers, they offer advantages such as recyclability, ease of dispersion, and minimized fiber dislocation. When polymers loaded with carbon fibers are used, it must be taken into account that they confer anisotropic properties, in particular the highest mechanical performances will be along the direction of the printed bead. This phenomenon is obvious for continuous fibers but also applies to short (chopped) fibers. The latter, despite being uniformly dispersed within the matrix, tend to align both during the manufacturing of the filament by extrusion, due to shear forces, and when the filament is extruded from the nozzle during printing. [142]

The rheological behavior of fiber-reinforced polymers is critical for successful extrusion and part quality. Carbon fibers, a common reinforcement choice, significantly alter the flow properties of the polymer matrix. Their inclusion increases viscosity by restricting polymer chain mobility, with the extent of this effect influenced by fiber volume fraction, size, and aspect ratio. Long fibers tend to amplify viscosity due to their larger surface area and potential for entanglement, whereas short fibers exert a more moderate influence, simplifying processing. Despite these challenges, carbon fibers improve shear-thinning behavior, enabling the material to flow more readily under high shear rates during extrusion while maintaining stability post-deposition. They also reduce the coefficient of thermal expansion (CTE) avoiding common issues like die swell and warping by limiting polymer shrinkage during cooling. [143]

Chemically, carbon fibers enhance the thermal stability and environmental resistance of composites. [144] Acting as physical barriers, they slow the diffusion of gases and chemicals, increasing the material's durability in harsh conditions. However, achieving optimal chemical performance depends on strong fiber-matrix bonding. Techniques such as surface treatments, pre-impregnation, and fiber sizing are often employed to improve interfacial adhesion, ensuring the mechanical and chemical benefits of the reinforcement are fully realized. [145] [146] [147]

By carefully balancing fiber type, size, and processing parameters, manufacturers can achieve tailored mechanical, rheological, and chemical properties, enabling the production of high-performance components.

In particular, this research study focuses on the printing process of pristine Polyether(ether ketone) (PEEK) and Carbon-PEEK that is PEEK filled with chopped carbon fibers. The chosen materials are PEEK and Carbon PEEK CF10 (with 10% of chopped carbon fibers) purchased from Roboze. Roboze PEEK is one of the most resistant industrial plastics to chemical agents (organic substances, acids and bases), wear and abrasion; it offers high performance in terms of robustness, resistance to fatigue and a continuous use temperature of 240°C. Carbon-PEEK adds further thermal stability and rigidity to PEEK. The addition of carbon fibers improves the mechanical properties of the material and increases the Heat Deflection Temperature (HDT), while maintaining the properties unchanged even at higher temperatures compared to pure PEEK. Thanks to these characteristics, PEEK and Carbon-PEEK are very interesting for the production of final parts for lightening purposes or tools (such as molds) of particular shapes that can be used for the creation of epoxy matrix composite parts that require polymerization cycles in an autoclave.

Below are listed their physical and mechanical characteristics taken from the supplier datasheets. [148] [149]

PEEK

	MECHANICAL PROPERTIES	Test Method	Build Orientation		Infill density
			xz	xy	
TENSILE	Tensile Strength Ultimate	ASTM D638	89 MPa	86 MPa	100%
	Tensile Modulus	ASTM D638	3.4 GPa	3.3 GPa	
	Tensile Elongation at Break (%)	ASTM D638	3.78	3.62	
FLEXURAL	Flexural Strength (at yield, 23°C)	ASTM D790	-	120 MPa	100%
	Flexural Modulus (at 23°C)	ASTM D790	-	3.5 GPa	

THERMAL PROPERTIES	Test Method	Value
Glass Transition temperature [°C]	ISO 11357-2	143°C
Heat Deflection (HDT) with load of 1.82 MPa	ISO 75	160°C
Melting Point DSC	ISO 11357-3	343°C
Continuous Use Temp.	UL 746 B	240°C

OTHERS	Test Method	Value
Density	ISO 1183	1,30 g/cm3
Water Absorption	ISO 62	0,45 %
Volume Resistivity	IEC 60093	1,00 e+16 ohm*cm
Flammability behaviour test method	UL 94	V-0

Carbon-PEEK

	MECHANICAL PROPERTIES	Test Method	Build Orientation		Infill density
			xz	xy	
TENSILE	Tensile Strength Ultimate	ASTM D638	120 MPa	115 MPa	100%
	Tensile Modulus	ASTM D638	13.8 GPa	14 GPa	

THERMAL PROPERTIES	Test Method	Value
HDT (load 1.82MPa)	ISO75	280°C
Continuous Use Temp.	UL 746B	250°C
Maximum (short term) Use Temp.	UL 746A	280°C

OTHERS	Test Method	Value
Specific Gravity	ISO 1183	1,36 g/cm3
Water Absorption	ISO 62	< 0,1%
Surface Resistance	DIN IEC 60093	< 10^9Ω

3.1.2 Polycarbonate - PC

Another engineering material, less performing than PEEK but interesting for industrial use, is Polycarbonate (PC), an amorphous thermoplastic having aromatic groups in the main chain alternating with carbonate functionalities (−O−(C=O)−O−). Its chemical structure is represented in Figure 3.1. Polycarbonates used in engineering are strong, tough materials, and generally optically transparent. [150]

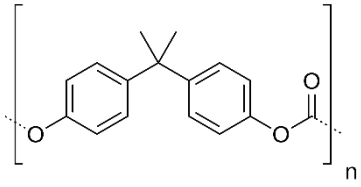

Figure 3.1: Repeating chemical structure unit of Polycarbonate.

This material has some similarities to PEEK in terms of processability difficulty, having a glass transition temperature of 145°C and a recommended extrusion temperature of 280-300°C. Other issues encountered in PC 3D printing occur due to difficult adhesion with print bed and tendency to warp during printing. For this reason, it was chosen, in addition to PEEK, to study how to improve interlayer adhesion via plasma surface treatments. The Polycarbonate chosen for this study is the Kimya PC-S filament. It offers high resistance to heat up to 140°C.

Below are listed Kimya PC-S physical and mechanical characteristics taken from the supplier datasheets. [151]

FILAMENT PROPERTIES

DESCRIPTION	TEST METHODS	UNITS	VALUES
Diameter	INS-6712	mm	1.75 ± 0.1
Density	ISO 1183-1	g/cm³	1.193
Moisture rate	INS-6711	%	< 1
Melt Flow Index (MFI) (@260°C – 5 kg)	ISO 1133-1	g/10min	25.5
Glass transition temperature (Tg)	ISO 11357-1 DSC (10°C/min - 20-410°C)	°C	140

PRINTED SPECIMENS PROPERTIES

	PROPERTIES	TEST METHODS	UNITS	VALUES
MECHANICAL PROPERTIES	Tensile modulus	ISO 527-2/5A/50	MPa	2,172
	Tensile Strength	ISO 527-2/5A/50	MPa	53,8
	Tensile strain at strength	ISO 527-2/5A/50	%	3,7
	Tensile stress at break	ISO 527-2/5A/50	MPa	44,6
	Tensile strain at break	ISO 527-2/5A/50	%	4,8
	Flexural modulus	ISO 178	MPa	1,640
	Flexural stress at conventionnal deflection (3,5% strain)**	ISO 178	MPa	67,7
	Flexural strength	ISO 178	%	>5*
	Charpy impact resistance	ISO 179-1/1eA	kJ/m²	7,9
	Shore Hardness	ISO 868	Shore D	79,2

*According to ISO 178, end of the test at 5% deformation even if there is no specimen break

** The data should be considered as indicative values - Properties can be influenced by production conditions.

3.2 Industrial 3D printers

PC can be extruded using a common printer such as the Ultimaker S5, while the printing process of PEEK presents a unique challenge due to its high melting point of 343°C. This characteristic necessitates the use of high-performance industrial 3D printers specifically designed to handle such demanding temperatures. These advanced machines are equipped with robust heating systems and precise temperature controls to ensure consistent melting and extrusion of PEEK. This capability is crucial for achieving optimal material properties and dimensional accuracy, which are essential for applications in aerospace, automotive, and medical industries where superior mechanical strength and thermal stability of PEEK are leveraged. Investing in high-performance 3D printing technology for PEEK not only ensures reliable production but also unlocks the full potential of this polymer, paving the way for innovative and high-quality applications.

The printer used for the first part of the present research is a Roboze Argo 500 (Figure 3.2a). It is an advanced machine designed for industrial applications, known for its ability to print high-performance polymers and composite materials. It has a large build volume of 500 x 500 x 500 mm^3, making it suitable for producing large parts or multiple smaller parts in a single print run. In addition, it is equipped with a heated chamber (up to 180°C) and a high-temperature extruder capable of reaching up to 500°C. This enables the processing of high-performance materials that require high extrusion temperatures for optimal results. The Roboze Argo 500 offers repeatable and high-precision 3D production (precision of 10 µm) thanks to the patented *Roboze Beltless System* technology which replaces the rubber belts commonly used in the sector with mechatronic movement. The inserted mechatronic handling ensures 25 microns of construction on the X and Y axes.

For the second part of this study, having used Carbon-PEEK as feeding material, a printer of smaller size and performance was used, the Roboze One+400 (Figure 3.2b). This is because, as mentioned in the previous paragraph, the thermal stability of Carbon-PEEK allows us to produce specimens with good precision without them deforming in the absence of a hot chamber. The differences compared to the Roboze Argo 500 are: heated print bed, unheated chamber and overall print volume of 300 mm x 200 mm x 200 mm (xyz). The heated printing bed in anticorodal 6082 with satin finish treatment is able to

reach 130°C for printing and holding the most complex technopolymers, guaranteeing thermal stability and adhesion.

(a) (b)

Figure 3.2: Roboze 3D printing machines: Argo 500 (a) and One+400 (b). [152]

3.3 Piezoelectric Direct Discharge (PDD) plasma

Piezoelectric Direct Discharge (PDD) atmospheric plasma technology is an advanced method for generating low-temperature plasma at atmospheric pressure. [153] The core principle behind this technology is the use of a piezoelectric element to induce a discharge, which ionizes a gas - typically air or another process gas - creating a cold plasma. In this process, an alternating electrical signal is applied to a piezoelectric material, causing it to vibrate at high frequencies. These vibrations generate a rapid electrical discharge between the electrodes within the plasma device, which in turn ionizes the surrounding gas molecules. The ionization process produces a mixture of electrons, ions, and reactive species such as oxygen radicals, enabling the plasma to interact with material surfaces. [154]

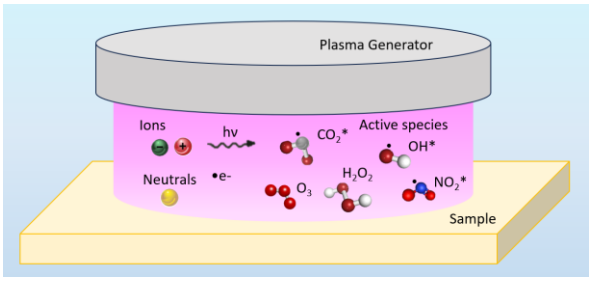

Figure 3.3: Reactive species in cold atmospheric plasma.

This technology is particularly useful because it operates at room temperature and atmospheric pressure, eliminating the need for complex vacuum systems. The generated plasma is "cold," meaning that the temperature remains low enough to treat heat-sensitive materials without damaging them. Cold atmospheric plasma is highly effective for a wide range of surface treatments, including cleaning, activation, and functionalization of various materials. [155] By modifying the surface chemistry, plasma can enhance adhesion properties, prepare surfaces for bonding or coating, and remove contaminants without using aggressive chemicals. PDD is primarily used in open discharge systems for treating non-conductive surfaces. Although PDD shares some characteristics with corona and dielectric barrier discharges, its uniqueness lies in the initiation of micro-discharges directly on the surface of the ceramic material, giving it distinct physical properties and a wide range of application possibilities.

The device used in this research is the Piezobrush PZ3 plasma torch, a compact and portable tool designed for small-scale and targeted plasma treatments. This device is built around the principle of piezoelectric direct discharge, enabling the generation of cold plasma from air or other gases without the need for an external gas supply. The discharge is produced using a piezoelectric cold plasma generator (PCPG), the CeraPlas F, which features a resonant piezoelectric transformer (RPT) capable of producing a voltage transformation ratio greater than 1000. This allows the generator to achieve output voltages exceeding 10 kV, while the input voltage remains below 25 V.

Figure 3.4: Piezobrush® PZ3 plasma torch, used for the present research work. [86]

In Korzec [153] overview, the key designs of PDD-based discharges are introduced, and the Piezobrush PZ3 torch is well described with a focus on the fundamental operational principles, critical performance characteristics, and examples of applications that take advantage of the unique properties offered by this plasma discharge. In addition, a description of the variation of the activation area as a function of various parameters is reported. In particular, the authors found a monotonous increase of the activation area with treatment time until a saturation of the area values for longer times is reached. The activation area can be maximum of 26 mm, even by a prolonged treatment time. The relationship between the activation area and the distance from the plasma source is also examined. The peak activation area occurs near the nozzle, specifically within a range of 1,5 to 3,5 mm from the tip of the CeraPlas F. The activation area diminishes as the distance increases beyond 3,5 mm. All these considerations were taken into account when the design of experiment of the present research work was studied.

CeraPlas F	
Operating frequency	50 kHz
weight	8 g
Length x width x thickness	72 x 6 x 2,8 mm^3
Piezoelectric material	PZT
Maximum operating power	8 W
Input capacity C_{in}	~ 2 µF
Output capacity C_{out}	~ 3 pF

Table 3.2: Parameters of the CeraPlas™F PCPG. [153]

The Piezobrush PZ3 is particularly suitable for delicate applications, such as the treatment of polymer surfaces, biomedical samples, or sensitive electronics. [156] Its low-temperature plasma ensures that materials are not exposed to excessive heat, making it ideal for applications where surface activation or cleaning is needed without the risk of thermal damage. Additionally, the PZ3 is user-friendly, offering ease of operation in laboratory or industrial environments, and provides an efficient, eco-friendly alternative to chemical treatments or high-energy plasma sources.

Overall, piezoelectric direct discharge atmospheric plasma technology plays a crucial role in modern surface engineering and treatment applications, combining the benefits of cold plasma generation with the simplicity of piezoelectric-driven discharge at atmospheric conditions.

3.4 Characterization Methods

3.4.1 Differential Scanning Calorimetry - DSC

Differential Scanning Calorimetry (DSC) is a thermal analysis technique used to measure how heat capacity of a material changes with temperature. The sample and a reference material are placed in two distinct holders (called "pans") in a DSC furnace, where the temperature is changed in a controlled manner. Often, the reference holder is left empty. In a DSC experiment, the sample and the reference are heated at a controlled rate under inert conditions (nitrogen flow), and the heat flow required to maintain the same temperature in both pans is recorded. The temperature difference between the sample and the reference is then measured as a function of the applied temperature, providing information on thermal transitions such as melting, crystallization, and glass transition.

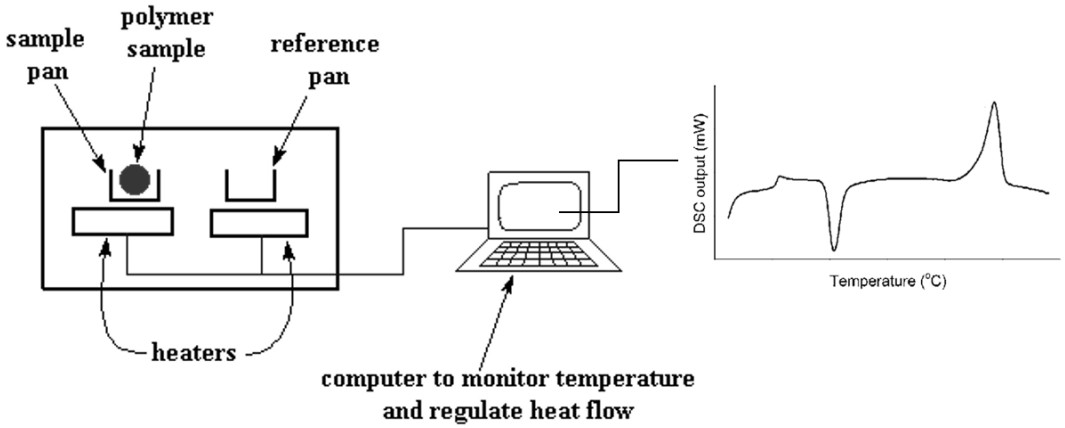

Figure 3.5: Scheme of DSC experimental setup. [157]

These transitions reflect changes in the physical state or structure of the material as it is heated or cooled. The principal transitions include:

- *Glass Transition (Tg)*: this is a second-order transition observed in amorphous or semi-crystalline materials like polymers. It represents the temperature at which a material transitions from a hard, glassy state to a softer, rubbery state. During Tg, there is no latent heat involved, so it appears as a step change in the heat capacity (baseline shift) on a DSC scan.

- *Melting Point (Tm)*: this first-order transition occurs in crystalline or semi-crystalline materials and represents the temperature at which a solid material melts into a liquid. It shows up as an endothermic peak, where heat is absorbed as the crystalline regions break down.

- *Crystallization (Tc)*: this is an exothermic process where the material cools and transforms from a disordered (amorphous) state into a more ordered (crystalline) structure. This typically appears as an exothermic peak during cooling after the material has been melted.

- *Cold Crystallization (Tcc)*: In some polymers, crystallization may occur upon reheating, rather than during cooling. This is referred to as cold crystallization, and it shows up as an exothermic peak during the heating cycle after glass transition and before the crystallization temperature.

- *Decomposition*: at high temperatures, materials may start to chemically decompose. This is often accompanied by a significant endothermic or exothermic signal, depending on the decomposition process. It usually appears as a large, broad peak at the higher end of the temperature range.

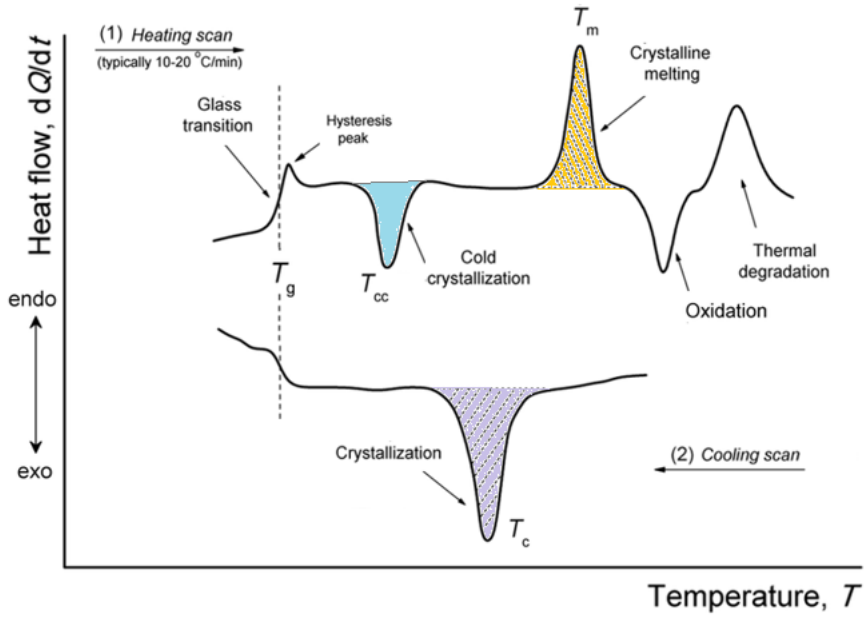

Figure 3.6: Typical DSC scans for a semicrystalline polymer.

Each of these transitions provides valuable insights into the thermal behavior and stability of materials, aiding in their characterization and optimization for various applications. DSC is widely used to characterize the thermal properties of polymers, helping to assess material stability, phase transitions, composition and heat capacity. All these information allow to identify the type of material (thermoplastic/thermoset, amorphous/crystalline). For semicrystalline polymers, is it also possible to calculate the degree of crystallinity (χ) from the enthalpies of endothermic and exothermic peaks using the following equation: [158]

$$\chi = \frac{\Delta H_m - \Delta H_{cc}}{\Delta H_m{}^{100\%}} \cdot 100\% \qquad \text{Eq. 5}$$

where:

χ is the crystallinity degree (%);

ΔH_m is the melting Enthalpy (J/g);

ΔH_{cc} is the Enthalpy related to the cold crystallization (J/g);

$\Delta H_m{}^{100\%}$ is the melting Enthalpy of PEEK with χ value equal to 100% (it is about 130 J/g).

Figure 3.7: The DSC 250 machine from TA instruments used for this thesis work. [159]

3.4.2 Optical Microscopy

The optical microscope is a widely used tool in material science, and various other fields, for magnifying small objects and structures that are invisible to the naked eye. By using visible light and a series of lenses, it allows detailed observation of a sample's surface

and internal features, often down to the micrometer or sub-micrometer scale. Optical microscopes are very useful for examining material surfaces and characterizing microscopic structures such as fibers, grains, and defects in engineering materials. The imaging by optical microscopy is most commonly performed in either reflection or transmission modes.

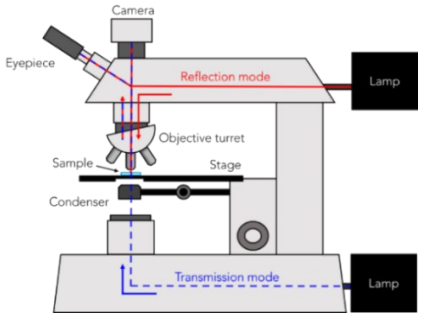

Figure 3. 8: Scheme of operation of an optical microscope. [160]

In reflection mode microscopy, light is directed onto the surface of the sample, and the reflected light is collected and analyzed to produce an image. This mode is particularly useful for studying opaque or reflective samples, such as metals, semiconductors, plastics or ceramics. Unlike transmission mode, where light passes through a transparent sample, reflection mode captures light bouncing off the surface, revealing details about surface topography, texture, and microstructure. This technique is often used for inspection and failure analysis of materials.

In this study a Hirox RH – 2000 digital Optical Microscope was used in reflection mode to examine the surfaces of the samples and evaluate the presence of voids and defects, the alignment of the carbon fibers in the 3D printed samples and the failure modes of the mechanically tested samples.

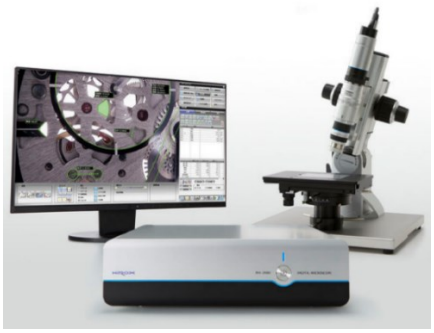

Figure 3.9: Hirox RH – 2000 digital Optical Microscope. [161]

3.4.3 Scanning Electron Microscopy

Scanning Electron Microscopy (SEM) is a powerful imaging technique that employs a focused beam of electrons to produce highly detailed images of a material's surface. Unlike conventional optical microscopes, which rely on visible light to magnify objects, SEM uses electrons to interact with the surface of a sample. This approach allows for significantly greater resolution (typically ranging from 1 to 20 nanometers, depending on the instrument and operating conditions) and depth of field, revealing the complex features of surface topography at the micro and nanoscale. The resolution is influenced by several factors, such as the accelerating voltage of the electron beam (typically it ranges between 1 and 30 keV), the working distance, and the nature of the sample itself. Higher accelerating voltages often yield better resolution but can also increase the risk of sample damage, especially in delicate or non-conductive materials. The latter are more difficult to analyze due to charging and beam damage, for this reason it is necessary to deposit a thin metallic coating (e.g. gold) by sputtering and grounding the sample before the analysis.

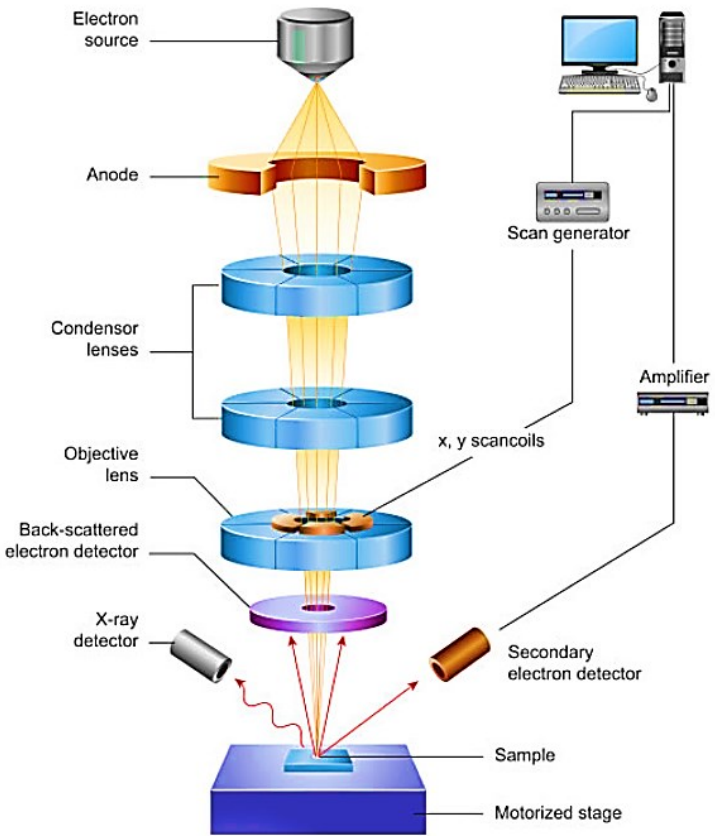

Figure 3.10: Schematic representation of a scanning electron microscope. [162]

The process begins with the emission of a high-energy electron beam generated by either a thermionic emitter (such as tungsten or LaB_6 filament) or a field emission gun (FEG). FEGs provide the highest resolution due to their small spot size. Electromagnetic lenses focus the electron beam generated from the filament on the surface of sample. To prevent electron scattering and contaminations, the sample is located in a high vacuum chamber. As the electrons make contact with the surface, they interact with the atoms, generating various signals, including secondary electrons, backscattered electrons, and X-rays. These signals are captured by specialized detectors, which convert them into detailed images that provide valuable insights into the sample's surface structure, composition, and other key properties. The secondary electron detector (SE) is the most common, providing detailed topographical information by collecting low-energy electrons emitted from the surface. For compositional contrast, the backscattered electron detector (BSE) captures high-energy electrons that reveal atomic number differences, with heavier elements appearing brighter. The energy dispersive spectroscopy (EDS) detector measures X-rays emitted from the sample, enabling elemental analysis and mapping. Additional detectors like cathodoluminescence (CL) and electron backscatter diffraction (EBSD) provide insights into optical properties and crystallographic structure, respectively, while in-lens detectors in advanced SEMs allow high-resolution surface imaging.

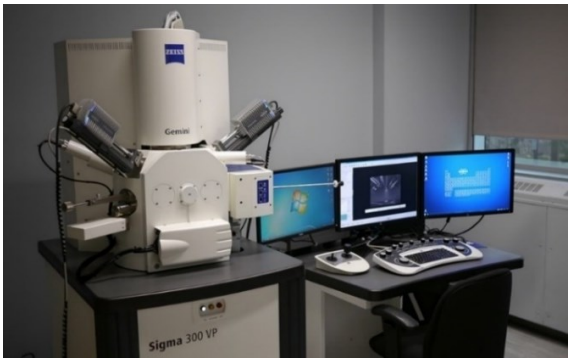

Figure 3.11: High-resolution Field Emission Scanning electron microscope (SEM), ZEISS Sigma 300 VP, used in the present thesis work. [163]

SEM finds extensive use in a range of fields. In material science, it is indispensable for studying the surface morphology and microstructure of diverse materials, from metals to advanced polymers, often in three-dimensional detail. Additionally, in the field of nanotechnology, SEM allows researchers to closely examine nanoscale materials like nanoparticles and nanowires, shedding light on their unique properties and potential

applications. In both research and industry, SEM serves as an essential tool for uncovering the fine details of a material's surface, playing a critical role in innovation, quality control, and scientific discovery.

3.4.4 Fourier Transform Infrared Spectroscopy

Fourier Transform Infrared (FT-IR) spectroscopy is a powerful analytical technique used to identify chemical compounds by measuring the infrared light absorbed by a sample. Infrared light causes the vibrational transitions in molecular bonds, and each type of bond produces a characteristic absorption spectrum. This technique uses interferometry to record information about a material placed in the IR beam An FTIR spectrum is generated by converting interferograms into identifiable spectra. Patterns in spectra help identify the sample, since molecules exhibit specific IR fingerprints, FT-IR enables the detection of them, making it an essential tool for identifying materials, analyzing chemical structures, and monitoring changes in composition. The Fourier Transform produces spectra that can be utilized by analysts for material identification or quantification.

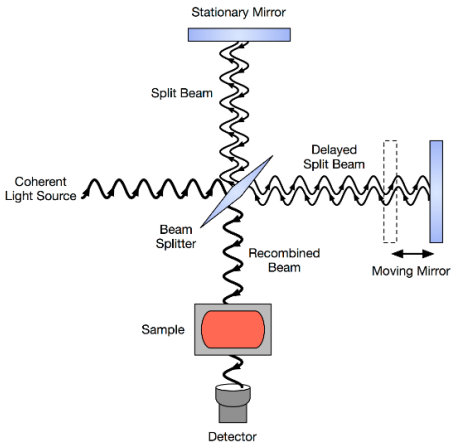

Figure 3.12: A schematic representation of a Michelson's interferometer used in FTIR spectroscope. [164]

In FT-IR spectroscopy, the sample is exposed to a broad range of infrared light, typically between 400 and 4000 cm^{-1} corresponding to mid-infrared frequency range. The resulting absorption spectrum is transformed using Fourier transform mathematics to provide detailed information about the molecular structure of the sample. This technique is widely used in materials science, chemistry, and biology for applications such as quality control, environmental analysis, and pharmaceutical development.

Range	Wavelength (μm)	Frequency (cm^{-1})	Molecular interactions
Near Infrared (NIR)	0,7-2,5	14285-4000	Electronic transitions in atoms and molecules; combinations and overtones of vibrational modes
Mid Infrared (MIR)	2,5-25	4000-400	Fundamental vibrational modes of molecules; rotational modes of gases
Far Infrared (FIR)	25-1000	400-10	Group vibrational modes of molecules and lattices; fundamental vibrational modes

Table 3.3: The principal divisions of the infrared spectrum.

One of the most common modes of FT-IR analysis is Attenuated Total Reflectance (ATR), which allows for easier sample preparation and analysis. In ATR mode, the infrared light is deflected towards a crystal with a high refractive index, typically diamond or zinc selenide. The light reflects off the internal surface of the crystal at the point where the sample is in contact, penetrating only a few microns into the sample and creating an evanescent wave. When the sample absorbs energy of particular wavelength in the IR spectrum, the evanescent wave experiences attenuation. The attenuated beam travels back to the crystal, exits from the opposite side, and is then directed toward the detector of the infrared spectrometer. The detector receives IR signals as interferograms which are converted into peaks of the IR absorption (or transmission) spectrum using the Fourier transform.

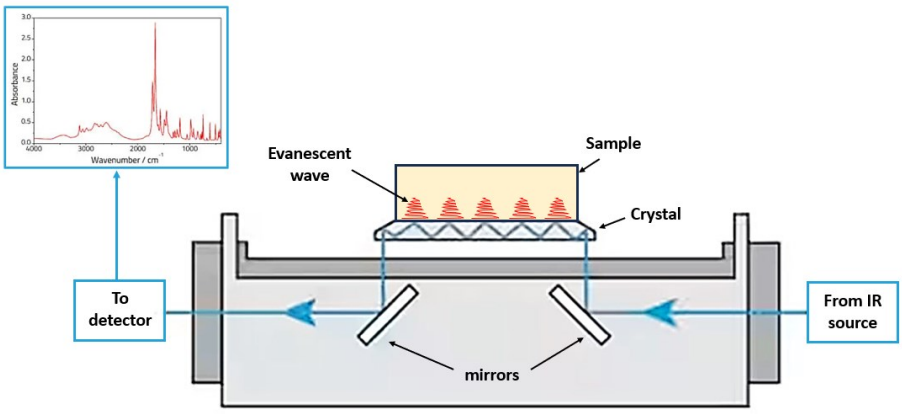

Figure 3.13: Schematic representation of ATR FTIR operating mode.

ATR-FTIR is particularly useful because it requires minimal or no sample preparation, and it is capable of analyzing solids, liquids, and gels without complex sample handling. This makes ATR ideal for analyzing hard-to-handle materials like powders or polymers.

For solid samples, they are often pressed into a thin film or mounted directly on the ATR crystal. Liquid samples can be placed directly on the crystal without dilution, while powders are typically compacted or pressed to ensure good contact with the crystal surface. The simplicity of sample preparation, combined with the high sensitivity of the ATR-FTIR method, makes it a highly versatile and efficient technique for characterizing a wide range of materials.

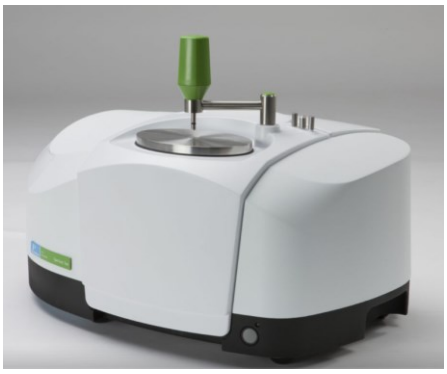

Figure 3.14: Spectrum Two PerkinElmer FTIR spectrometer used in this work. [165]

3.4.5 Tensile Test

A tensile test is a fundamental mechanical test used to determine how a material reacts when it is subjected to a uniaxial pulling force. The test provides crucial data about the strength, elasticity, and ductility of materials, making it essential in evaluating materials used in engineering, manufacturing, and construction.

The tensile specimen is usually shaped like a dog bone, with a wider grip section at both ends and a narrower gauge section in the middle. The gauge section is the critical area where the tensile test focuses, as it experiences the most stress and eventual failure. The dimensions of the specimen are standardized, often according to ASTM or ISO standards, to ensure consistency in testing and comparability of results. These standards dictate the sample's geometry, including its length, width, and thickness, depending on the material type. Typically, the ASTM D638 is the standard used for the tensile test of plastics, but

in our case, since the samples were printed layer by layer, it was preferred to follow the standard for composite laminates, the ASTM D3039.
Once the specimen is prepared, it is mounted in the grips of a tensile testing machine, which applies a controlled, increasing tensile load.

As the machine pulls the sample, it records the force applied and the elongation or strain in the material. The test continues until the sample breaks, and the machine records data throughout this process.

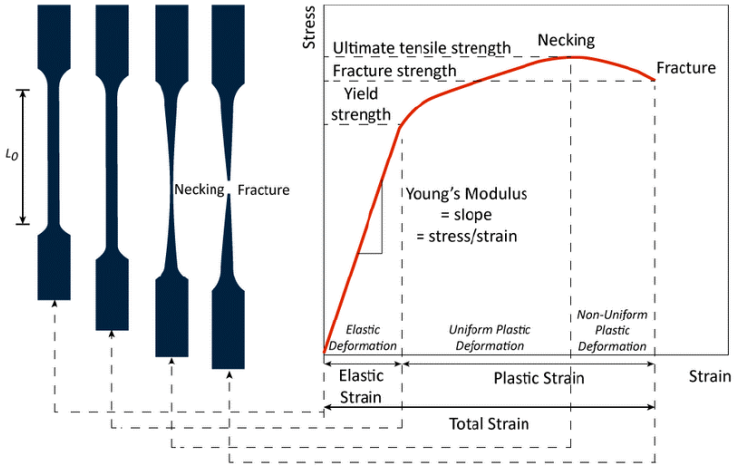

Figure 3.15: Tensile stress-strain curve and shapes of the specimen changing during test. [166]

Tensile testing is widely used to measure properties like tensile strength, yield strength, and elongation at break. Tensile strength, the maximum stress that the material can withstand before breaking, is a critical parameter for assessing the suitability of a material in load-bearing applications. Engineers and designers use this information to predict how materials will perform under real-world conditions, such as in bridges, buildings, or aircraft.

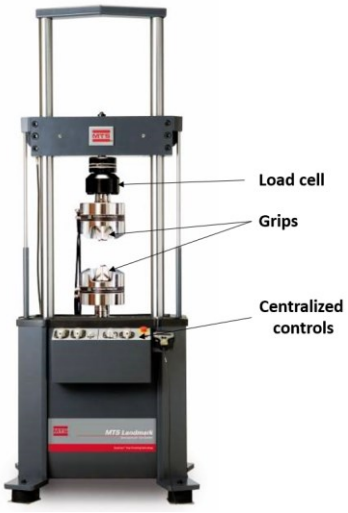

Figure 3.16: MTS machine, model 370.25 Landmark Load Frame, used in the present research study. [167]

Stress-strain curves are obtained considering the following definitions of Stress "σ" and strain "ε":

$$\sigma = \frac{F_i}{A_o} \qquad \text{Eq. 6}$$

$$\varepsilon = \frac{l_i - l_0}{l_0} = \frac{\Delta l}{l_0} \qquad \text{Eq. 7}$$

where:

F_i is the instantaneous load applied perpendicular to the specimen cross-section (in N)
A_0 is the original cross-sectional area before the application of load (in mm2)
l_i is the instantaneous gauge length
l_0 is the original gauge length before the application of load

The tensile strength is obtained from the maximum stress point corresponding to the maximum force (F_{max}) that the specimen withstood before failure. This calculation provides the tensile strength in megapascals (MPa), a standard unit for measuring material strength. The Young's modulus "E", that is the modulus of elasticity, is given by the slope of the initial linear part of the σ-ε curve before the yield point:

$$E = \frac{\sigma}{\varepsilon} \qquad \text{Eq. 8}$$

The tensile test offers essential insights into the mechanical behavior of materials, particularly their ability to endure tensile forces. It is indispensable in ensuring that materials used in critical applications meet the required strength and safety standards.

3.4.6 Single Lap Shear Test

The single lap shear test is a widely utilized method for evaluating the adhesive strength of bonded joints, particularly in composites and polymer-based materials. This test measures the shear strength of an adhesive bond between two substrates by subjecting the bonded specimen to a tensile force until failure occurs. The test is especially relevant in industries where materials are bonded together rather than mechanically fastened, such as in aerospace, automotive, and construction, as it provides critical insights into the load-bearing capabilities of bonds.

In preparing a specimen for the single lap shear test, two flat, rectangular strips of material are typically used. These strips, referred to as the adherends, are often composed of metal, composite, or polymeric materials, depending on the application being studied. The length of the overlap between the two strips is crucial for the test, as it directly influences the stress distribution during loading. The adherends are bonded together over a defined overlap area using an adhesive of interest. Precise control of bond line thickness is important to ensure uniform stress distribution across the bonded area. The adhesive is allowed to cure fully according to the manufacturer's specifications, and the specimen is then ready for testing.

Once the specimen is prepared, it is clamped into the grips of a tensile testing machine, which pulls the adherends in opposite directions, parallel to the bond line. As the tensile force increases, shear stress develops at the adhesive interface. The force at which the bond fails, or the maximum load sustained before failure, is recorded as the lap shear strength of the adhesive. The failure mode - whether cohesive (within the adhesive), adhesive (at the interface), or substrate failure - can provide further insight into the performance of the adhesive.

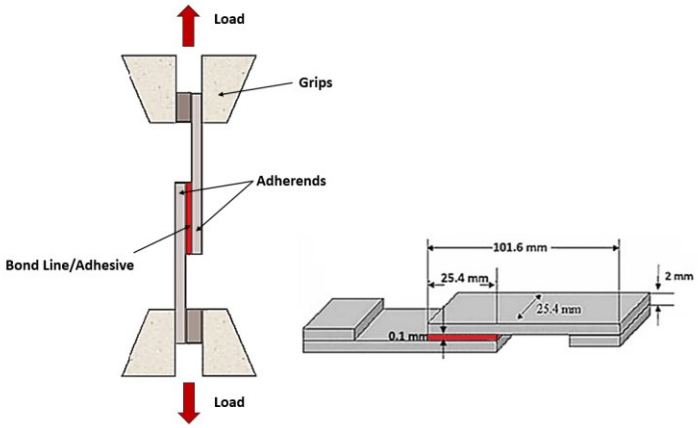

Figure 3.17: Typical shape of single lap shear specimen and scheme of testing set-up.

The single lap shear test is widely used for characterizing the mechanical properties of adhesive bonds because it mimics the real stresses that bonded joints may encounter in service. It is particularly useful for evaluating the shear strength of adhesives under various conditions, such as temperature, humidity, or aging, allowing engineers to select appropriate adhesives and bonding processes for their specific applications. Although the test provides valuable data, it should be noted that the stress distribution in the lap shear configuration is not uniform, leading to stress concentrations at the ends of the overlap, which can affect the interpretation of results. Nevertheless, the single lap shear test remains a fundamental technique for assessing adhesive performance and optimizing bonded joint designs.

3.4.7 Compression Test

A compression is a key mechanical test that helps to understand how materials respond when subjected to compressive forces. In this test, a material sample is subjected to controlled force until it deforms or fractures, allowing for the measurement of properties such as compressive strength, modulus of elasticity, and yield strength. The test provides insights into how materials perform under compressive stress, which is critical for applications where materials are expected to withstand squeezing or compressive forces, such as in structural components. The compression test of lattice structures is an essential method for assessing the mechanical properties of lightweight, cellular materials used in high-performance applications. Lattice structures, which are often designed with repeating geometric patterns, are employed in aerospace, biomedical, and automotive

industries due to their exceptional strength-to-weight ratio. The purpose of the compression test is to evaluate the mechanical stability and load-bearing capacity of the lattice under compressive forces, simulating conditions they may encounter in real-world applications. In this research study, different ASTM standard were considered. Initially, ASTM D695, the established testing method for the compressive characteristics of rigid plastics, was utilized to compare the mechanical compressive properties of lattice structures having different infill percentages and the 100% filled structures. Subsequently, the ASTM C365 - the standard test method for flatwise compressive properties of sandwich cores - was used to evaluate the compressive behavior of cubic samples in the x, y and z directions.

The specimen for a compression test consists of a prism/cubic or cylindrical lattice structure made from the material of interest. The dimensions and geometry of the lattice are carefully selected based on the intended application, as these parameters strongly influence the mechanical behavior under compression. To prepare for testing, the specimen is positioned between the plates of a universal testing machine. The plates apply a compressive force uniformly across the top and bottom surfaces of the lattice, gradually increasing until the structure deforms or fails. These are generally very complicated tests due to the fact that between the specimen and the machine plates the friction creates tangential tensions which introduce a three-dimensional state of tension (also creating the barreling phenomenon).

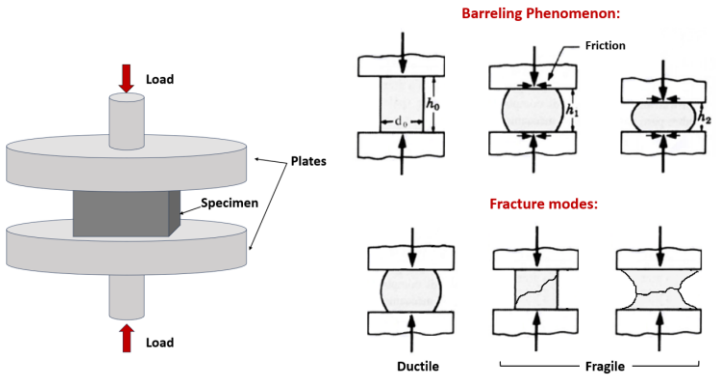

Figure 3.18: Compression test setup and compressive fracture modes.

During the test, load and displacement data are recorded to determine key properties such as compressive strength and elastic modulus. These properties, calculated using the same equations expressed for tensile strength and Young's modulus, are critical for

understanding how the lattice will perform under various loading conditions. The deformation behavior of the lattice is often of particular interest, as it can involve buckling, local collapse, or densification depending on the material and geometry. The failure mode - whether it is gradual collapse or sudden brittle failure - provides insight into the structural integrity and potential applications of the lattice.

Figure 3.19: Instron 5582 universal testing machine used for this research. [168]

Compression tests of lattice structures are useful in optimizing designs for lightweight, load-bearing components. By evaluating how different geometries and materials respond to compressive forces, it is possible to refine lattice designs for enhanced mechanical performance.

3.4.8 Impact Test

The low-velocity impact test using the drop-weight method is a crucial technique for assessing the impact resistance and damage tolerance of sandwich structures, which are widely used in aerospace, marine, and automotive industries. Sandwich structures typically consist of two stiff outer face sheets bonded to a lightweight, energy-absorbing core, such as a foam or honeycomb. These structures are designed to withstand dynamic loads while maintaining a low weight, making them ideal for applications where strength and stiffness are required alongside energy absorption capabilities. The drop-weight impact test simulates impact events, such as tool drops or debris strikes, by subjecting the sandwich structure to a controlled impact at low velocity.

Typically, in preparing the specimen for testing, a sandwich panel is fabricated with carefully chosen materials for the face sheets and core, as the material combination directly affects the impact performance. The panel is clamped securely within a fixture to prevent movement during the test. A drop-weight tower is used, in which a weight with a specified mass is raised to a set height and then released, striking the surface of the specimen with a known kinetic energy. Both the drop height and the weight of the impactor are modified according to the required impact energy.

Upon impact, the energy is transferred to the sandwich structure, causing stress waves to propagate through the material. Data such as impact force, deformation, and energy absorbed by the specimen are recorded. The typical representation of impact data is the Impact Force-Time history.

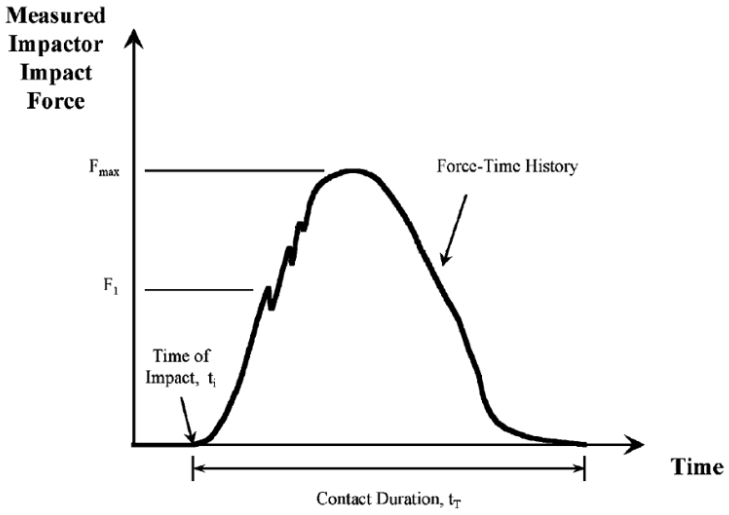

Figure 3.20: Impact Force vs time history from ASTM D7136.

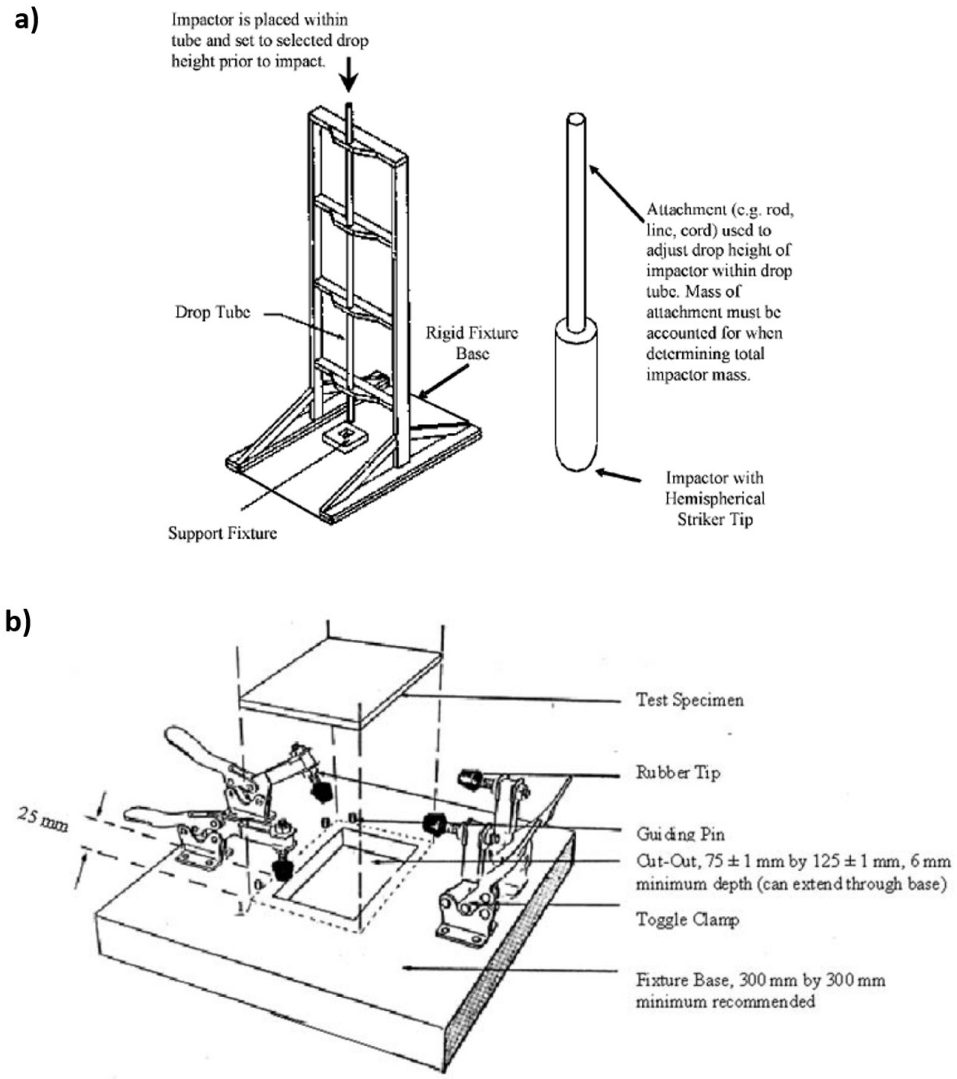

Figure 3.21: Drop-weight Low velocity impact machine (a), scheme of the clamping system (b), from ASTM D7136.

After the impact, the damage to the specimen is analyzed, focusing on failure modes such as core crushing, face sheet delamination, and core-face debonding. The extent of damage provides valuable insights into the ability of the sandwich structure to absorb energy and resist failure during impact events. To study the impact behavior of 3D printed sandwich structures, the ASTM D7136 standard was followed and the Instron Ceast 9350 machine was used.

Figure 3.22: Instron Ceast 9350 drop-weight impact machine. [169]

This test is particularly important in safety-critical applications where the structural integrity of a component must be maintained after an impact, ensuring the continued performance of the structure in service.

3.4.9 Compression after Impact Test

The Compression After Impact (CAI) test is a critical method used to evaluate the residual compressive strength of composite materials and structures after they have been subjected to an impact event. This test is particularly important in industries such as aerospace, automotive, and defense, where materials are often exposed to impacts during service, and their ability to withstand compressive loads after damage can be crucial to structural integrity. Composite materials, while strong and lightweight, can suffer internal damage - such as delamination or matrix cracking - after an impact, which may not be immediately visible but can significantly degrade their mechanical properties. The CAI test provides a quantitative measure of how much compressive strength is retained after impact damage has occurred.

To perform the CAI test, a panel or laminate is first subjected to a controlled impact using methods like the low-velocity impact test or drop-weight test. The impact creates localized damage, typically in the form of a dent, delamination, or fiber breakage, without completely penetrating the specimen. After the impact, the panel is carefully inspected,

often using non-destructive techniques such as ultrasonic C-scanning, to assess the extent of internal damage. Once the damage is characterized, the specimen is prepared for compression testing.

The impacted specimen is placed into a specially designed fixture that supports the panel along its edges to prevent buckling during the test. The compressive load is gradually increased until the panel fails, with the maximum compressive load sustained before failure being recorded as the residual compressive strength. The failure mode is also observed, which can include delamination propagation, fiber buckling, or matrix cracking, depending on the material system and the extent of the impact damage. The ASTM D7137 is the standard followed in this study using a MTS Insight machine for testing 3D printed sandwich panels.

Figure 3.23: Tool used for CAI test. [170]

The CAI test is essential for understanding the durability and safety of composite structures in service, particularly in applications where unexpected impacts may occur, such as aircraft fuselages, automotive body panels, or sporting goods. By comparing the residual compressive strength to the original (undamaged) strength, it is possible to quantify the impact tolerance and optimize designs for improved damage resistance and post-impact performance. This test is also useful to validate material models and predict the behavior of composites under combined impact and compressive loading conditions.

3.4.10 Damage Indentation

The measurement of damage indentation using a comparator is a non-destructive inspection technique widely employed to assess the surface-level damage in materials, particularly composites, after impact events. This method is often used in quality control and post-impact evaluations to determine the severity of a visible dent or deformation caused by an impact. Accurate measurement of these indentations is critical for assessing the need for repairs or further inspection.

The process involves the use of a mechanical depth comparator, which is a precision instrument designed to measure the depth of surface deformations. A typical comparator consists of a base plate and a dial gauge or digital indicator with a probe. To begin the measurement, the comparator is positioned on the surface of the impacted specimen, ensuring that the base plate is level and rests on the undamaged area around the indentation. The probe is then carefully lowered into the center of the damaged area, and the depth of the indentation is recorded. This process is often repeated at multiple points within and around the damaged region to obtain a clear profile of the indentation and ensure that the deepest point is accurately captured. For this scope, a Mitutoyo Absolute comparator was used.

Figure 3.24: Mitutoyo Absolute comparator.

The depth and size of the indentation provide important initial information about the extent of damage to the material. While small indentations might not indicate significant internal damage, larger or deeper indentations often correlate with more severe damage such as delamination or matrix cracking in composite materials. This data is used to determine if further non-destructive testing, such as ultrasound inspection, is necessary

to evaluate the internal damage more thoroughly. In practice, the comparator method is a quick and reliable way to quantify surface damage, helping maintenance teams decide on the next steps in the inspection or repair process.

3.4.11 Ultrasound inspection

Ultrasound inspection is a non-destructive testing (NDT) technique used to detect internal damage within materials that may not be visible on the surface. This method is particularly valuable for identifying subsurface defects such as delamination in composites, voids, cracks, and inclusions which can occur during the manufacturing process or after a damage event. Ultrasound inspection is a preferred technique in industries such as aerospace and automotive because it provides detailed insight into material internal condition without causing further damage to the specimen.

The process of ultrasound inspection begins by applying a coupling medium, typically a gel or liquid, to the surface of the specimen. This coupling medium ensures efficient transmission of the ultrasonic waves from the transducer into the material. A handheld or automated ultrasound transducer, which emits high-frequency sound waves, is then placed on the surface of the specimen. The transducer sends these sound waves through the material, and when the waves encounter a boundary, such as a void or defect, they are reflected to the transducer. The time it takes for the sound waves to return is measured and used to determine the location and size of internal defects.

In ultrasound inspection, several configurations can be used depending on the type of material and the nature of the defects being investigated. The most common configurations are transmission, reflection (pulse-echo), and through-transmission modes. Each configuration has its advantages and is chosen based on the specific inspection requirements, material type, and the nature of the expected defects.

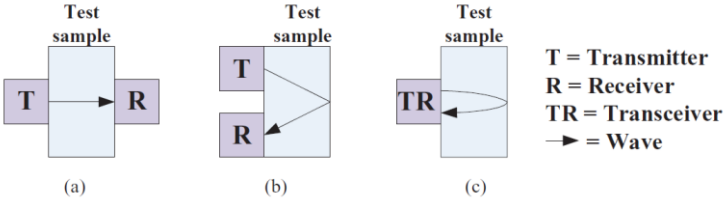

Figure 3.25: Ultrasonic sensing mode (a) transmission; (b) pitch catch; (c) pulse-echo. [171]

Through-transmission mode, on the other hand, involves two separate transducers placed on opposite sides of the specimen. One transducer emits the ultrasonic waves, and the other receives the waves that pass through the material. This configuration is highly sensitive to defects that block or disrupt the sound waves, such as large voids or inclusions, but it requires access to both sides of the material, which may not always be feasible.

In *pulse-echo* mode, the transducer acts as both the transmitter and receiver of the ultrasonic waves. The sound waves are sent into the material, and the same transducer detects the reflected waves when they encounter internal features. This method is widely used for detecting internal defects from a single side of the specimen and is effective for locating flaws such as cracks and delamination.

Another configuration is *pitch-catch* mode, where two transducers are positioned on the same side of the specimen. One transducer emits the ultrasound waves, while the other receives the waves after they have interacted with internal features. This method can be advantageous for detecting defects near the surface or in cases where reflection from internal boundaries is weak.

The data collected during the ultrasound inspection is visualized in the form of A-scans, B-scans, or C-scans, depending on the level of detail required. A-scans provide a one-dimensional representation of the wave reflections, B-scans give a cross-sectional view of the material, and C-scans offer a two-dimensional image showing the distribution of defects within the specimen. This information allows inspectors to precisely locate and quantify internal damage, such as the extent of delamination or voids beneath the surface, which are not detectable through visual inspection alone. For the present research, the ultrasounds inspection was performed in transmission configuration (TTU).

4 Influence of process parameters on physical and mechanical features of PEEK printed parts

The process of Fused Filament Fabrication (FFF) with polyether(etherketone) (PEEK) presents significant challenges due to its high melting point and viscosity, which require elevated printing temperatures and careful optimization of various parameters. In this chapter, the effects of printing speed, nozzle temperature, and chamber temperature on the crystallinity and tensile properties of the material are analyzed. The findings demonstrated that it is possible to control the structural properties of 3D printed PEEK, which are closely linked to its tensile performance. Notably, the chamber temperature had the greatest impact on the degree of crystallinity, which directly influences the material tensile behavior. As the crystallinity increases, the material becomes stiffer. Additionally, both printing speed and nozzle temperature play critical roles in minimizing voids within the printed parts, thereby enhancing tensile strength.

4.1 Design of Experiment

The Roboze PEEK filament was used as the feed material for the Roboze Argo 500 3D printer. This filament has a standard diameter of 1,75 mm, a glass transition temperature (Tg) of 143°C, a melting temperature (Tm) of 343°C, and a density of 1,30 g/cm^3. The Roboze Argo 500 printer offers several advanced features, well described in Chapter 3, paragraph 3.2.

To investigate how certain process parameters could enhance mechanical properties and minimize voids in printed parts, the following variables were selected for examination:

- **Nozzle Temperature:** Three different nozzle temperatures - 440°C, 450°C, and 460°-were tested. These temperatures were chosen because the filament supplier recommends extrusion temperatures around 100°C higher than the filament's melting temperature.

- **Chamber Temperature:** Three chamber temperatures - 100°C, 130°C, and 160°C- were explored to assess the performance both below and above the glass transition temperature.

- **Printing Speed (Sp):** Four printing speeds - 1200 mm/min, 1500 mm/min, 2000 mm/min, and 2600 mm/min - were selected. The first two slower speeds were aimed at reducing defects, while the faster speeds were considered to optimize production time, particularly for industrial applications.

Additional Test Condition: to further evaluate the quality of the extruded material under more energetically convenient conditions, printing was also tested with the chamber at ambient temperature (25°C) and the nozzle at 450°C.

Other process parameters used for printing all samples are listed in Table 4.1. It must be noted that the print direction (raster angle) was chosen of 0° with respect to the loading direction, according to Rahman and Arif results. [64] [65]

Process Parameters	
Nozzle diameter	0,4mm
Raster angle	0°
Bottom layers	4
Bottom layer orientations	-45°/+45°
Walls number	2
Layer thickness	0,225mm
Infill density	100%
Infill pattern	Lines

Table 4.1: Process parameters used to 3D print all samples.

These experiments were designed to determine the optimal combination of conditions to improve the crystallinity, mechanical properties, and overall quality of FFF printed PEEK parts. A summary of the experimental design is provided in Table 4.2, where Tn, Sp, and Tch represent nozzle temperature, printing speed, and chamber temperature, respectively, along with the nominal number of samples printed for each condition (N). The sample dimensions for the tensile test are 4.05 mm x 25.4 mm x 254 mm. The final g-code for the printing process was generated using Simplify 3D software. The ASTM D3039 standard was chosen for the tensile test due to its relevance, as it mirrors the layer-by-layer deposition method used in standard laminates. Additionally, the extruded filaments in 3D printing behave similarly to unidirectional fibers in a composite when subjected to tensile stress.

Tn (°C)	Sp (mm/min)	Tch (°C)	N
440	1200	100	4
		130	4
		160	4
	1500	100	4
		130	4
		160	4
	2000	100	4
		130	4
		160	4
	2600	100	4
		130	4
		160	4
450	1200	100	4
		130	4
		160	4
	1500	25	4
		100	4
		130	4
		160	4
	2000	25	4
		100	4
		130	4
		160	4
	2600	25	4
		100	4
		130	4
		160	4
440	1200	100	4
		130	4
		160	4
	1500	100	4
		130	4
		160	4
	2000	100	4
		130	4
		160	4
	2600	100	4
		130	4
		160	4

Table 4.2: Test matrix.

In addition to tensile test samples, smaller specimens were printed for analysis using Differential Scanning Calorimetry (DSC). Once printing was complete, all specimens were removed from the build plate, and the supports were machined off using CNC equipment. To prepare the samples for mechanical testing, aluminum alloy (EN AW 6082) tabs were bonded to the specimens using a two-component epoxy adhesive

(Araldite 2031-1, Huntsman). Figure 4.1 (c) presents an image of a typical specimen, fully prepared and ready for tensile testing.

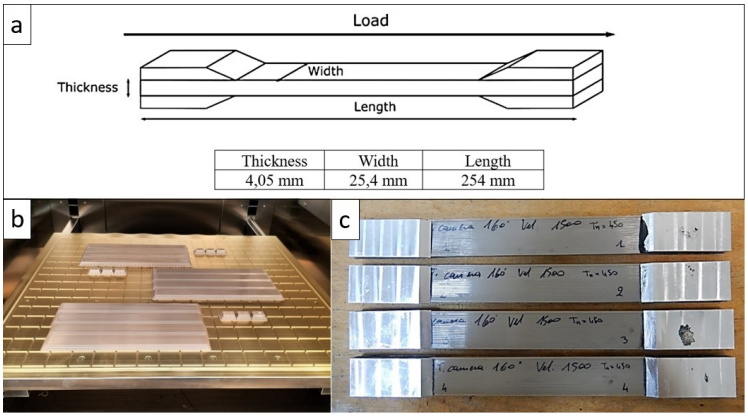

Figure 4.1: Scheme of the specimen for ASTM D3039 tensile test (a), 3D printed specimens for tensile test as built (b) and after machining and tabs attachment (c). [172]

All mechanical tests were conducted using an MTS machine (model 370.25 Landmark Load Frame) equipped with a 250 kN load cell. The Young's Modulus (E) for each test was measured using an extensometer. The tensile tests were performed at room temperature with a constant rate of 2 mm/min. Mechanical performance was assessed and compared based on Tensile Strength (MPa) and Young's Modulus (MPa). Tensile Strength was calculated as the ratio of the maximum load to the specimen's cross-sectional area, while Young's Modulus was determined from the slope of the linear portion of the stress-strain curve obtained from extensometer data.

To examine the internal structure of the specimens, cross-sectional images were captured using an Optical Microscope (OM). The samples were cut perpendicular to the filament deposition direction with a miter saw using a cooling medium and then mechanically polished. The polished surfaces were analyzed with a Hirox RH – 2000 digital Optical Microscope.

The thermal properties and degree of crystallinity (χ) of the material were evaluated for all samples as well as for the virgin PEEK filament using Differential Scanning Calorimetry (DSC) with a DSC 250 machine from TA instruments. The DSC tests were conducted from 50°C to 400°C with a heating rate of 10°C/min, under a nitrogen flow of 50 ml/min.

4.2 Results and Discussion

4.2.1 Thermal Characterization

The thermal properties of both PEEK filament and printed specimens were assessed through Differential Scanning Calorimetry (DSC) to examine how the printing process affects the material. Initially, DSC analysis was performed on the unprocessed filament to establish a baseline for comparison. This allowed us to compare the characteristic temperatures and degree of crystallinity with those of the specimens after printing. The results for the raw filament are detailed in Table 4.3, where Tg, Tm, Tc, and χ represent the glass transition temperature, melting temperature, crystallization temperature, and degree of crystallinity, respectively.

Tg (°C)	Tm (°C)	Tc (°C)	χ (%)	χ std.dev. (%)
149	332	289	27,6	1,6

Table 4.3: Crystallinity degree and transition temperatures of raw PEEK filament from DSC scans.

DSC analyses were performed on all samples according to the test matrix outlined in Table 4.2. The impact of chamber temperature on the crystallinity of PEEK was first examined with the nozzle temperature held constant at 450°C. The four chamber temperatures chosen for this analysis were: room temperature (25°C), achieved without heating the chamber; two temperatures below the glass transition temperature (Tg ≈ 145°C) of 100°C and 130°C; and the highest available temperature of 160°C, which is above the PEEK Tg.

The most challenging condition was at a chamber temperature of 25°C, due to the significant temperature gradient between the chamber and the nozzle. This resulted in rapid cooling of the extruded filament, increasing the risk of nozzle clogging and process failure. [173] [174] Despite using a nozzle temperature of 450°C and printing speeds above 1200 mm/min to mitigate clogging risks, prints at 25°C were not successful. The residual stresses within the samples prevented proper adhesion to the printing bed, often resulting in warped or distorted parts (see Figure 4.2). Consequently, for the nozzle temperatures of 440°C and 460°C, only the other three chamber temperatures -100°C, 130°C, and 160°C-were analyzed, as indicated in Table 4.2.

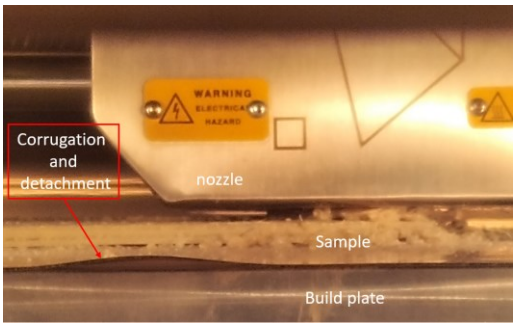

Figure 4.2: Interruption of the printing process due to corrugation and detachment of the specimen from the build plate.

Figure 4.3 displays the DSC scans for samples printed with a nozzle temperature of 450°C and a printing speed of 2000 mm/min, highlighting the thermal transitions of the material as the chamber temperature varies. The graph shows a significant point at 143°C, which corresponds to the glass transition temperature (Tg) of the material. An endothermic peak around 330°C is associated with the melting temperature (Tm) of the material. Additionally, samples printed at chamber temperatures of 25°C, 100°C, and 130°C exhibit an extra exothermic peak around 170°C, indicating cold crystallization. This occurs because the heat during the DSC test enhances polymer chain mobility, leading to the formation of additional crystalline domains in samples with amorphous regions that are capable of crystallizing. The initial crystallinity of these samples was calculated from the melting and cold crystallization enthalpies (Eq. *5*), and the results are detailed in Table 4.4. Key observations from these results, including the main effect and interaction plots shown in Figure 4.4, are as follows:

- *Influence of Printing Speed*: Increasing the printing speed to Sp > 1500 mm/min results in decreased crystallinity. This is because faster extrusion cools the material more quickly, leaving less time for polymer chains to organize into crystalline domains. The effect on crystallinity is less pronounced at a nozzle temperature of 460°C.

- *Influence of Chamber Temperature*: Generally, a higher chamber temperature leads to increased crystallinity. This occurs because a warmer chamber reduces the temperature difference between the extruded material and the environment, allowing the polymer chains to cool more slowly and form more crystalline domains. Interaction plots (Figure 4.4 a) show that at a chamber temperature of

130°C, the impact of printing speed on crystallinity is reduced, while at 160°C, the effect of nozzle temperature is significantly diminished.

- *Influence of Nozzle Temperature*: Evaluations were made at three chamber temperatures: 100°C, 130°C, and 160°C. Typically, a larger temperature difference between the chamber and the nozzle results in lower crystallinity due to faster cooling rates of the extruded filament. Increasing the nozzle temperature from 440°C to 450°C generally leads to decreased crystallinity, but a further increase to 460°C results in a slight increase in crystallinity. This effect is less noticeable at higher chamber temperatures (see Figure 4.4 a) due to the smaller temperature difference. At a nozzle temperature of 450°C, chamber temperature has a more significant impact on crystallinity.

From the main effect plot (Figure 4.4 b), it is evident that printing speed and chamber temperature are the most influential factors on crystallinity. Higher chamber temperatures significantly increase the degree of crystallinity, aligning with Yang et al.'s findings on isothermal crystallization, where the ambient temperature closely matches the PEEK crystallization temperature (Tc ≈ 290°C) [15]. In this process, polymer chains in an amorphous state gain sufficient energy and time to crystallize close to the typical PEEK crystallinity of 35%. By reducing the printing speed to 1200-1500 mm/min and maintaining the chamber at its maximum temperature of 160°C, a crystallinity degree higher than 30% was achieved (Table 4.4).

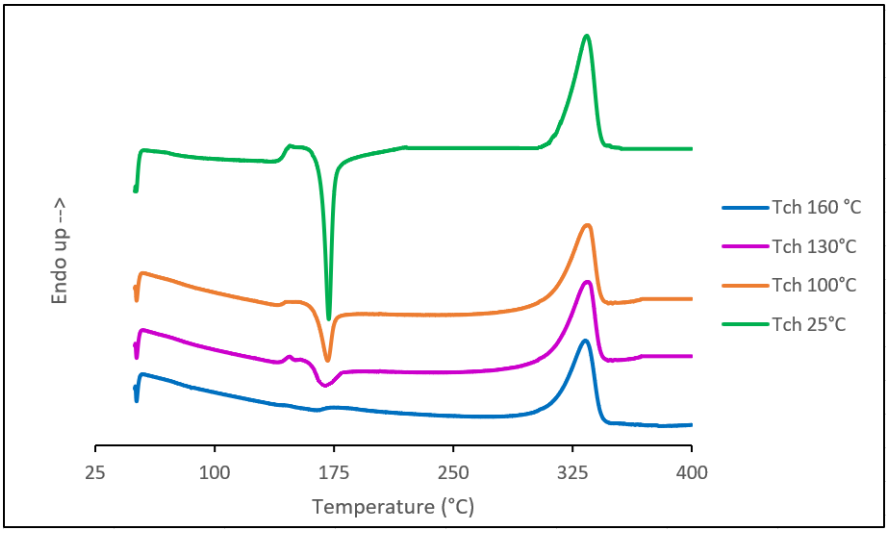

Figure 4.3: DSC scans at different chamber temperatures of samples printed with Tn=450°C and Sp=2000mm/min.

Tch (°C)	Tn (°C)	χ (%) at 1200 mm/min	St.Dev. (%)	χ (%) at 1500 mm/min	St.Dev. (%)	χ (%) at 2000 mm/min	St.Dev. (%)	χ (%) at 2600 mm/min	St.Dev. (%)
25	450	-	-	17,0	1,7	15,0	2,2	13,6	2,8
100	440	31,7	4,5	28,4	2,5	27,7	1,2	22,3	1,3
	450	26,9	2,1	25,0	1,7	23,9	0,4	20,1	0,8
	460	27,5	2,4	27,9	1,3	26,1	1,3	26,1	2,2
130	440	30,0	4,7	29,6	0,4	30,9	3,4	30,4	1,1
	450	28,0	2,3	27,7	4,1	27,0	3,0	25,9	2,0
	460	30,9	4,4	27,3	2,2	26,7	3,7	25,7	1,1
160	440	33,1	0,8	30,8	0,4	29,4	0,3	28,3	0,5
	450	32,7	1,8	33,3	1,1	29,8	1,6	27,7	2,8
	460	30,8	1,2	30,4	3,1	29,9	3,6	28,2	2,0

Table 4.4: Degree of crystallinity of printed PEEK samples calculated from DSC heating scan.

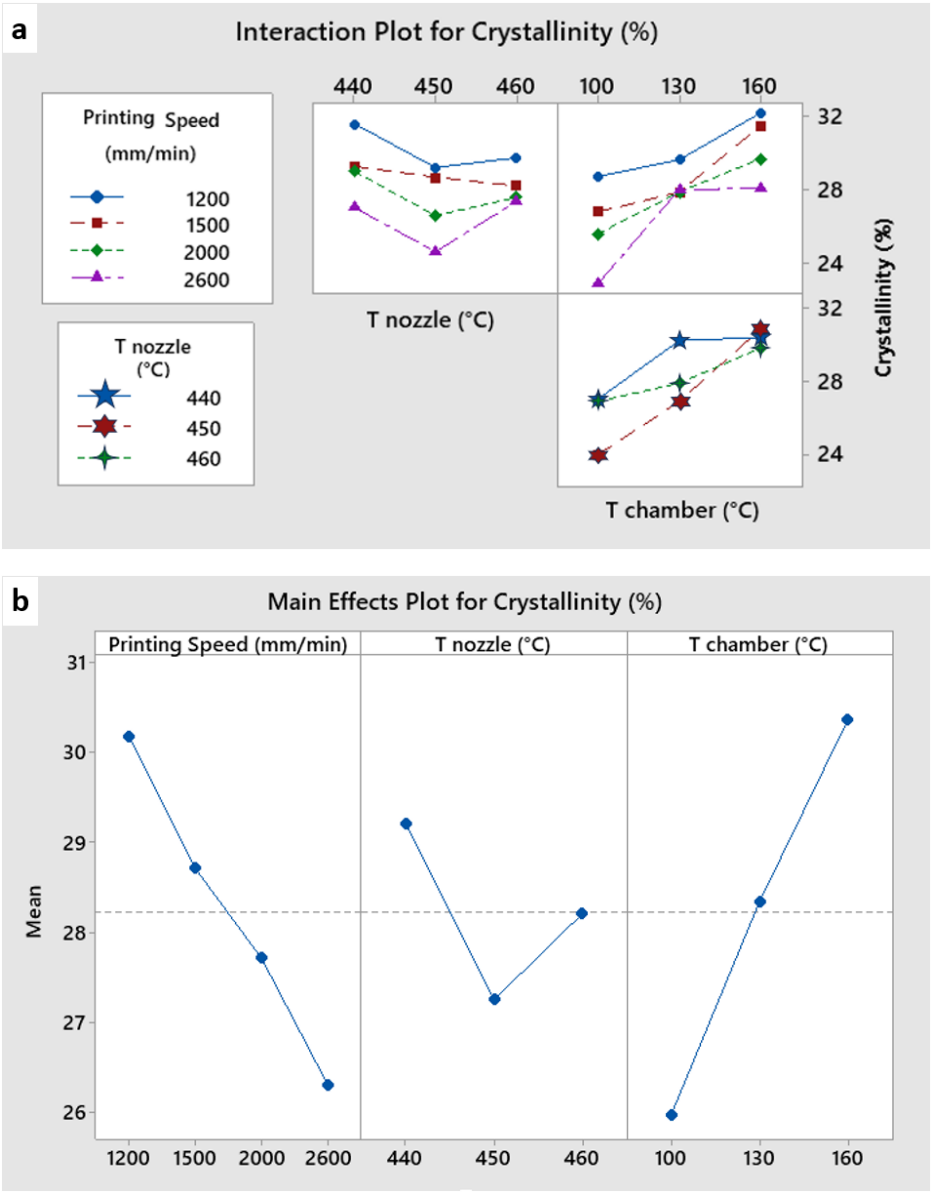

Figure 4.4: Interaction plot (a) and Main effect plot for degree of crystallinity (b).

Figure 4.5 compares three samples with varying degrees of crystallinity, clearly demonstrating that the color of each sample is closely related to its crystalline domain percentage. By observing the sample colors, it could be possible to make an approximate estimation of their crystallinity: as the degree of crystallinity increases from $\chi < 20\%$ to $\chi > 25\%$, the samples exhibit a transition in color from translucent dark brown to opaque light grey. The translucent or semi-transparent effect is typical of amorphous polymers, while semi-crystalline polymers are opaque, in fact the presence of crystallites, having a different refractive index from the amorphous phase, allows the refraction of light radiation in different wavelengths at the interfaces between the two phases. The greater

the presence of crystallites in the polymer, the greater the refraction of light and the opacity of the polymer which will appear white in color.

Figure 4.5: Colour comparison between three samples with different degrees of crystallinity. [172]

4.2.2 Optical Microscopy (OM) and mechanical characterization

For the optical microscope analysis, a sacrificial sample from the smallest printed specimens (used for DSC analysis) was sectioned and examined. These observations revealed that printing speed significantly affects both inter- and intra-layer adhesion. As shown in the OM images in Figure 4.6, reducing the printing speed results in a decrease in the presence and average size of voids within the samples. At a printing speed of 1200 mm/min, voids nearly disappear, consistent with findings from Wang's study [16]. Additionally, increasing the nozzle temperature enhances filament adhesion. The images indicate that, across all printing speeds, a nozzle temperature of 450°C produced better welding and fewer pores compared to the other nozzle temperatures. This improvement is attributed to the higher temperature of the extruded material, which facilitates better bonding between filaments [17]. However, the impact of nozzle temperature on adhesion is less pronounced than the effect of printing speed.

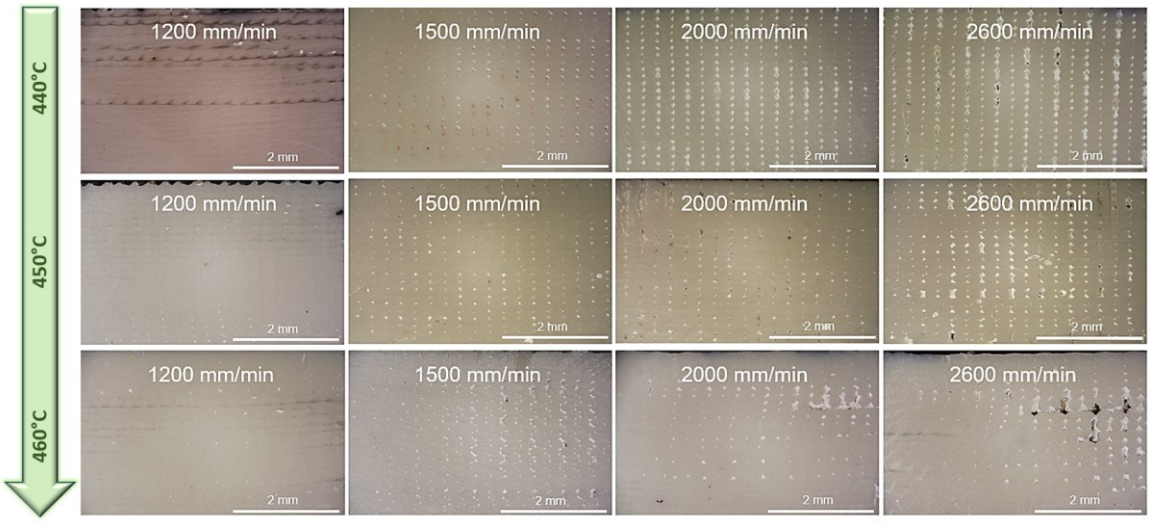

Figure 4.6: Cross sections of samples printed at Tch of 160°C and Tn of 440°C, 450°C and 460°C.

The tensile test results, including Tensile Strength at maximum load, Ultimate Strength at break, and Young's Modulus, are summarized in Table 4.5. Notably, some samples were too ductile to evaluate Ultimate Strength, as they stretched without breaking. Figure 4.7 displays the main effect and interaction plots related to Tensile Strength and Young's Modulus.

Tn (°C)	Tch (°C)	Sp (mm/min)	Tensile Strength at maximum load (Mpa)	TS St.Dev. (%)	Ultimate Strength at break (MPa)	US St.Dev. (%)	Young Modulus (E) (MPa)	E St.Dev. (%)
440	100	1200	73,0	1,2	48,6		2723,1	3,5
		1500	59,6	1,8	-	-	2440,2	1,8
		2000	59,6	0,6	-	-	2413,3	1,4
		2600	56,6	2,3	-	-	2273,5	2,4
	130	1200	86,8	0,5	66,8	2,5	3347,0	0,8
		1500	86,8	1,5	68,6	3,2	3432,5	0,9
		2000	89,3	0,9	70,9	1,9	3392,8	2,8
		2600	86,8	1,0	-	-	3339,3	0,7
	160	1200	86,8	3,0	77,5	4,9	3360,7	4,5
		1500	80,9	0,9	64,3	2,2	3013,0	2,1
		2000	79,9	1,5	62,3	1,1	2948,0	2,9
		2600	76,8	0,7	58,5	3,0	2870,3	2,1
450	100	1200	73,5	2,9	-	-	2462,9	0,8
		1500	61,6	0,3	-	-	2510,2	0,2
		2000	60,6	1,1	-	-	2494,1	3,8
		2600	58,3	1,0	-	-	2412,7	2,7
	130	1200	78,6	0,8	60,3	2,5	2941,1	1,5
		1500	77,5	0,5	60,4	1,8	2871,9	2,5
		2000	76,4	3,6	61,3	1,2	3014,5	1,1
		2600	74,9	1,0	60,6	1,9	2864,9	0,6
	160	1200	85,8	1,1	-	-	3331,8	1,6
		1500	83,3	0,9	66,9	2,7	3178,4	0,8
		2000	83,2	1,6	66,8	2.2	3068,6	3,6
		2600	79,7	1,3	65,9	1,1	3050,9	1,1
460	100	1200	75,7	3,4	-	-	2986,9	4,9
		1500	72,3	2,7	-	-	3026,7	1,1
		2000	72,9	1,8	-	-	3004,2	1,8
		2600	73,6	0,9	70,3	1,2	3087,4	3,8
	130	1200	88,1	0,6	69,9	3,0	3570,6	2,8
		1500	82,4	1,1	66,7	3,5	3518,6	5,1
		2000	84,4	2,1	67,1	3,8	3488,1	1,9
		2600	76,0	4,5	72,51	4,4	3399,5	2,7
	160	1200	87,2	0,7	75,4	4,7	3589,5	4,6
		1500	87,6	0,5	76,3	3,5	3539,6	3,5
		2000	87,6	0,7	85,1	2,7	3957,3	4,5
		2600	79,6	3,5	78,7	2,2	3535,8	4,9

Table 4.5: Tensile test results.

Key observations from the data are as follows:

- *Influence of Printing Speed:* The results for Tensile Strength and Young's Modulus are similar for printing speeds of 1500 mm/min and 2000 mm/min on average. However, they decrease at 2600 mm/min and slightly increase at 1200 mm/min. As indicated in Figure 4.6, at 2600 mm/min, there are more and larger pores, and the effective cross-sectional area is reduced, leading to lower maximum load capacity. Higher printing speeds also correlate with lower crystallinity, resulting in poorer mechanical performance [60] [62].

- *Influence of Chamber Temperature*: For samples printed at a chamber temperature of 100°C, the crystallinity level is typically below 28% (Table 4.4), and the specimens tend to be ductile, stretching significantly. Only the Tensile Strength at maximum load could be compared for these specimens, as they did not break but reached the displacement limit of the grips. Comparing Tensile Strength at maximum load for samples printed at 100°C, 130°C, and 160°C reveals that higher chamber temperatures improve mechanical performance due to increased crystallinity [60] [61]. Chamber temperature is the most influential factor in the results.

- *Influence of Nozzle Temperature:* Consistent with observations by El Magri et al. [158], increasing the nozzle temperature generally improves results. At 460°C, the reduction in pore size is more pronounced than the effect on crystallinity, due to decreased melt viscosity and improved specimen density [63].

In general all the variables that lead to an increase in the number of pores consequently lead to a reduction in mechanical properties. However, with the 0° printing strategy that we used this effect is more attenuated, because the pores do not act as a weakening between the layers in the direction perpendicular to the load application. For 90° specimens the influence of the pores would be much more evident because air channels are created between the filaments perpendicular to the load.

For the 0° specimens, the deposited filaments continue to support the load, but the more pores there are, the more they work separately. Based on the application of the final 3D printed part, process parameters can be selected to achieve optimal structural characteristics in terms of filament adhesion and mechanical performance related to

crystallinity. Tensile Strengths (TS) exceeding 80 MPa are associated with samples having a crystallinity degree greater than 29%. The following conditions yielded TS > 80 MPa:

- When the nozzle temperature (Tn) was 460°C, with chamber temperatures (Tch) of 130°C and 160°C, and printing speeds (Sp) below 2600 mm/min.
- When Tn was 450°C, with Tch at 160°C and Sp below 2600 mm/min.
- When Tn was 440°C, with Tch at 130°C across all tested speeds, and at 160°C with Sp below 2000 mm/min.

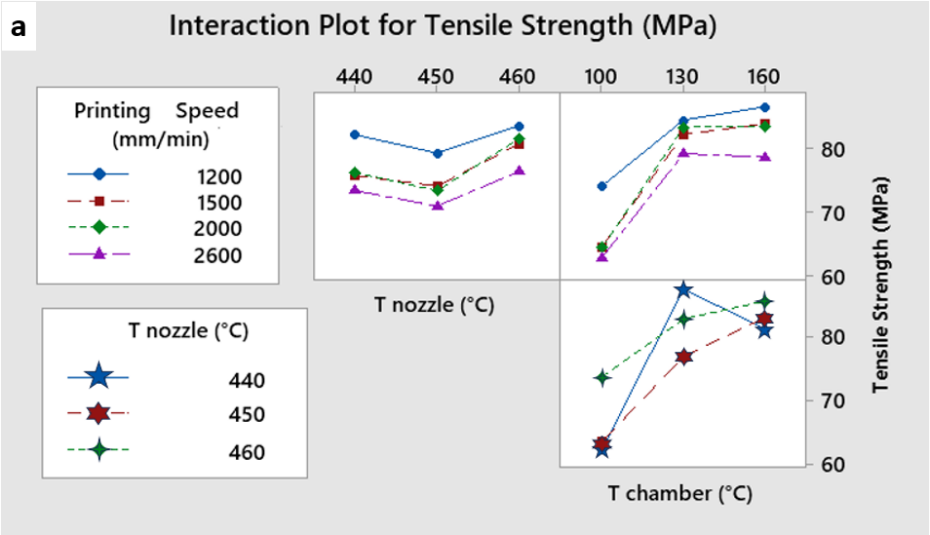

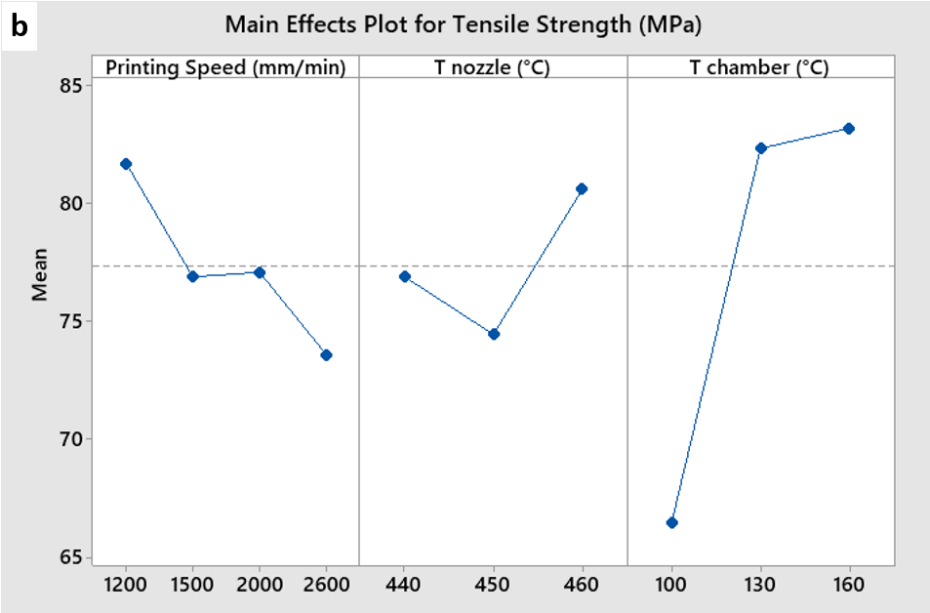

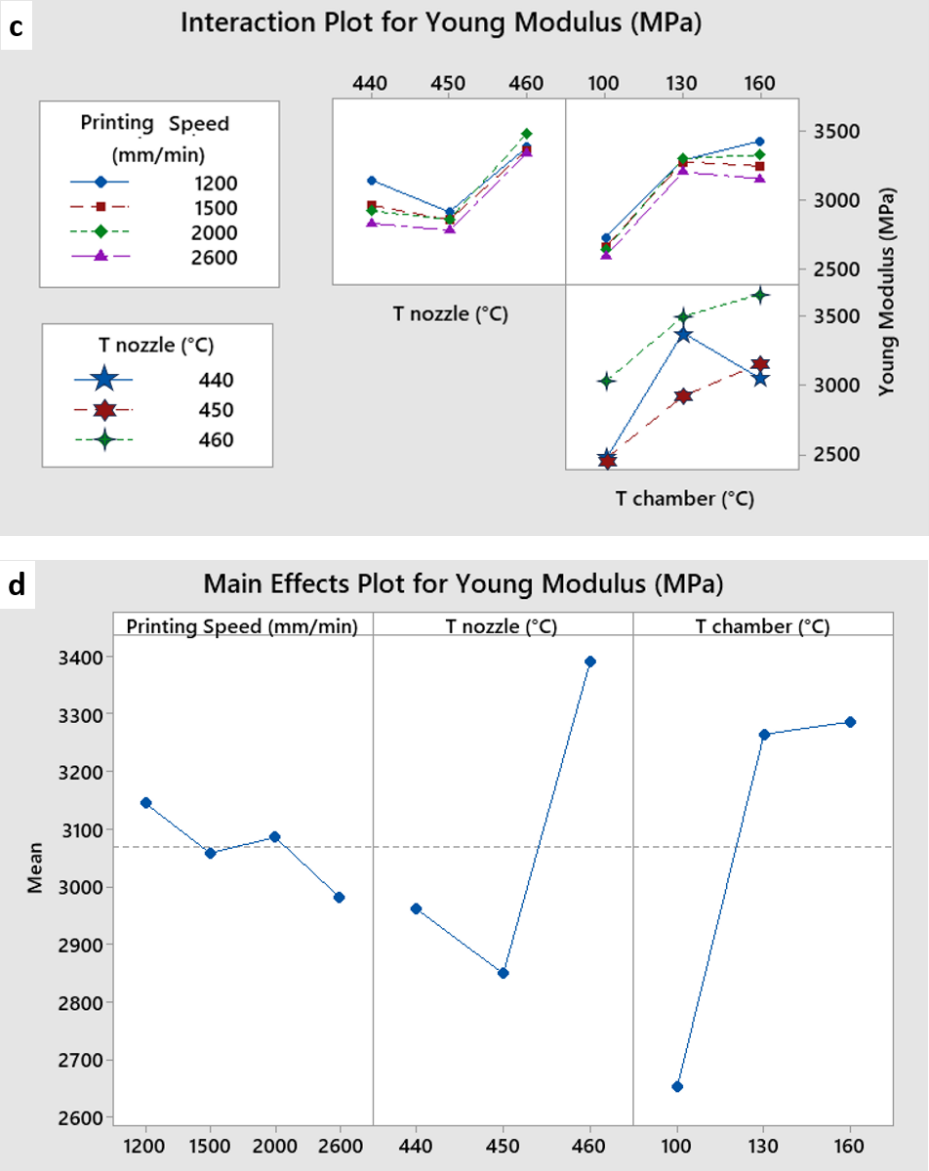

Figure 4.7: Interaction plot (a) and Main effect plot (b) for Tensile strength; Interaction plot (c) and Main effect plot (d) for Young's Modulus.

Figure 4.8 (a-c) presents the stress-strain curves for all samples printed at different chamber temperatures, with each plot including a photo of a representative tested sample. These graphs clearly illustrate that process temperatures have a more significant impact on overall tensile behavior than printing speed. This reinforces the important role of material crystallinity in defining the mechanical properties of the printed parts. Specifically, when the crystallinity (χ) is below 27%, the material becomes more ductile. The samples exhibiting ductile behavior were either light or dark brown, as indicated in Figure 4.5, where the crystallinity was less than 25%.

The stress-strain curves generally exhibit the typical pattern of a semicrystalline thermoplastic material. Initially, the material undergoes linear elastic deformation, followed by nonlinear elastic deformation. As elongation occurs along the entire length of the sample, a uniform reduction in cross-sectional area (hardening) is observed. The material becomes more resistant, and the stress required to continue deforming the specimen increases until reaching the maximum value, known as tensile strength (TS). At this point, necking begins, where elongation becomes localized in a specific area (the neck), leading to a reduction in the cross-sectional area. Beyond this maximum point, stress decreases because the reduced cross-sectional area requires less force to maintain a given deformation rate. Despite this, stress calculations continue using the initial cross-sectional area, explaining why specimens might fracture under a stress lower than the TS and why they may exhibit varying deformations under the same load.

Following the zone of decreasing stress, two scenarios can emerge:

- If the material is ductile, necking will extend throughout the specimen without resulting in fracture. In such cases, the stress-strain curve will show a horizontal line, indicating plastic deformation. In this stage, the polymer chains orient and move relative to each other in the direction of the applied force.

- If the material has lower ductility due to higher crystallinity, a crack will form within the neck region. This crack will propagate rapidly, leading to specimen failure. For these specimens, it is possible to measure the Ultimate Strength.

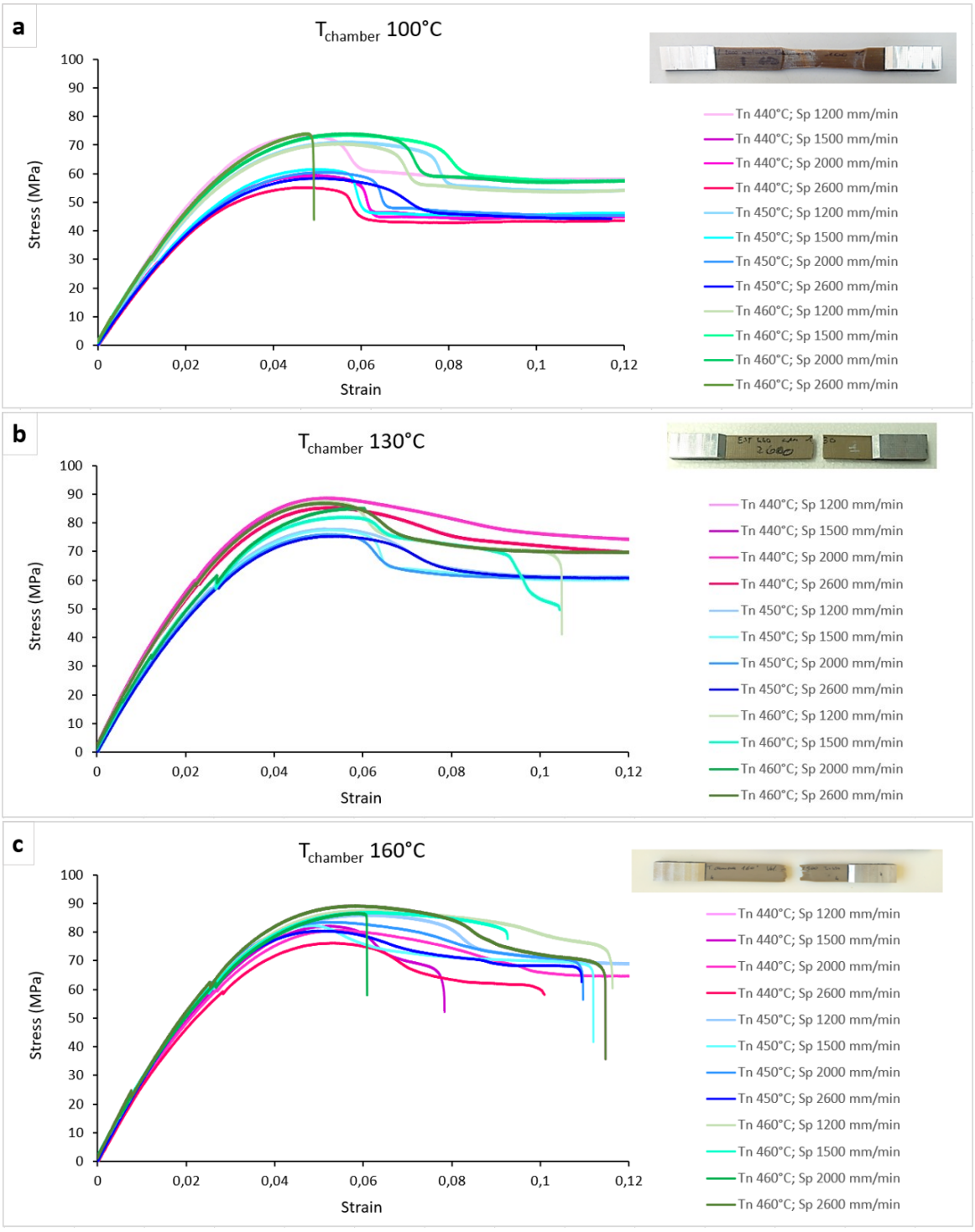

Figure 4.8: Stress-strain curves of all samples printed at Tch of 100 °C (a), 130 °C (b) and 160 °C (c). [172]

In this first part of the research, the effects of printing parameters (nozzle and chamber temperatures and printing speed) on 3D printed PEEK mechanical performances and crystalline characteristics were studied. It was found that the chamber temperature and the printing speed are the most influent parameters for the crystallinity degree, instead the chamber and nozzle temperatures are the parameters that can determine the mechanical behaviour. Adjusting the temperature of the chamber and nozzle allows for the creation of a material with either greater flexibility or increased rigidity, depending on its intended use. Furthermore, the printing speed determines the inter- and intra-layers adhesion, i.e. the presence and dimensions of voids within the printed component. Preventing voids is essential in industries like aerospace and aviation, particularly for structural applications. In the present study, the best tensile performances in terms of tensile strength (of about 89,3 MPa) with a Young's modulus of 3392,8 MPa and a degree of crystallinity of 30,9% were obtained by printing at a nozzle temperature of 440 °C, chamber temperature of 130 °C and with a printing speed of 2000 mm/min. However, very similar results, with tensile strength higher than 87 MPa and Young's modulus higher than 3500 MPa were also obtained for a nozzle temperature of 460°C, chamber temperature of 130°C and printing speed of 1200 mm/min, and chamber temperature of 160°C and printing speeds of 1200, 1500, 2000 mm/min.

The results of this study allowed to understand better the PEEK structural features linked to the thermal processing of the material and how these properties can affect the mechanical behaviour. These results were very important for the following part of the research.

5 Improvement of interlayer adhesion in 3D printed PEEK and PC parts

The aim of this study is to evaluate the effect of atmospheric plasma treatment on the interlayer adhesion in 3D printed Polyether(etherketone) (PEEK) and Polycarbonate (PC) samples. In particular, it was used the handheld piezoelectric plasma torch PiezoBrush PZ3 from Reylon plasma. [153] In order to choose the best treatment conditions in terms of plasma exposure time and distance of the torch from the surface (named "working distance"), different combinations of these two factors were tested and the evaluation of the change in surface energy and wettability was performed by sessile water contact angle (WCA) measurements. For each condition, the superficial temperature of the sample was measured by means of a thermal camera to quantify the surface heating due to the treatment. The treated surfaces were than characterized both morphologically by Scanning Electron Microscopy (SEM) and chemically by FT-IR spectroscopy (in ATR mode).

Finally, chosen the conditions that allow the highest wettability (lowest contact angle values), it was possible to simply mount the plasma torch on the Ultimaker S5 printer using a custom-made setup, and verify the actual improvement of the interlayer adhesion by testing treated and untreated samples through single lap shear mechanical test. This test allows to obtain actual results by treating only few successive layers in the overlap area of the two half-parts constituting the specimen. In this way, after comparing the results obtained for the characterization of both PEEK and PC polymers, and evaluating the actual effectiveness of the treatment on the interlayer adhesion through mechanical testing on the PC, it would be possible to indirectly draw predictions on the mechanical behavior that PEEK would have when it is plasma treated.

5.1 Design of Experiment

5.1.1 Materials and FFF parameters

The materials chosen for this study are two technopolymers: Polycarbonate PC-S 3D filament purchased from Kimya and Polyether(ether ketone) filament from Roboze. These two materials are very interesting for advanced applications in functional parts thanks to their high mechanical performances, thermal resistance, flame retardancy

ability, high glass transition temperature and melting point. Furthermore, they present similarities both in the molecular structure made up of aromatic rings and carbon-oxygen bonds, and in the surface energy of approximately 42 dyne/cm for PC [175] and 44 dyne/cm for PEEK [176].

To 3D print samples with these two materials, two different 3D printers were used: the Roboze One+400 for PEEK and Ultimaker S5 and for PC. Samples used for WCA, SEM and ATR-FTIR analyses were 3D printed with the dimensions reported in Figure 5.1 a and with the process parameters reported in Table 5.1. The process parameters, i.e. printing speed 20 mm/s, nozzle temperature 450°C and layer thickness 0,2 for printing PEEK samples were chosen on the basis of the best results obtained from the study described in Chapter 4.

	PEEK Parameters	PC Parameters
Nozzle diameter	0,4 mm	0,4 mm
Bed temperature	150 °C	90°C
Nozzle temperature	450°C	280°C
Printing speed	20 mm/s	20 mm/s
Walls number	0	0
Layer thickness	0,2 mm	0,2 mm
Infill density	100%	100%
Infill pattern	Lines	Lines
Fan	OFF	ON (75%)
Flow	100%	105%

Table 5.1: FFF process parameters for the 3D print of PEEK and PC samples.

5.1.2 Experimental setup

For this study, the plasma torch was fixed to a support equipped with a micrometric screw which allowed the torch to be raised relative to the surface of the sample with an accuracy of 0,01 mm (Figure 5.1 b). In this way it was possible to vary the working distance from 0,5 mm to 2 mm very precisely. In fact, since from the study of Korzec et al *[153]* it was found that the maximum activation area is obtained when the working distance (W.d.) is lower than 3 mm, it was decided to vary the W.d. between 0,5 mm and 2 mm (with intervals of 0,5 mm). However, from the same study, it emerged that for the same W.d., the activation area can increase as the treatment time increases according to a quasi-logarithmic trend (initial monotonous increase and subsequent plateau). Anyway, it was

verified that the maximum size of the activation area does not exceed 26 mm. For this reason and to minimize the time of the whole process, in this work the treatment times were chosen as 1 s, 2 s, 4 s and 5 s.

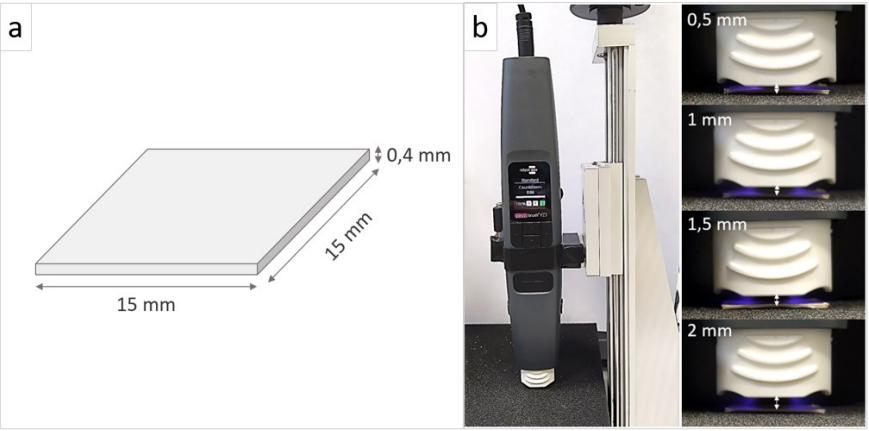

Figure 5.1: Sample shape and dimensions (a) and plasma torch set-up and working distances (b).

5.1.3 Surface Characterization

With a FLIR Thermal Camera it was possible to visualize the heat distribution on the surface of samples and measure the temperature in the hottest part. This measurement was carried out to evaluate whether temperature was a factor that could influence the surface features of the two materials.

The WCA analyses were performed by sessile drop method. In particular for each sample, a 3 µl drop of distilled water was deposited using a micropipette, an HDR photo of the drop was taken after 10 seconds and was processed using an online digital protractor [177]. The resulting measurement is an average of the left and right angles for each drop. To evaluate the surface aging due to the hydrophobic recovery phenomenon, the WCA measurement was repeated for each sample in the first 3 hours after treatment with 30 minutes intervals between one measurement and the next.

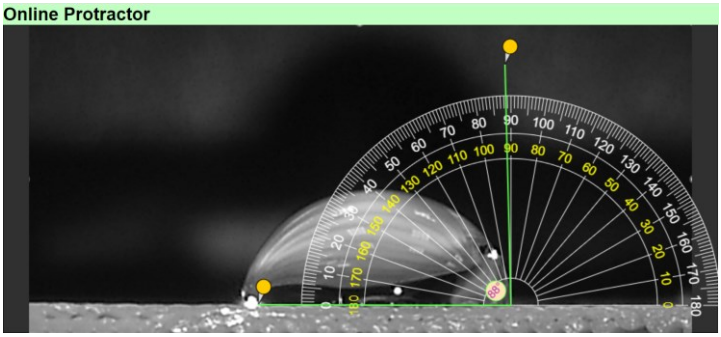

Figure 3.26: Contact Angle Measurement using the Online digital protractor.

The functional groups analyses were carried out using a Spectrum Two PerkinElmer FTIR spectrometer in attenuated total reflectance mode (ATR-FTIR). The analyses were conducted both before and approximately 5 min after treatment for each sample.

It was used a high-resolution Field Emission Scanning electron microscope (SEM), ZEISS Sigma 300 VP, to verify the effect of plasma treatment conditions on the surface morphology compared to the untreated samples. In order to observe the non-conductive samples in high vacuum mode (10^{-4} Pa) they were coated with a thin layer of gold by sputtering for 20s using Quorum Q 150R S plus sputter. The images were taken using the secondary electrons detectors (InLens and SE2) with an acceleration voltage of 5 kV and a magnification of 17000X.

5.1.4 Mechanical Test

After the characterization of the treated samples, the conditions (working distance and treatment time) that gave the best contact angle results were chosen to treat the Polycarbonate specimens to be mechanically tested. To estimate the effect of plasma on the interlayer adhesion of extruded PC the single lap shear test was performed following the ASTM D3163 Standard. The Ultimaker S5 3D printer was used to fabricate the samples, using the parameters listed in Table 5.1 and varying the raster angle. The aim was to evaluate the effect of plasma treatment also as a function of infill orientation, therefore the specimens were printed with extruded lines oriented along 0°, 90° and 45° with respect to the load direction. A total of 3 samples for each line orientation were fabricated and tested.

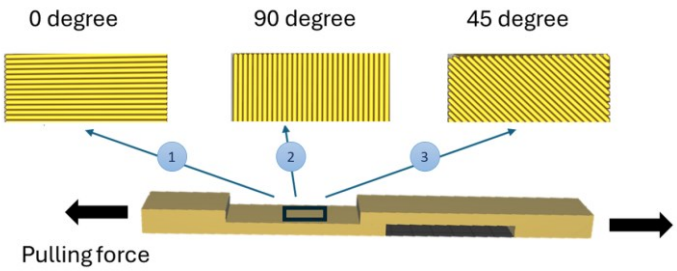

Figure 5.2: Schematic representation of Single Lap Shear sample and its lines orientations with respect to the load direction.

In other to perform the treatment, g-code was modified to automatically pause the print when the bottom layer was completed. The 3D printer machine was equipped with the cold plasma PZ3 torch: a custom-made setup was created to have a controlled gap between the tip of the torch and the printed layer to be treated. After the treatment, the plasma setup was removed and the print was resumed.

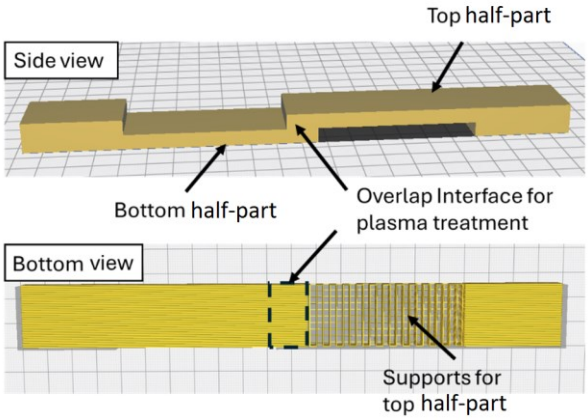

Figure 5.3: Single Lap Shear 3D printed specimen.

To correctly estimate the effect of the plasma treatment, and its benefit also non-treated samples were manufactured. It should be noted that, also the for the fabrication of non-treated samples the 3D printing process was paused for a total of about 2 min, to have the same boundary conditions.

5.2 Results and Discussion

5.2.1 Thermal Analysis

To evaluate if the plasma treatment could induce some morphological changes on the treated surfaces due to heating processes, thermal analyses were performed for each treatment condition. In Figure 5.4 are plotted the temperatures of the hottest area of sample for each treatment condition. It can be noted that as the treatment time increases, the temperature also increases by a few degrees. This increase is more evident moving from W.d. 0,5mm to W.d. 2 mm. This is in agreement with Korzec's study, as there is a rise in the active species that constitute the plasma due to the increase in treatment time and distance. [153] In any case, for all samples, the hottest area did not record a temperature above 35°C. Therefore, since the temperatures are much below the glass transition temperature (Tg) of the two treated polymers, it can be assumed that this heating has not a direct effect on the surface morphology, but this could be a very important factor to take into account for polymers with Tg lower than 35°C.

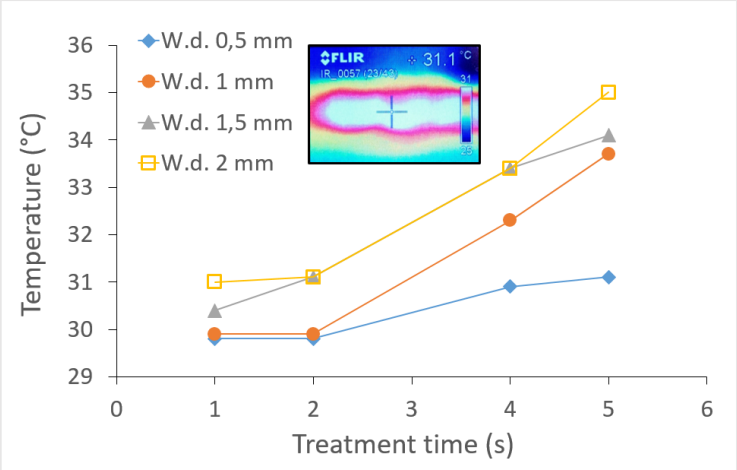

Figure 5.4: Temperature measurements of plasma-treated surfaces.

5.2.2 Water Contact Angle measurements

The wettability characterization of surfaces by means of sessile drop contact angle is a very simple method to evaluate changes in surface energy. It is well known that the higher

the surface energy the higher the wettability. In this study distilled water was used as test liquid by depositing a drop of 3 µl on each sample. The WCA measures were obtained from HDR photos of the drops using a digital protractor. Figure 5.5 is a representative image of the drops deposited on both virgin (untreated) and plasma-treated PEEK and PC samples.

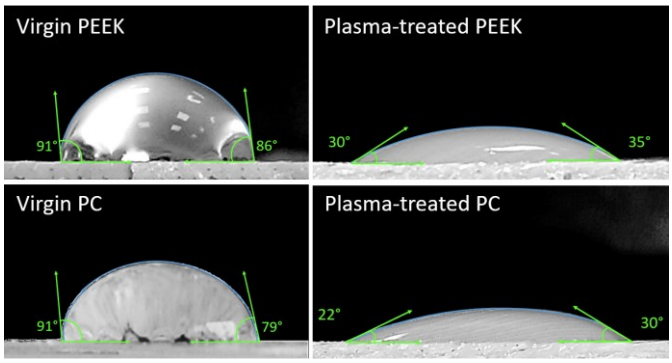

Figure 5.5: Photos of the drops deposited on both virgin and plasma-treated PEEK and PC samples respectively.

The results reported in Figure 5.6 are the average values of the right and left angles of each drop and were obtained from repeated measurements over time every 30 minutes up to 3 hours after treatment. This was used as qualitative method to evaluate the effectiveness of the treatment and the surface ageing due to hydrophobic recovery.

It is possible to note that in all cases, for both polymers, the plasma induced an increase in surface energy, i.e. in wettability, in fact the contact angles were reduced from $\theta > 80°$ for untreated samples, to $\theta < 60°$ for treated samples. It can be also noted that PC samples exhibit a better wettability than PEEK ones, with a post-treatment θ always lower than 45° and remained lower than 70° after 3 hours. The reasons for this could be linked to the greater chemical reactivity of amorphous PC compared to semicrystalline PEEK. Generally, the WCA measurement over time are consistent for the different treatment times for each working distance: the data follow approximately the same trend. From this first exploratory investigation, it seems that the best results for both polymers in overall terms of minimum treatment time, wettability immediately after treatment and surface aging are obtained for W.d. equal to 1 mm and 2 mm with 2 s of treatment time.

However, to have a better interpretation of the WCA results, IR analyses and SEM imaging were also used, to understand the influence of the plasma on the surface chemistry and morphology.

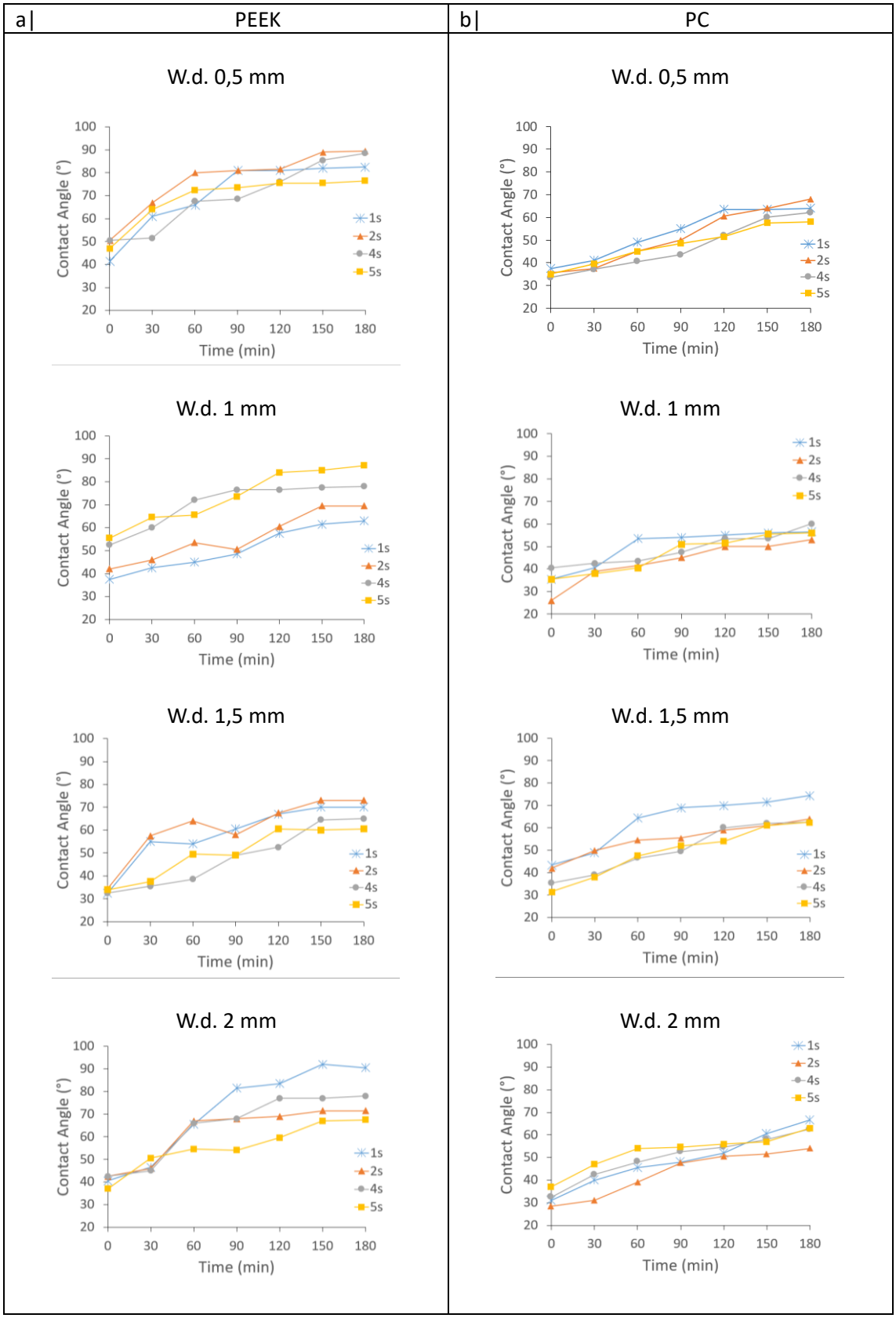

Figure 5.6: Surface ageing evaluation of each treatment by means of WCA analysis for both materials (a) PEEK and (b) PC respectively.

5.2.3 ATR-FTIR Spectroscopy

All treated and untreated samples were analyzed by FT IR spectroscopy in attenuated total reflectance (ATR) mode. For treated samples, the analyses were performed approximately after 5 minutes from the treatment. All ATR-FTIR spectra were recorded in absorbance (in a wavenumber range from 3800 to 650 cm^{-1}), baseline-adjusted, and normalized so they could be compared to each other. Both in the case of treated PEEK and in the case of treated PC, the same result was obtained for all treatment conditions, making it impossible to distinguish which treatment condition returned greater surface functionalization. Therefore, it is possible that IR spectroscopy alone cannot explain the differences in wettability obtained in the various treatment conditions as it analyzes a surface depth of just 1 micron. It is possible instead that the differences in wettability are due to other factors linked to morphological variations of the surface.

This paragraph reports the variations in the functional groups, present on the main polymer chains, which were obtained by plasma treatment. Figure 5.7 and Figure 5.8 show the PEEK and PC ATR-FTIR spectra respectively, for both treated (continuous red line) and virgin (dotted blue line) polymers. All the functional groups vibrations for PEEK and PC are listed in Table 5.2 and Table 5.3. From Figure 5.7 a and Figure 5.8 a is very evident the presence of the -OH stretching vibration band having the peak maximum centered around 3300 cm^{-1} indicating that it is the stretching of -OH with intramolecular bonds (for example hydrogen bond in -COOH groups). In the wavenumber range of 3050-2800 cm^{-1} it could be noted an increase in the stretching vibrations of sp^2 and sp^3 C-H bonds, probably due to breaking of the main chain into smaller segments having more degrees of vibrational freedom. This last hypothesis is supported by the fact that, considering the PEEK spectra in Figure 5.7 b and c, a decrease in CH=CH stretching of aromatic rings and an increase in C-H bending in plane are visible. For both polymers, an increase in absorbance of C=O stretching vibrations at 1650 cm^{-1} and at 1750 cm^{-1} related to the C=O stretching vibrations in carboxyl/ester groups are present (Figure 5.7 b and Figure 5.8 b).

From these results it can be deduced that the plasma-induced functional groups are hydroxyl, carboxyl, and carbonyl which could act as anchor groups between successive layers.

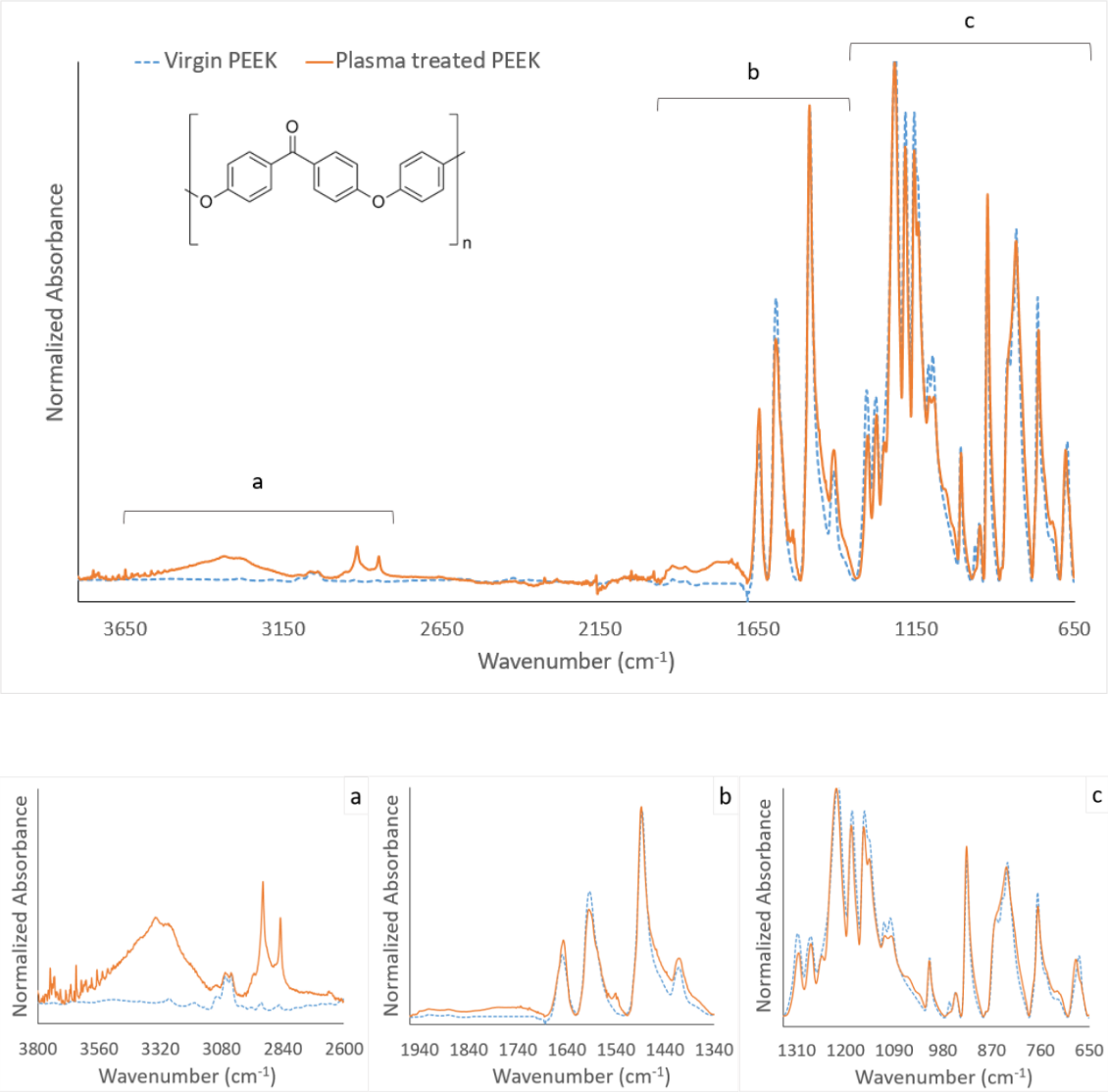

Figure 5.7: ATR-FTIR spectra of treated (continuous red line) and virgin (dotted blue line) PEEK. Focus on the spectra regions: (a) 3800-2600 cm^{-1}, (b) 1950-1350 cm^{-1}, (c) 1350-650 cm^{-1}.

Wavenumber (cm^{-1})	Intensity/shape	Corresponding bonds and functional groups	Virgin PEEK	Plasma-treated PEEK
3600-3000 band peak maximum at 3300	w/br	νO-H bonded	no	yes
3053, 3035	w	νC-H sp^2, aromatic	yes	increased intensity
2918, 2853	w/sh	νC-H sp^3	no	yes
2000-1800 band	w/br	ring harmonics	yes	yes
1750	w/br	νC=O carboxyl/ester group	no	yes
1650	s-m/sh	νC=O diaryl ketone	yes	yes
1594	s-m/sh	νCH=CH aromatic ring vibrations	yes	slightly reduced intensity
1487	s/sh	ν(Ar-O-Ar)	yes	yes
1404	m-w/sh	νC=C	yes	yes
1305 1280	m/sh	ν_{as}C=O diaryl ketone ν_{as}(Ar-O-Ar)	yes	slightly reduced intensity
1245	w	δO-H	no	yes
1217	s/sh	ν_{as}(Ar-O-Ar)	yes	yes
1186 1157	s/sh	ν_{as}(Ar-O-Ar) νAr-O, νAr-(C=O)	yes	slightly reduced intensity
1105 1096	m-w/sh	ν_{as}(Ar-O-Ar)	yes	slightly reduced intensity
1051 1029	w/br	δC-H in plane	no	yes
1010 946	m-w/sh w	δC-H aromatic νC-H aromatic out of plane vibrations	yes	yes
925	s/sh	νC=O diaryl ketone	yes	slightly increased intensity
834 765 677	m-s/br m-s/sh m-w/sh	out of plane δC-H aromatic and δC-O-C bonds	yes	yes

Table 5.2: Virgin and plasma-treated PEEK functional groups IR vibrations.

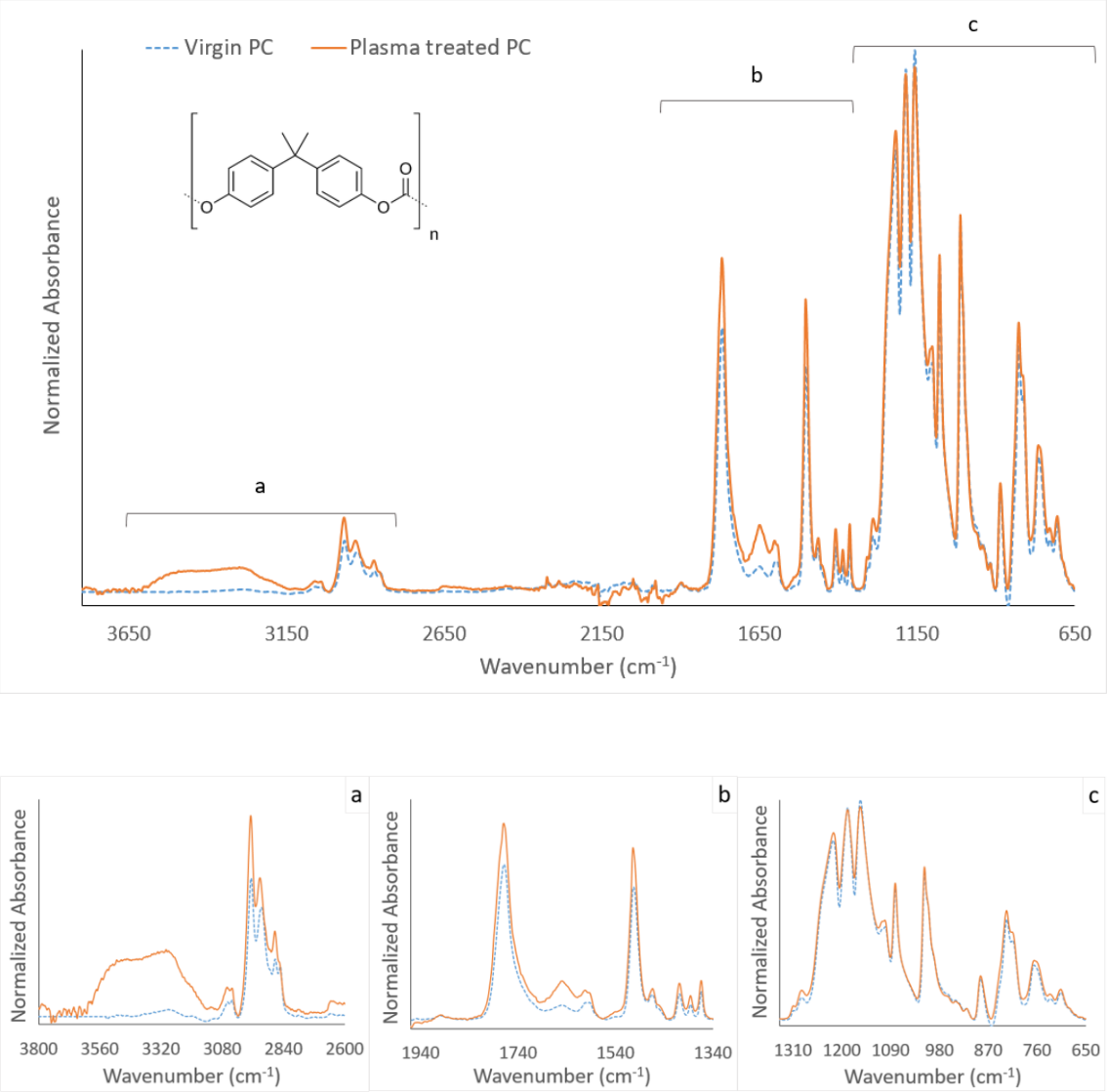

Figure 5.8: ATR-FTIR spectra of treated (continuous red line) and virgin (dotted blue line) PC. Focus on the spectra regions: (a) 3800-2600 cm^{-1}, (b) 1950-1350 cm^{-1}, (c) 1350-650 cm^{-1}.

Wavenumber (cm^{-1})	Intensity/shape	Corresponding bonds and functional groups	Virgin PEEK	Plasma-treated PEEK
3600-3100 band peak maximum at 3300	w/br	νO-H bonded	no	yes
3053, 3035	w	νC-H sp^2, aromatic	yes	yes
2963, 2927, 2871	w/br	νC-H sp^3	yes	slightly increased intensity
2000-1800 band	w/br	ring harmonics	yes	yes
1750, 1650	w/br	νC=O carbonate group, carboxyl group	yes	increased intensity
1570-1430	s-m/sh	νCH=CH aromatic ring vibrations	yes	increased intensity
region 1428-1348	w/sh	δC-H sp^2 and sp^3	yes	yes
region 1300-1000	s/sh	νC-O-C	yes	yes
region 900-700	m /sh	δC-H aromatic out of plane vibrations	yes	yes

Table 5.3: Virgin and plasma-treated PC functional groups IR vibrations.

5.2.4 SEM Imaging

To verify if there were plasma-induced surface morphological changes, Scanning Electron Microscopy imaging was performed. The untreated PEEK and PC samples are shown in Figure 5.9. In Figure 5.10 and Figure 5.11 the images of all the plasma-treated PEEK are shown, while in Figure 5.12 and Figure 5.13 the images of all the plasma-treated PC samples are collected.

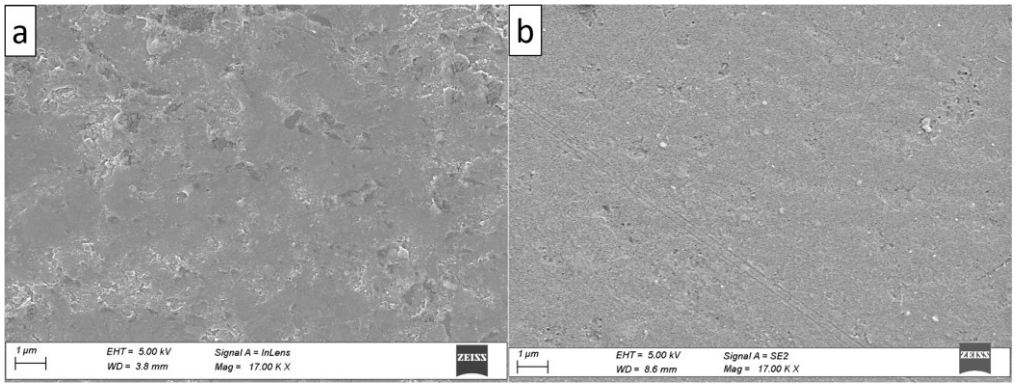

Figure 5.9: SEM micrographs of virgin PEEK (a) and virgin PC (b) surfaces.

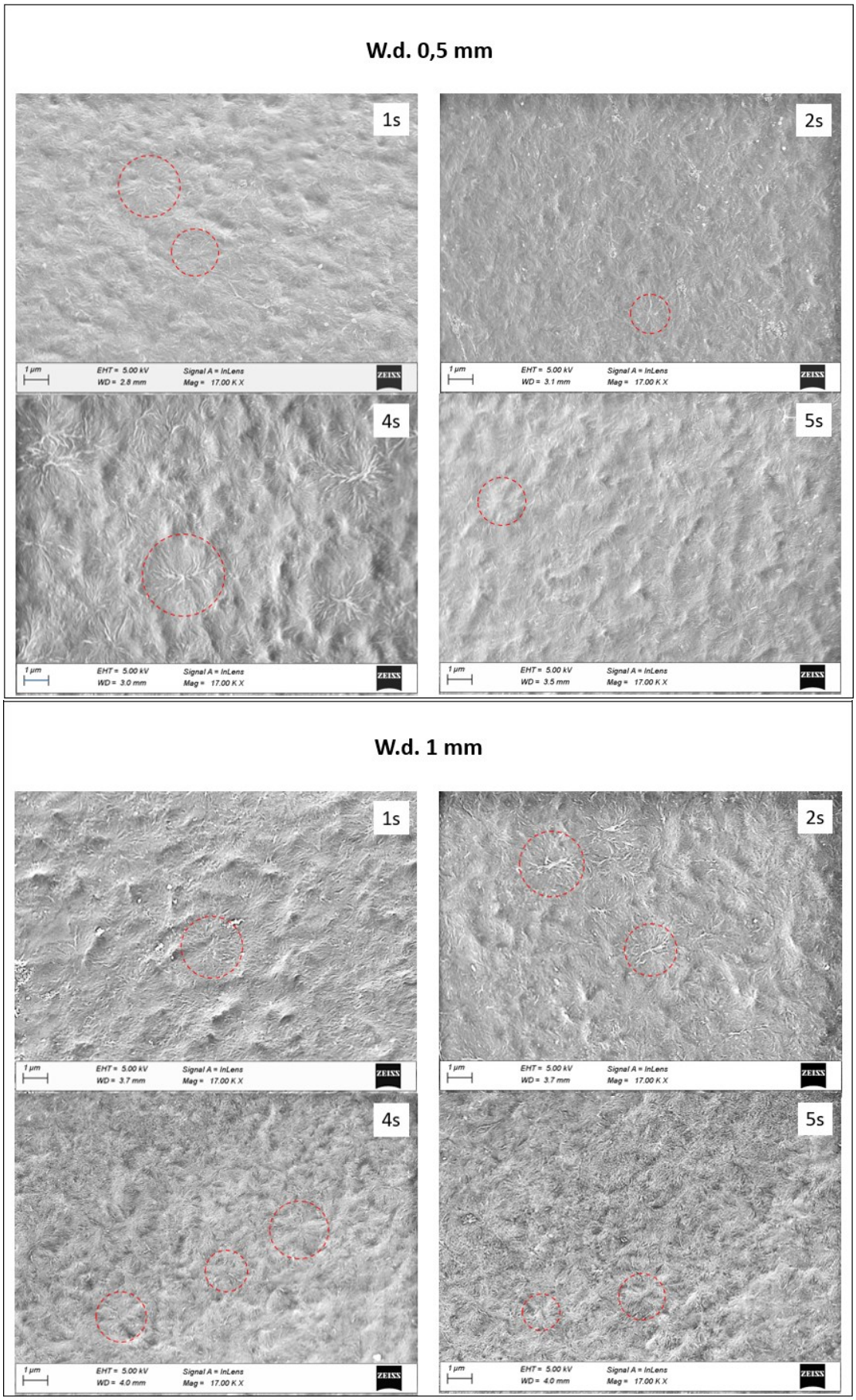

Figure 5.10: SEM micrographs of all the plasma-treated PEEK samples.

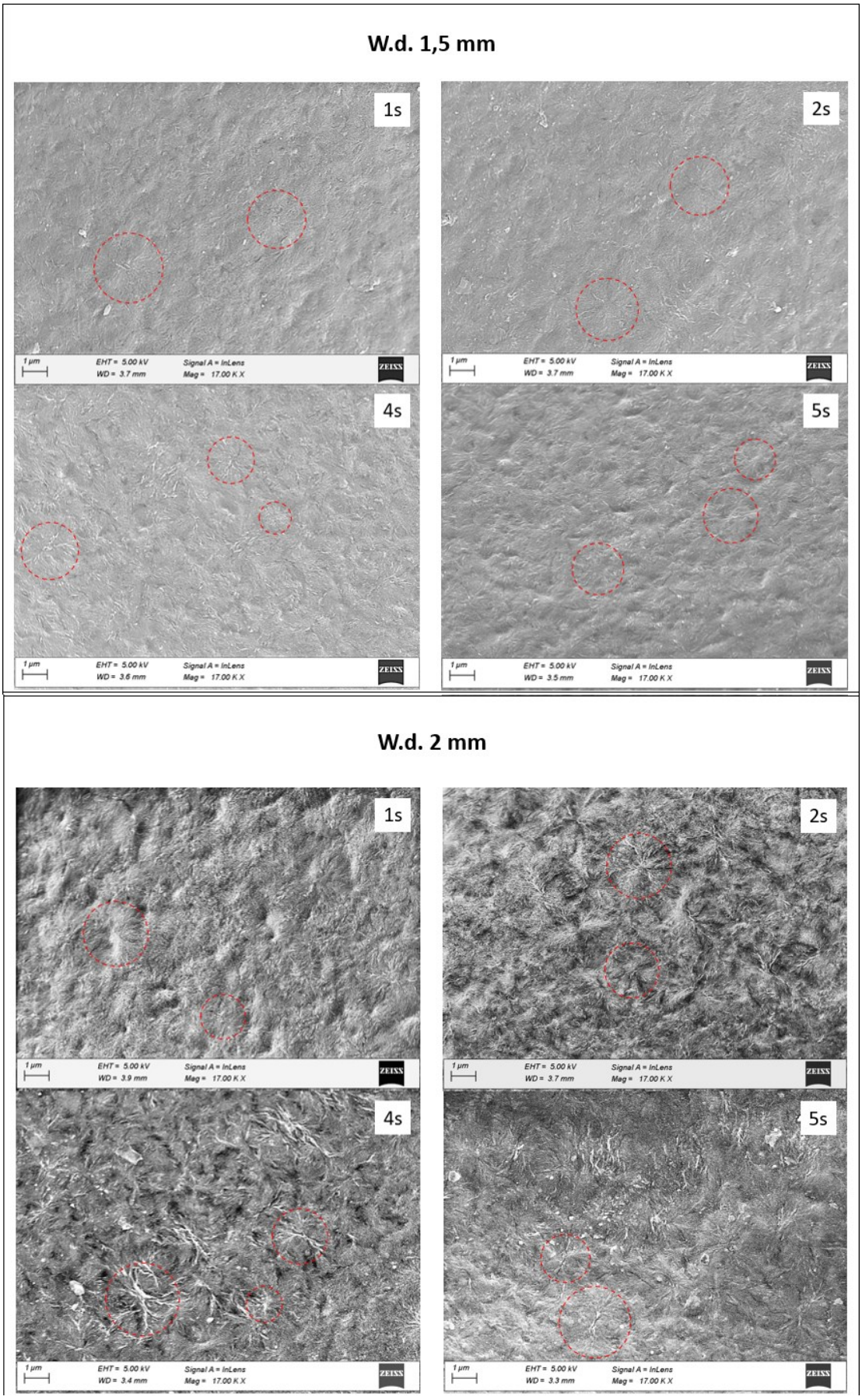

Figure 5.11: SEM micrographs of all the plasma-treated PEEK samples.

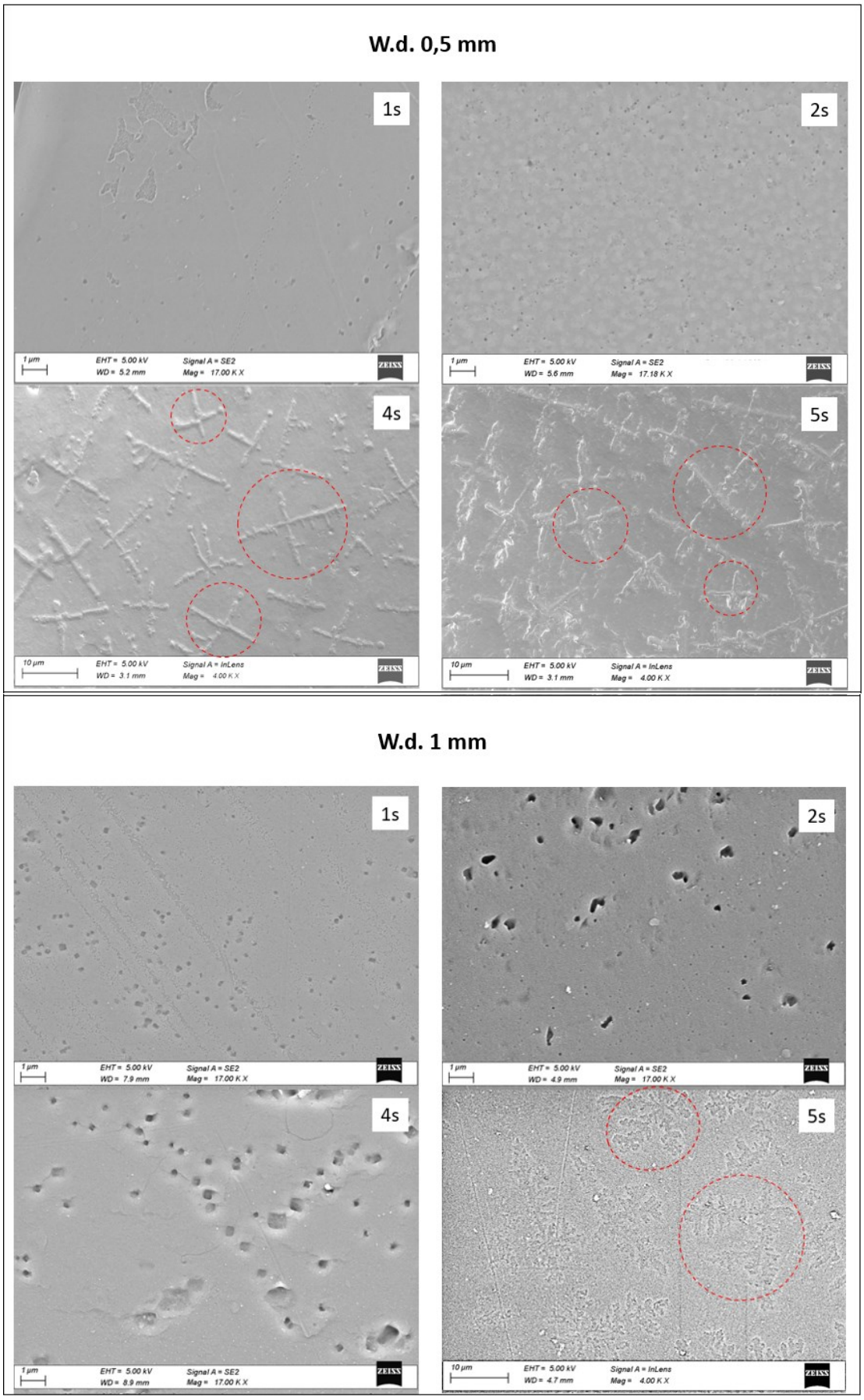

Figure 5.12: SEM micrographs of all the plasma-treated PC samples.

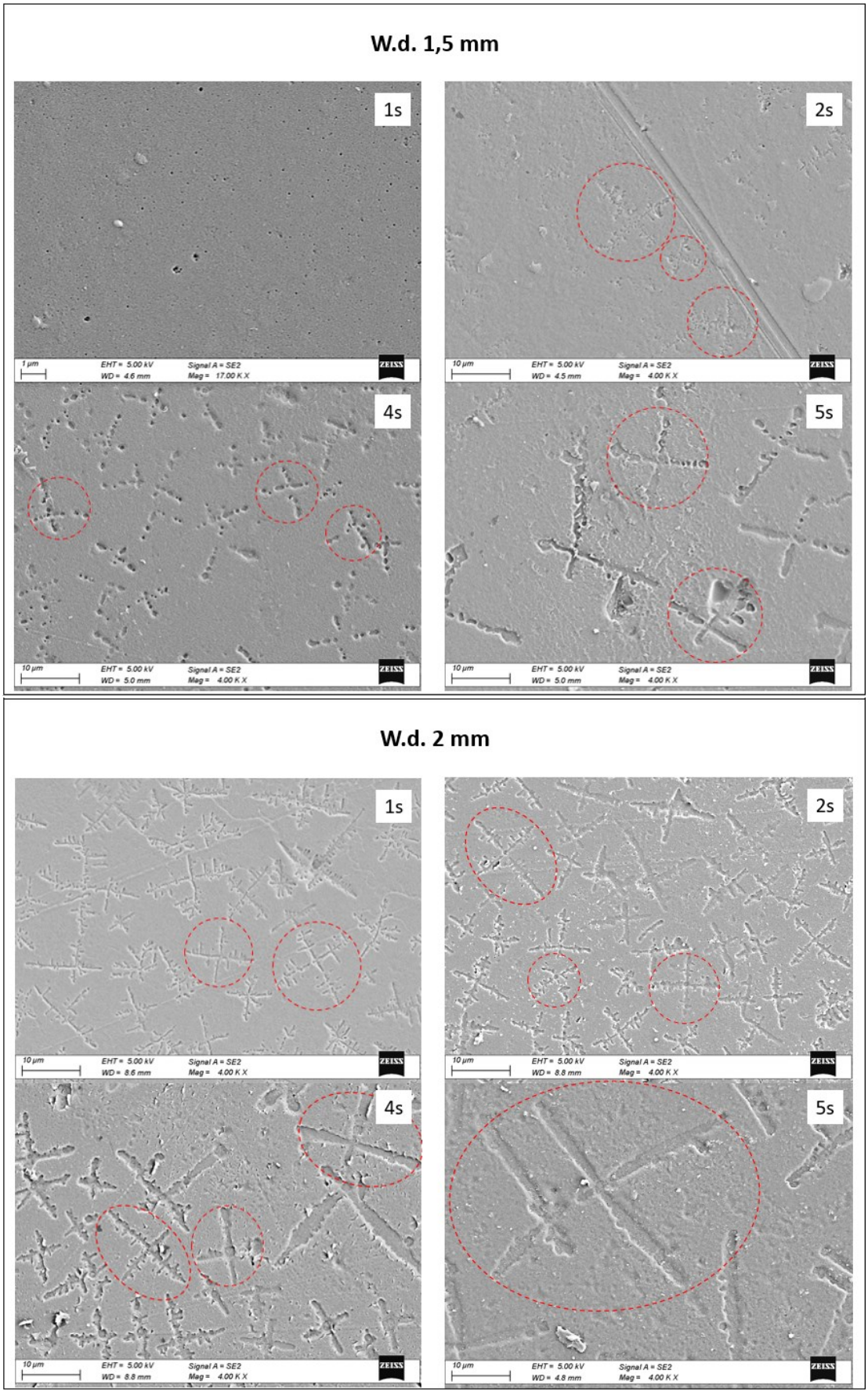

Figure 5.13: SEM micrographs of all the plasma-treated PC samples.

From Figure 5.10 and Figure 5.11 it is evident that in all treatment conditions, plasma induces crystallization on the surface of PEEK with the formation of spherulites. This is in agreement with a work of Al Khatib et al [178] according to which crystallization of PEEK is induced by the plasma through ion bombardment. These spherulites, with dimensions between 1 μm and 3 μm, are difficult to distinguish separately because they are attached to each other, completely occupying the surface. Another observation that can be made is that the working distance has a greater influence on crystallization than the treatment time. This probably occurs due to the reduction in the reactivity of chemically active species as the W.d. increases therefore ion bombardment prevails over functionalization breaking bonds and promoting cross-linking between polymer chain segments. [153]

As can be seen from both Figure 5.12 and Figure 5.13, plasma can induce the crystallization of commonly amorphous polymers such as PC, as well. It is well known in literature how difficult it is to thermally crystallize PC, and how expensive it is in terms of time and energy. In this case, however, just a few seconds of treatment are enough to induce the formation of spherulites on PC surface. As seen for PEEK samples, also for PC the working distance influences the crystallization more than the treatment time. As a matter of facts, when the torch was positioned at a distance less than 2 mm from the surface, at least 4 s of treatment time were needed to trigger the crystallization process. Instead, increasing the distance to 2 mm, it was possible to obtain spherulites even with just one second of treatment. Observing the PC crystallites, compared to PEEK, they are numerically fewer but with much larger dimensions (ranging from 8 μm to 60 μm).
For distances less than 2 mm and treatment time of 1 and 2 seconds, the main effect of plasma on surface morphology is ablation: the surfaces appear smoother than the untreated polymer with the presence of small porosities.

Generally, roughness, crystallinity and chemical functionalization are factors that can determine the variation in surface wettability of a material. In this case, no difference in chemical functionalization was revealed by IR analysis and, through SEM imaging, it was possible to see the surface morphology but not to measure the roughness. Therefore, it was not possible to give an absolute interpretation of which factor influences surface hydrophilicity most of all, but certainly the variation in wettability is the result of the combination of these 3 factors. However, by looking at contact angles results, it could be noted that the aging process (hydrophobic recovery) is slower for more crystalline

samples. This probably happens due to the impediments caused by cross-linking and lower mobility of the polymer chains.

Definitely, to evaluate the improvement of the interlayer adhesion through mechanical tests, the treatment conditions were chosen based on the treatment time and working distances which allowed to obtain lower contact angles on average: 2 s and 2 mm. Furthermore, to understand if the crystals size has an influence on mechanical properties, the condition with W.d. = 2mm and 5 s of treatment time was also tested.

5.2.5 Single Lap Shear (SLS) test

Single Lap Shear (SLS) test was performed according to ASTM D3163 standard using the Instron 5582 universal testing machine at a crosshead rate of 2 mm/min, to estimate the effect of plasma on the interface adhesion of 3D printed PC. From the stress-strain curves, the Interlaminar Shear Strength (ILSS) was used as a metric to evaluate interface adhesion for non-treated and treated samples. The 3D printer machine was equipped with the cold plasma torch to have a gap of 2 mm between the tip of the torch and the overlap interface area (see Figure 5.14). The plasma treatment was performed for 2 s (according to the best results found out in previous sections).

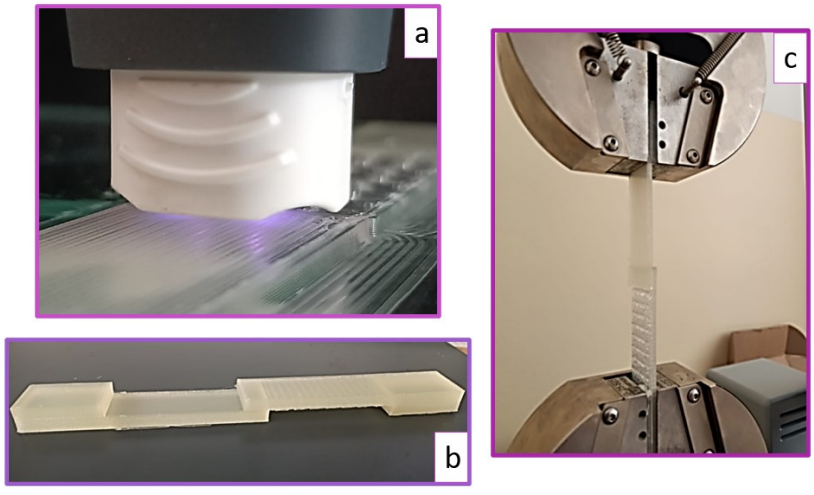

Figure 5.14: Plasma torch during SLS sample surface treatment (a), 3D printed PC sample (b), Test setup (c) .

All the results are collected in Table 5.4 and the following considerations can be drawn:

- In all cases plasma leads to an increase in ILSS of between 25% and 30%. Looking at the standard deviations obtained on 3 specimens for each layer orientation, the results show excellent reproducibility of the process.
- The samples having the raster lines oriented along 45° and 90° directions showed almost the same improvement in interlayer adhesion, exhibited in both cases an ILSS of ~25%.
- As expected, the best results were obtained for the orientation of the lines at 0° with respect to the direction of the load, obtaining 30,7% ILSS improvement.

After proving that the plasma treatment brings an improvement in adhesion almost regardless of the orientation of the lines, it was decided to investigate the effect of layer height. As well known, from scientific literature, the lower the layer height the higher the adhesion. Such correlation is described in Coogan et al [179] [180], and it relies on two factors: contact area and pressure between consecutive layers. When layer height is low, the contact area between two consecutive layers is high, as well as the pressure.

A layer height of 0,3 mm was set in conjunction with a line orientation equal to 0 degree (parallel to the load direction) was set, being the best orientation for the SLS test. As expected, the interface adhesion is lower compared to the one obtained at layer height of 0,2. On the other hand, the effect of plasma treatment produced almost the same increase in adhesion obtained when the layer height was 0,2 mm, obtaining an improvement of 29,1%. Also in this case, the plasma treatment was demonstrated to be layer height-free.

Lines Orientation (°)	Layer Height (mm)	Untreated specimens		Plasma-treated specimens		Improvement in ILSS (%)
		ILSS average (MPa)	Std. Dev. (MPa)	ILSS average (MPa)	Std. Dev. (%)	
0	0,2	44,5	±2,5	58,2	±4,0	30,7
90	0,2	27,8	±3,3	34,8	±4,2	25,3
45	0,2	20,3	±1,0	25,3	±1,2	24,8
0	0,3	32,6	±1,8	42,0	±2,8	29,1

Table 5.4: Single Lap Shear test results for untreated and treated samples.

Finally, a layer height of 0,2 mm and a line orientation of 0° was set, to investigate a new variable: plasma treatment time. SEM images clearly show that a plasma treatment of 5s

produce bigger crystals. This effect was investigated by producing and testing 3 samples treated for 5 s instead of 2 s at the same working distance of 2 mm. From ILSS reported in Table 5.5 it is shown that there is a further 0,4% increase in adhesion when the treatment time was 5 s compared to 2 s results. This result could be indicative of the fact that the degree of crystallization and the size of the crystals also influence the mechanical adhesion between the layers in synergy with the chemical functionalization. Furthermore, the slight increase in contact angle could explained by the increased surface roughness due to the formation of larger crystals.

Treatment Time (s)	Untreated specimens		Plasma-treated specimens		Improvement in ILSS (%)
	ILSS average (MPa)	Std. Dev. (MPa)	ILSS average (MPa)	Std. Dev. (%)	
2	44,5	±2,5	58,2	±4,0	30,7
5	44,3	±1,9	59,7	±3,2	34,7

Table 5.5: Comparison of UTS results obtained for two different treatment time: 2 s and 5 s.

In summary, the present research work has allowed us to study in depth the effect of plasma treatment on the surfaces of PEEK and PC engineering polymers. In particular, the influence of two process parameters, i.e. treatment time and working distance, on the improvement of the wettability of the polymer was studied. The latter was evaluated using contact angle measurements and FTIR analysis. The FTIR analysis revealed the appearance of new polar functional groups (carboxylic and hydroxyl) and a slight increase in the intensity of the peak relating to the stretching of the carbonyl group for all the treated samples. Not being able to quantify, using FTIR, significant differences in chemical functionalization for the various treatment conditions used, it was decided to continue the study with contact angle measurements. On average, a lowering of the contact angle greater than 50% was found, highlighting an increase in surface energy for both materials mainly due to the chemical functionalization evaluated by FTIR. Through WCA analysis it was also possible to evaluate the aging of the treatment which seems to occur faster for PEEK than for PC. In fact, in many cases, PEEK shows contact angles greater than 70° after approximately 1 h -2 h, restoring the hydrophobic condition (prior to treatment) after 3 h. Instead, the PC continues to maintain contact angles less than 70° even 3 hours after treatment. From the contact angle measurements it was difficult to

understand how both the treatment time and the distance from the surface could influence the wettability. It was therefore hypothesized that in addition to chemical functionalization, other phenomena involving changes in surface morphology could contribute to this variation. The SEM investigations confirmed the fact that the plasma in some cases made the surfaces cleaner by lowering the average roughness, in other cases it induced the formation of crystallites typical of PEEK but not of PC. It was surprising to find the formation of crystals even in the PC, notoriously amorphous, larger in size than those formed in PEEK. Finally, it was decided to mechanically test samples treated in the conditions that gave the lowest contact angle, i.e. 2 mm and 2 s. Through the shear test results, an increase in adhesion of 30,7% was found compared to the untreated material. Furthermore, the treatment condition with W.d. at 2 mm and 5 s of treatment time, which gave rise to larger PC crystals, was tested. In this case the increase in adhesion was found to be 34,7%, showing how the size of the crystals also plays an important role in interlayer adhesion. These mechanical results obtained on PC suggest that also for PEEK it is possible to obtain a significant increase in interlayer adhesion using an atmospheric plasma treatment generated by a PDD torch.

6 Characterization of 3D printed C-PEEK gyroid-lattice structures

Fused Filament Fabrication allows the creation of lightened parts not only through the choice of lighter materials but also through topological optimization or the choice of infill patterns that allow obtaining high strength-to-weight ratios of the part. This chapter presents a comprehensive study on the compressive strength behavior and impact absorption capability of FFF printed Carbon fiber reinforced Polyether ether ketone (C-PEEK) lattice structures having different infill density percentages. The chosen pattern is the gyroid, interesting for being a bio-inspired triple periodic minimal surface (TPMS) - type structure. The main objective was to find the density that maximizes the compressive strength-to-weight ratio, optimizing the manufacturing time and the material cost. The study was extended to the x,y,z loading directions in order to estimate compression isotropy of 3D printed gyroids. These studies aimed to overcome several challenges related to producing components through FFF, including high material costs, long printing times, mechanical anisotropy of parts, design constraints, and the use of supports. Furthermore, all these findings served as a starting point for the construction of 3D printed sandwich panels with gyroid filled cores to evaluate their ability to absorb impact energies.

6.1 Compressive behavior

After having optimized the FFF process of virgin PEEK and studied the process parameters that most influence crystallinity and mechanical performance, the main objective was to exploit the properties conferred by the carbon fibers to PEEK to obtain even lighter and higher performing parts. For this reason, it was decided to mechanically characterize the C-PEEK gyroid structures. In this part of the work, it was studied the effect of the gyroid infill pattern in C-PEEK 3D printed samples on compression strength. A study on the process parameters (infill density and printing speed) was performed in order to optimize the printing process and the strength-to-weight ratio.

6.1.1 Design of Experiment

Gyroid C-PEEK specimens were fabricated using the Roboze One+400 3D printer, with

the commercial Roboze C-PEEK filament as the feedstock. The filament and 3D printing machine key features are well described in Chapter 3.

The slicing software used to generate the G-code was Ultimaker Cura 5.2.1, into which the Roboze One+400 printer and material specifications were configured.

Compression tests were conducted using an Instron 5582 machine with a 100 kN load cell to assess the strength of the printed specimens. These tests followed the ASTM C365 standard (minimum specimen area: 625 mm²; standard environmental conditions; testing speed set to produce failure within 6 minutes), while the test speed was based on ASTM D695 (1,3 mm/min). The compression test setup and specimen design are illustrated in Figure 6.1.

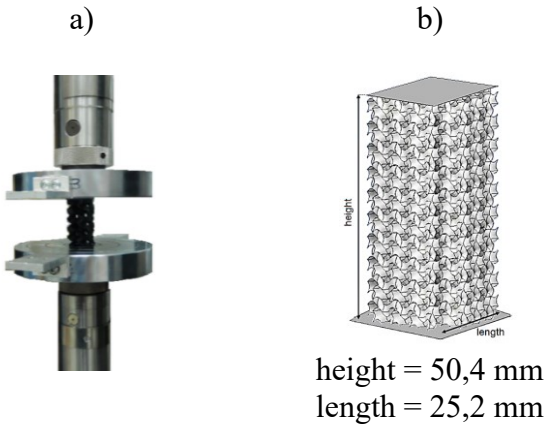

Figure 6.1: Compression test setup a); specimen shape and dimensions b).

The compressive strength behavior of gyroid-structured specimens was examined by varying both infill density and printing speed. Since the study reported in Chapter 4 showed that the printing speed influences the adhesion between the layers and consequently the mechanical resistance of the part, it was decided to test different speeds also in this case, specifically: 17, 20, 23, and 30 mm/s. The infill density ranged from 5% to 25% (in increments of 5%) for the first three speeds. For the speed of 30 mm/s, the infill density was tested across a broader range, from 5% to 100%. It was observed that within the 5% to 25% infill density range, the influence of printing speed on compressive strength was negligible. Consequently, to optimize production time and material usage, the study was extended to 100% infill density only for the 30 mm/s speed. Finally, unlike what was done for the printing of the PEEK samples in Chapter 4, the layer thickness chosen for the printing of the gyroid structures is 0,1 mm because of the higher dimensional and thermal stability of C-PEEK than pure PEEK thanks to the presence of

carbon fibers, thus reducing the risk of nozzle clogging and polymer swelling or warping. All key constant printing parameters are listed in Table 6.1, where nozzle temperature and bed temperature were the same of that used for PEEK 3D printing in Chapter 5.

Constant Parameters	
Nozzle diameter	0,4 mm
Bed temperature	150 °C
Nozzle temperature	450°C
Walls number	0
Top layers	6
Bottom layers	6
Layer thickness	0,1 mm
Infill pattern	Gyroid

Table 6.1: Main printing parameters kept constant for all printed specimens.

For the study of the compressive strength of the gyroid structures, it was decided not to print the walls of the specimens so that they would not influence the test results, instead it was decided to print 6 layers for both the top and the bottom to stabilize the surfaces that would come into contact with the plates of the testing machine and ensure a homogeneous distribution of the loads.

The experimental design is summarized in Table 6.2 including the number of specimens for each condition.

Experimental parameters		
Printing Speed	Infill density	Number of specimens
17 mm/s	From 5% to 25%	5 for each infill %
20 mm/s	From 5% to 25%	5 for each infill %
23 mm/s	From 5% to 25%	5 for each infill %
30 mm/s	From 5% to 100%	5 for each infill %

Table 6.2: Design of experiment.

Finally, the tested samples were observed by using the Hirox RH – 2000 digital Optical Microscope in order to analyse the failure modes. The optical characterization of the deformation behaviour of samples under compression stress was carried out with a magnification of 35 times.

6.1.2 Results and Discussion

The stress-strain curves obtained by compression test are displayed in Figure 6.2. At beginning the curves grow linearly defining the elastic region. Afterwards, other cells of the structure are involved in withstanding the load until the ultimate point is reached. After this point, there is the onset of the crushing or the buckling of the structure leading to a reduction in compression stress. Then, the compression stress increases again due to the densification of the lattice cells. In all the tests, the stress-strain curves gradually develop a plateau. Such stress-strain curves show a ductile failure of the specimens in which the lattice cells do not experience catastrophic break. This is expected thanks to the gradual distribution of load through the structure. The Figure 6.3 is a representative picture of the specimens before and after test.

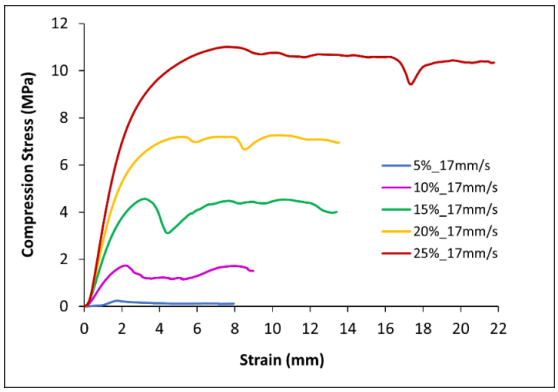

Figure 6.2: Stress-strain curves for samples printed at 17 mm/s of print speed.

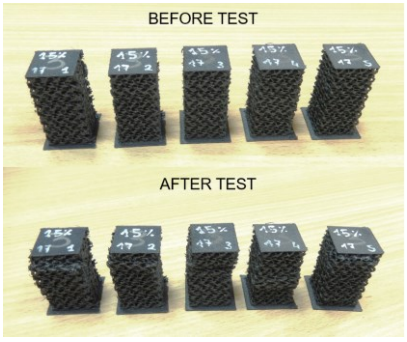

Figure 6.3: Specimens before and after compression test.

From the ultimate point, the compressive strength was extrapolated and all the results are collected in Table 6.3. What is noteworthy is that, over all, as the infill density increases, also the compressive strength increases. This phenomenon occurs because the increased number of unitary cells corresponds to an increase in struts cross-section area that carry the load.

Print speed (mm/s)	Infill density (%)	Nominal weight (g)	Compressive strength (MPa)	Standard deviation (MPa)	Compressive strength/weight (MPa/g)
17	5	2,13	0,26	± 0,07	0,12
	10	4,26	1,79	± 0,47	0,42
	15	6,39	4,18	± 0,78	0,65
	20	8,51	7,12	± 0,79	0,84
	25	10,64	10,75	± 0,56	1,01
20	5	2,13	0,58	± 0,06	0,27
	10	4,26	2,05	± 0,33	0,48
	15	6,39	4,56	± 0,61	0,71
	20	8,51	7,27	± 0,86	0,85
	25	10,64	11,04	± 0,23	1,04
23	5	2,13	0,36	± 0,06	0,17
	10	4,26	1,816	± 0,32	0,43
	15	6,39	4,04	± 0,42	0,63
	20	8,51	7,18	± 0,64	0,84
	25	10,64	10,82	± 0,48	1,02
30	5	2,13	0,24	± 0,06	0,11
	10	4,26	1,63	± 0,35	0,38
	15	6,39	3,59	± 0,49	0,56
	20	8,51	6,58	± 0,85	0,77
	25	10,64	10,24	± 0,61	0,96
	30	12,77	13,17	± 0,66	1,03
	35	14,9	21,11	± 1,11	1,42
	40	17,03	23,91	± 1,14	1,4
	45	19,16	32,53	± 1,25	1,7
	50	21,29	35,97	± 1,54	1,69
	55	23,41	43,54	± 1,08	1,86
	60	25,54	57,12	± 0,89	2,24
	65	27,67	63,21	± 0,64	2,28
	70	29,8	77,15	± 0,63	2,59
	75	31,93	84,34	± 0,71	2,64
	80	34,06	88,53	± 0,82	2,6
	85	36,18	92,67	± 0,49	2,56
	90	38,31	100,43	± 0,55	2,62
	95	40,44	101,06	± 1,09	2,5
	100	42,57	106,01	± 0,99	2,5

Table 6.3: Compression test results.

The Figure 6.4 shows the compressive strength plotted versus the infill density for each printing speed and the residual plots, respectively. All the curves follow almost the same power law trend in accordance with the Gibson-Ashby model (Eq. 9) [181]:

$$\frac{\sigma}{\sigma_0} = C\left(\frac{\rho}{\rho_0}\right)^n \Rightarrow \sigma = \sigma_0 C\left(\frac{\rho}{\rho_0}\right)^n \qquad \text{Eq. 9}$$

Where: σ is the compressive strength of the lattice structure, ρ is the lattice material density, σ_0 and ρ_0 are the compressive strength and the density of the bulk material respectively (for C-PEEK used in this work: σ_0 = 229 MPa and ρ0 = 1,33 g/cm^3), C and n are constant whose value was obtained by fitting the data. According to the model, based on the value of n, it is possible to categorize the structures into two types: if n is equal to 1 it is an ideal stretching-dominated structure, to 3/2 it is an ideal bending-dominated structure. In this case, n ranges from 1,83 to 1,93 and C from 1,03 to 1,16 indicating that the data are in better agreement with the Gibson-Ashby prediction for bending-dominated (BD) lattices [182]. However, the samples showed also some similarities to stretching-dominant (SD) structures which collapse especially for buckling phenomena. Furthermore, it was studied that, under compression, the BD stress-strain curves exhibit three zones: elastic, constant plateau and densification, instead the SD exhibit stress oscillations in the plateau zone followed by densification [182]. This means that, unlike the BD structures that collapse uniformly leading to barreling, the SD structures fail by step of consecutive unit cells collapses. The behaviors of the stress-strain curves in Figure 6.2, showed that the oscillations in the plateau zone are not very pronounced and their intensity decreases as the size of the cells increases. In fact, buckling occurs by increasing the infill density. This is because of the increase in lattice interconnections which act as load-bearing struts aligned with the loading direction as in SD structures. For lower densities, there is more BD behavior in which the unit cells fail due to bending stress.

In all cases, the power law equations obtained by regression can be used to predict approximately the strength value that the structure will have at a particular infill density with a confidence and prediction intervals of 95%.

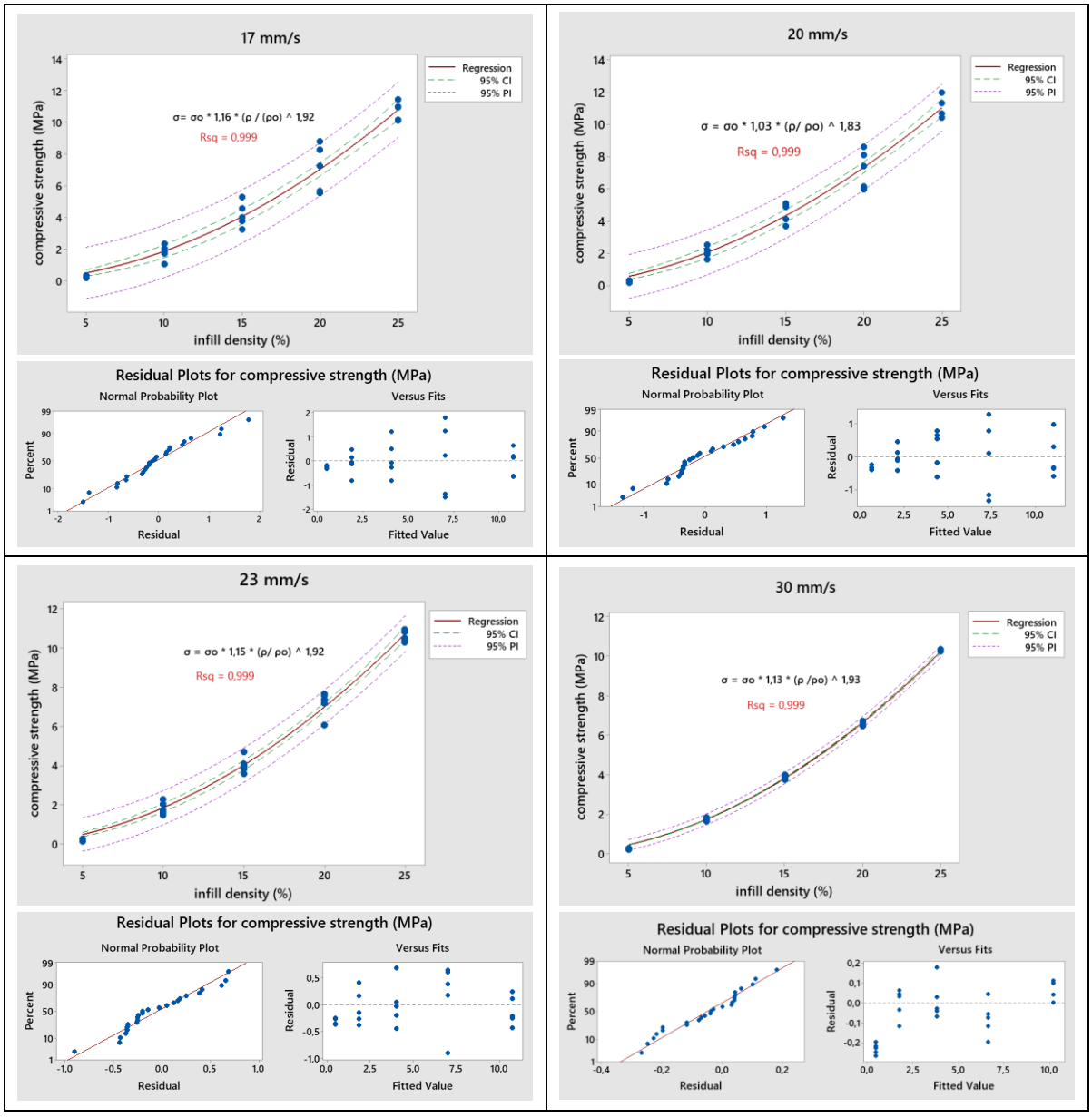

Figure 6.4: Compressive Strength vs Infill density curves and residual plots for each print speed.

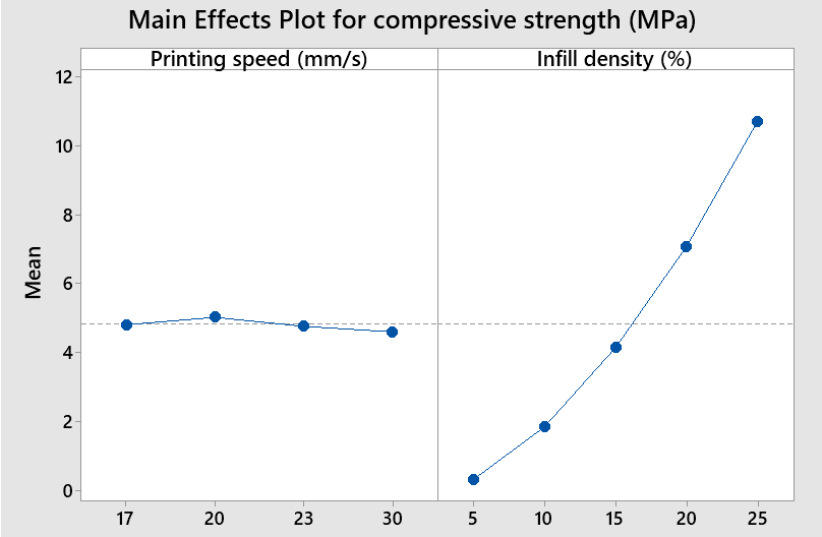

Figure 6.5: Main effect plot for Compressive strength.

Moreover, from Figure 6.5, it is evident that the printing speed doesn't influence the compressive performance, and it's effect is negligible within the standard error. For this reason, it was decided to continue the study until the 100% infill density only for the higher printing speed in order to reduce the printing time. The results are represented graphically in Figure 6.6. The data follow the power law trend up to 70% of infill density, then a change in curvature occurs. By plotting the compressive strength-to-weight ratio versus the infill density (Figure 6.7), it can be noted that there is a linear growth up to 70%, after this infill density, a sort of plateau is shown, in fact the compressive strength-to-weight ratio becomes almost constant (the linear fit of this part of the curve has a very small negative slope which could be approximated to zero). Therefore, given the printing conditions reported in this work, the 70% of infill density optimizes the compressive strength-to-weight ratio, minimizing the manufacturing time and material use.

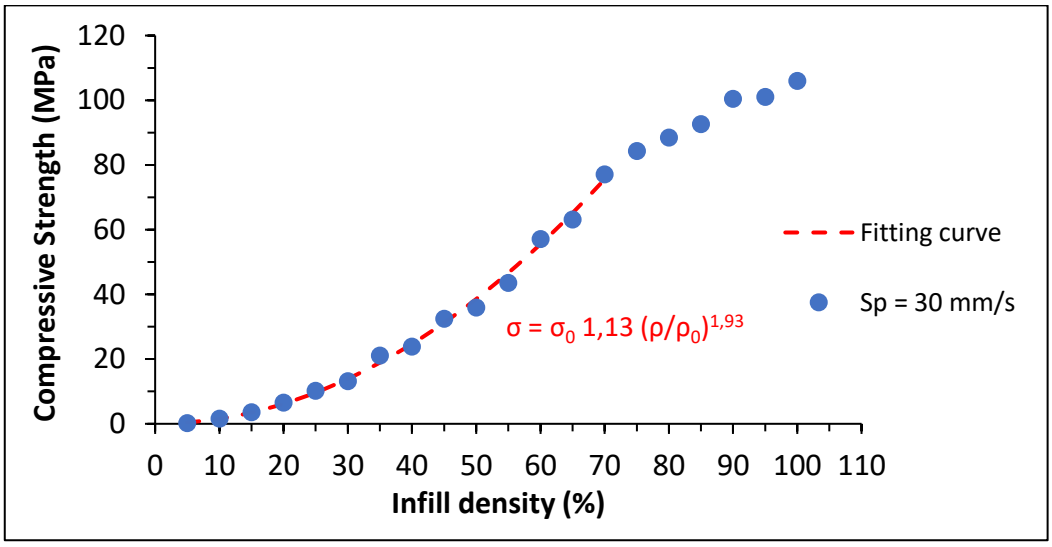

Figure 6.6: Compressive Strength behaviour from 5% to 100% of infill density.

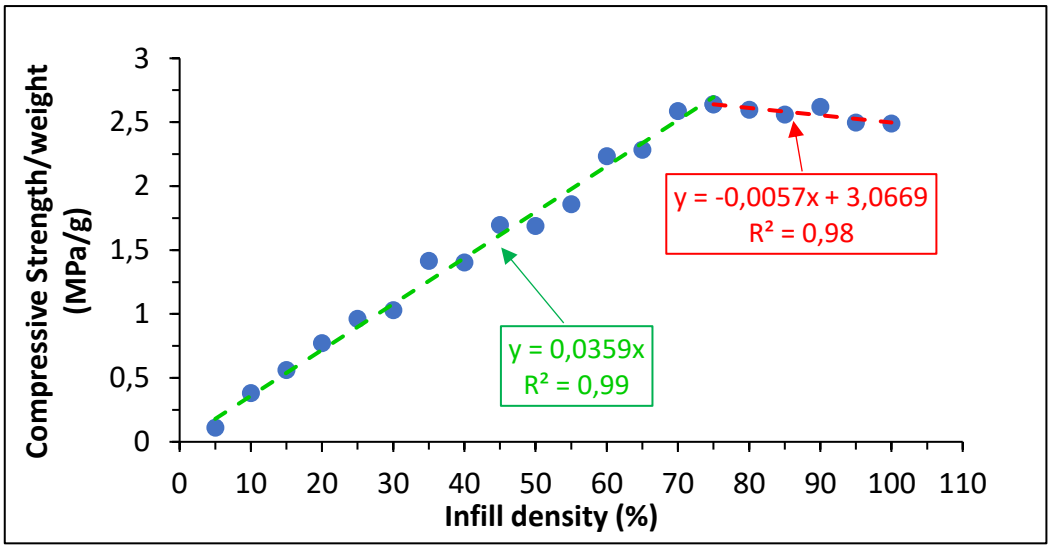

Figure 6.7: Compressive Strength-to-weinght ratio from 5% to 100% of infill density.

In order to better understand the failure mechanisms of the specimens under compression, OM analysis were carried out.
Figure 6.8 displays a picture of the five observed samples and the microscope images corresponding to the highlighted failed regions (a-f). The OM images show that:

- At lower infill densities, 5% and 10%, the gyroidal cells were subject to uniform breakage of the lattice structure. In Figure 6.8 a-c is shown that crack propagation occurred vertically indicating that filament fracture due to bending stresses was the actual cause of failure, rather than inter-layer delamination resulting from the FFF process;

- At 15% the printed layers underwent shear deformation due to stretching stresses and therefore delamination and breakage occurred (Figure 6.8 d);

- The densest specimens (15% – 25%) showed buckling: the unit cells deformed for both stretching and bending stresses, without breaking, exhibiting very slight delamination (Figure 6.8 e and f). The latter decreases as the filling percentage increases until it disappears completely for samples printed at infill densities higher than 25%. This is due to the fact that by increasing the filling % the unit cell size decreases, thus the adjacent cells cool more slowly and the temperature of the printed layer remains higher for a long time, improving the wettability. Therefore, the interlayer adhesion between successive layers is improved and delamination is prevented.

To summarize, the phenomena that lead to the breakage of the samples subjected to compression stresses are two: the first depends on the geometry of the cells, in particular on their size, the second depends on a limitation of the FFF manufacturing process linked to poor interlayer adhesion. Both phenomena decrease as infill density increases. At lower densities, the unit cells are bigger, thus, because of the lack of support elements, the overhang and curling phenomena are introduced during the printing process [120].

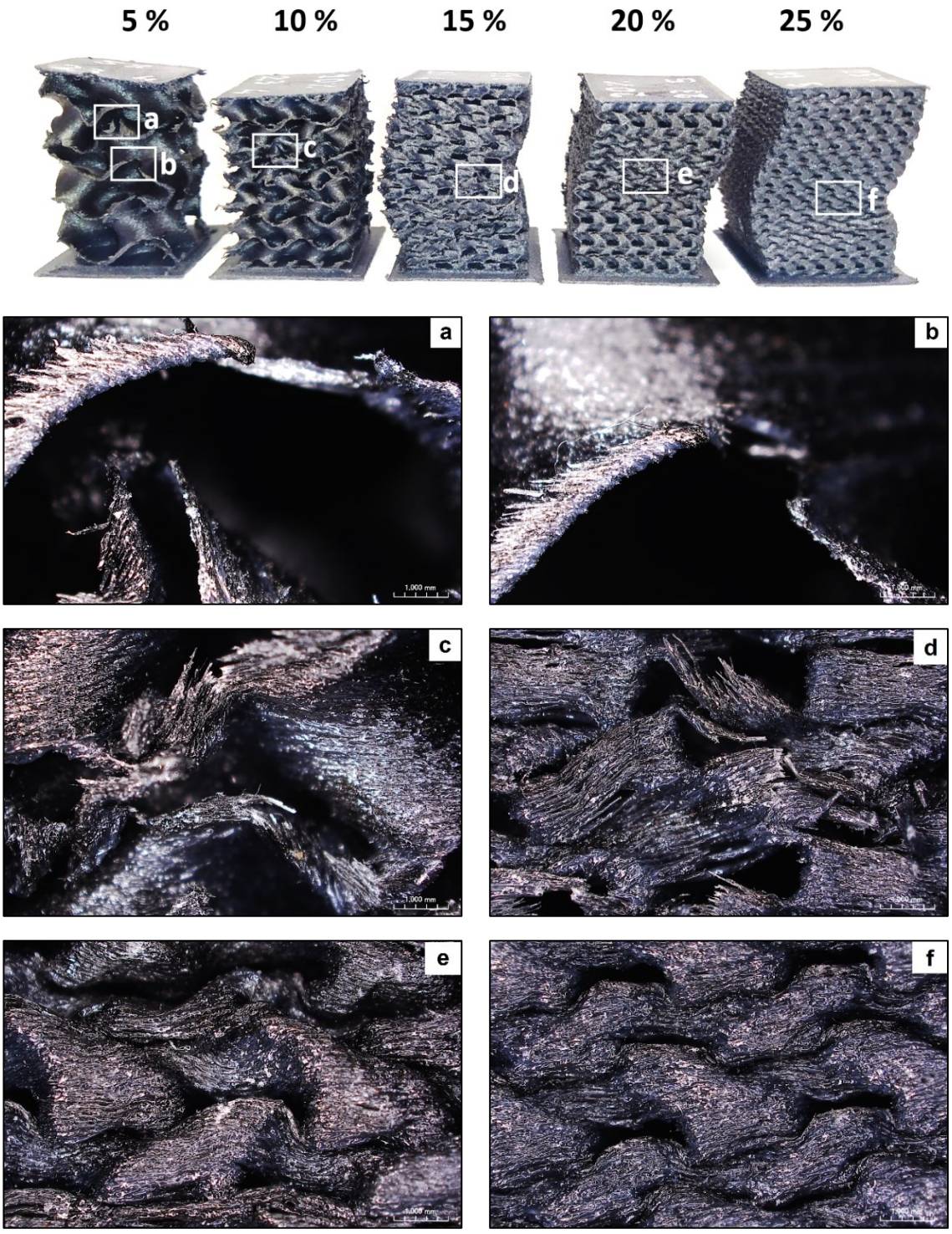

Figure 6.8: Optical microscope images (a-f) of the failed regions in the corresponding samples.

Ultimately, the results showed that, given the process parameters of Table 6.1, the FFF process was robust since the compressive strength standard deviations were about 5%. When the infill densities from 5% to 25% were considered, the compressive strength exhibited a power law growth and the printing speed had a very slight influence on it, in fact the mechanical performances are improved as the speed decreases, but this improvement is almost negligible falling within the standard error. For this reason, with a view to reducing production time, it was decided to continue the study up to the 100% of infill density only for the printing speed of 30 mm/s. The main aim was to maximize the compressive strength-to-weight ratio, i.e. to find the infill density that optimize the compressive strength and minimize both material use and process time. It was found that, until the 70% of infill density, the compressive strength exhibited the previously defined power law growth (Figure 6.6). Due to that, it is possible to predict, in good approximation, the compressive strength of printed parts with a value of infill density inside this range. For densities higher than 70% the compressive strength increased thanks to the densification of the cells in the lattice, but with a change in curvature which no longer followed the power law trend. By plotting the compressive strength-to-weight ratio versus the infill density it was found that, after a linear growt, the data relative to samples denser than 70% showed a plateau. This result means that the 70% is the optimal density sought. In summary, in this work, it was demonstrated that the Carbon PEEK gyroid lattice structures are very promising for the light-weight purposes and for applications in which the compressive loads are involved. It could be very interesting for the aeronautical industry because it is a quasi-isotropic structure and could allow a weight reduction of at least 30%, if C-PEEK is considered as fabrication material, and greater than 30% if this lattice structure is used for replacing metal parts.

6.2 Evaluation of the mechanical isotropy in compression of gyroid structures

Fused Filament Fabrication (FFF) technology tends to exhibit anisotropy along the print direction (z direction). Gyroid structures are characterized by their uniform cell arrangement in the three dimensions, typically exhibiting more isotropic mechanical properties compared to other trabecular structures used for structural lightening. However, the mechanical performances of gyroids are affected by the material isotropic or anisotropic nature, the cell design (such as cell size and wall thickness), and manufacturing. Consequently, it was decided to investigate the possibility that gyroid structures can be tailored to mitigate the mechanical anisotropy of 3D printed parts. For this purpose, after the preliminary study on the compression behavior of gyroid structures at different densities (tested along z, the direction of growth of the part) shown in the previous paragraphs, it was decided to extend the study also along the x and y directions. Since the capability to produce isotropic components is crucial in overcoming the limitations of FFF process, the present research demonstrates how infill percentage, i.e. the size of the unit cells, affects the compressive behavior of 3D printed Carbon fiber-reinforced Polyether(ether ketone) in all directions, with a focus on the possibility to reduce the anisotropic behavior along the printing direction (z axis).

6.2.1 Design of Experiment

Despite being a composite with chopped fibers uniformly distributed within the matrix, C-PEEK typically exhibits anisotropic behavior due to fiber alignment along the extrusion direction (Figure 6.9). Therefore, the study focuses on how gyroid structures, by varying infill densities, can mitigate the mechanical anisotropy in 3D printed parts, which arises from both the material characteristics and the FFF process itself.

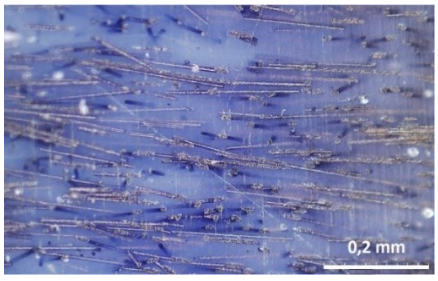

Figure 6.9: Optical Microscope image of C-PEEK carbon fibers aligned along the extrusion direction.

Roboze C-PEEK was used as feed material for the Roboze One+400 3D printer. The Ultimaker Cura 5.2.1 slicing software was used to generate G-codes.

All the main printing parameters are listed in Table 6.4.

Process Parameters	
Nozzle diameter	0,4 mm
Bed temperature	150 °C
Nozzle temperature	450°C
Printing speed	23 mm/s
Walls number	0
Layer thickness	0,1 mm
Infill densities	5%,10%,15%,20%,25%,40%,55% ,70%
Infill pattern	Gyroid

Table 6.4: Printing parameters.

In order to test the samples in the x,y,z directions it was decided to change the shape of the specimens shown in the previous chapter with a cubic shape without walls and top/bottom layers in order to test only the mechanical performance of the gyroid structure. Cubes with a side length of 25 mm were 3D printed and, before being detached from the building bed, the x and y axes relating to the printing volume were marked on paper tape subsequently attached to the upper surface of the specimen. In this way it was possible to perform compression tests in the x,y,z directions simply rotating the cubes so that the x, y or z axis aligns with the load direction of the test machine.
The compression test setup and the specimens shape are shown in Figure 6.10.

a) b)

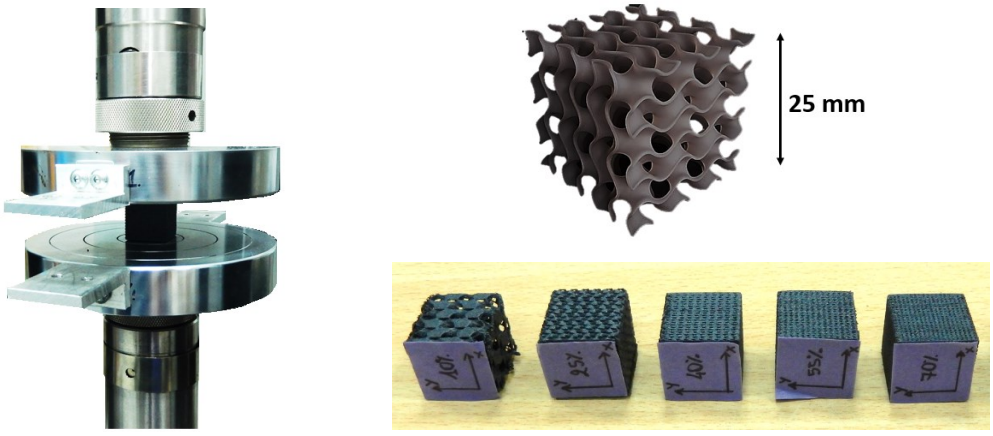

Figure 6.10: Compression test setup (a) and the specimens shape (b).

In particular, 3 samples for each direction and for each infill density were tested. Specimens with infill densities of 5%, 10%, 15%, 20%, 25%, 40%, 55% and 70% were printed. The infill densities (%) were indicated on the paper tape as well.
Compression tests were performed according to the ASTM C365 standard (minimum specimen area: 625 mm^2; standard environmental conditions) with a test speed of 1,3 mm/min.

From the stress-strain curves, the compressive strength at yield was obtained and the Young's modulus was calculated for each sample. To interpret the compressive behavior of 3D printed C-PEEK gyroid structures and evaluate their isotropy, nonlinear regression analysis on relative compressive strength (σ/σ_0) and relative Young's modulus (E/E_0) versus the relative density (ρ/ρ_0) was performed to find the C1, C2, m, n parameters which satisfy the Gibson-Ashby model (see Eq. 1 and Eq. 2, respectively).

6.2.2 Results and Discussion

The specimens after compression test and representative stress-strain curves are displayed in Figure 6.11. What is noteworthy is that all stress-strain curves follow the characteristic trend for Bending-dominated structures with an initial elastic phase, followed by a constant plateau and a final growth in stress due to densification of the unitary cells.

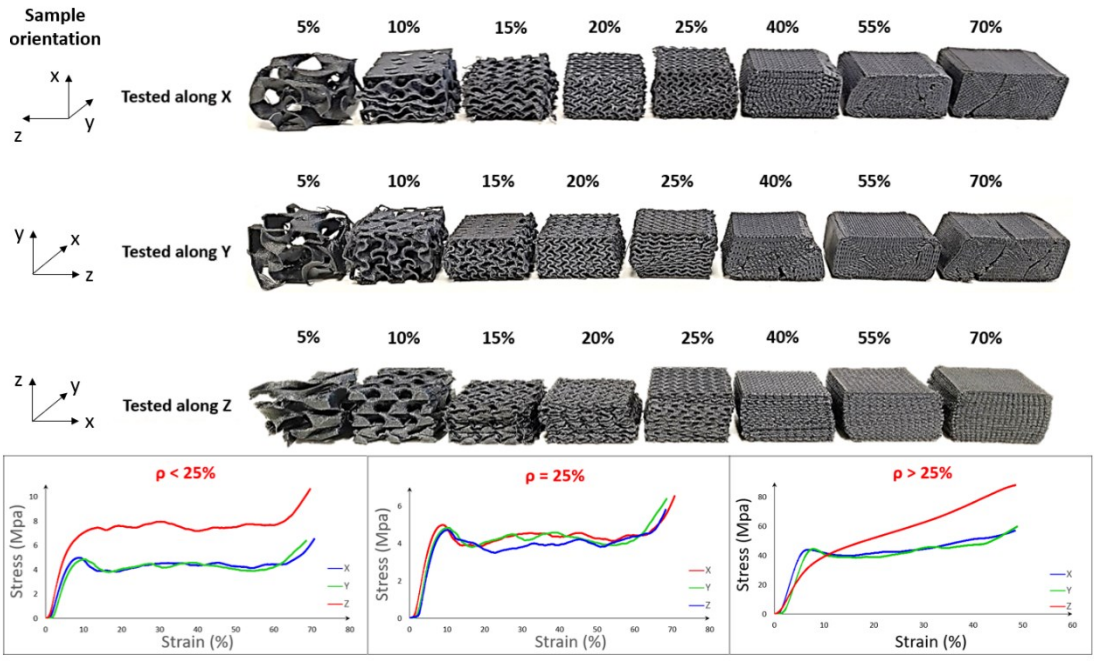

Figure 6.11: Pics of the specimens after compression test and representative stress-strain curves.

From the comparison of stress-strain curves and the images of tested samples, the following conclusions can be drawn:

- Up to the 25% of infill density the compressive behavior along the three tested axes was the same: the structures broke mainly due to the bending of the surfaces during compression. In particular, the isotropy was perfectly confirmed in all direction for ρ equal to 25% thanks to the perfect balance between the stresses to be supported (both bending and stretching stresses) and the dimensions of the cells within the structure.

- All the specimens tested, showed uniform compression of the unitary cells and the failure of the structures occurred along shear bands resulting from the bending of the surfaces and buckling phenomena. However, the presence of shear bands decreased by increasing the infill density beyond 25%. This happened because the cell size decreases by increasing the density, therefore when they deform they immediately come into contact with each other, avoiding sliding phenomena.

- When $\rho<25\%$ the isotropy is confirmed only in the x and y directions, overall with a loss of strength of approximately 40% if compared to the z direction results. The reason why the structures tested along the x and y directions recorded lower values of compressive stress is attributable to delamination phenomena along the z direction caused by the bending of the load-bearing elements.

- For densities higher than 25%, the isotropic behavior is confirmed in x and y only. In fact, the structures tested along the x and y axes exhibited a failure because of the appearance of vertical cracks which did not appear in samples tested along the z axis. This happened because the buckling of the structures during the test induced a loss of interlayer adhesion between layers deposited along z, resulting from the FFF process. The samples tested along z showed a shorter elastic phase: after yielding the unit cells deform plastically, compacting in a continuous and uniform manner.

All the average compression test results and standard deviations are reported in Table 6.5, while all the derived relationships and the minimized sum of squared errors are reported in Table 6.6. All the data and the fitting curves are displayed in Figure 6.12.

Test direction	Infill density (%)	Compressive strength (MPa)	Standard deviation (MPa)	Young's Modulus (MPa)	Standard deviation (MPa)
X	5	0,38	± 0,03	0,39	± 0,04
	10	1,59	± 0,19	1,63	± 0,49
	15	3,71	± 0,31	3,23	± 0,45
	20	4,73	± 0,24	4,03	± 0,11
	25	10,62	± 0,35	8,20	± 1,06
	40	26,43	± 1,45	21,34	± 1,42
	55	43,80	± 0,62	38,55	± 2,09
	70	67,73	± 1,19	52,03	± 2,68
Y	5	0,43	± 0,03	0,45	± 0,03
	10	1,61	± 0,20	2,00	± 0,48
	15	3,62	± 0,34	3,08	± 0,51
	20	4,72	± 0,19	4,00	± 0,06
	25	10,38	± 0,23	9,90	± 1,04
	40	25,42	± 1,24	20,40	± 1,41
	55	44,45	± 0,70	38,70	± 1,68
	70	69,09	± 1,56	52,31	± 1,79
Z	5	0,73	± 0,04	1,02	± 0,08
	10	2,98	± 0,39	3,23	± 0,25
	15	5,84	± 0,15	4,53	± 0,13
	20	7,35	± 0,10	5,27	± 0,12
	25	10,92	± 0,76	7,93	± 0,54
	40	22,77	± 0,46	16,77	± 1,19
	55	28,36	± 2,01	26,10	± 0,91
	70	56,42	± 2,80	40,00	± 1,88

Table 6.5: Compression test results.

Test direction	Mechanical Property	Derived Relationship	SSE
X	Compressive strength	$\frac{\sigma_x}{\sigma_0} = 0{,}97 \left(\frac{\rho}{\rho_0}\right)^{1{,}84}$	1,8 10^{-4}
	Young's Modulus	$\frac{E_x}{E_0} = 0{,}1 \left(\frac{\rho}{\rho_0}\right)^{1{,}71}$	6,59 10^{-6}
Y	Compressive strength	$\frac{\sigma_y}{\sigma_0} = 1{,}02 \left(\frac{\rho}{\rho_0}\right)^{1{,}89}$	1,06 10^{-4}
	Young's Modulus	$\frac{E_y}{E_0} = 0{,}09 \left(\frac{\rho}{\rho_0}\right)^{1{,}7}$	6,26 10^{-6}
Z	Compressive strength	$\frac{\sigma_z}{\sigma_0} = 0{,}66 \left(\frac{\rho}{\rho_0}\right)^{1{,}65}$	1,45 10^{-3}
	Young's Modulus	$\frac{E_z}{E_0} = 0{,}06 \left(\frac{\rho}{\rho_0}\right)^{1{,}54}$	1,45 10^{-6}

Table 6.6: Nonlinear regression results.

From the nonlinear regression results, it could be noted that all the data followed a power-law trend, with exponents higher than 1,5. This suggest that the gyroid structures haven't a stretching-dominated behavior, but they exhibit a non-ideal bending dominated behavior. This non-ideal behavior is probably linked to the structural imperfections caused by the FFF technology, which cause delamination and sliding phenomena due to the lack of inter-layer adhesion. However, this aspect could be improved by varying the process parameters that most influence the wettability between subsequent layers, such as nozzle temperature and printing speed, without being able to further reduce the layer height.

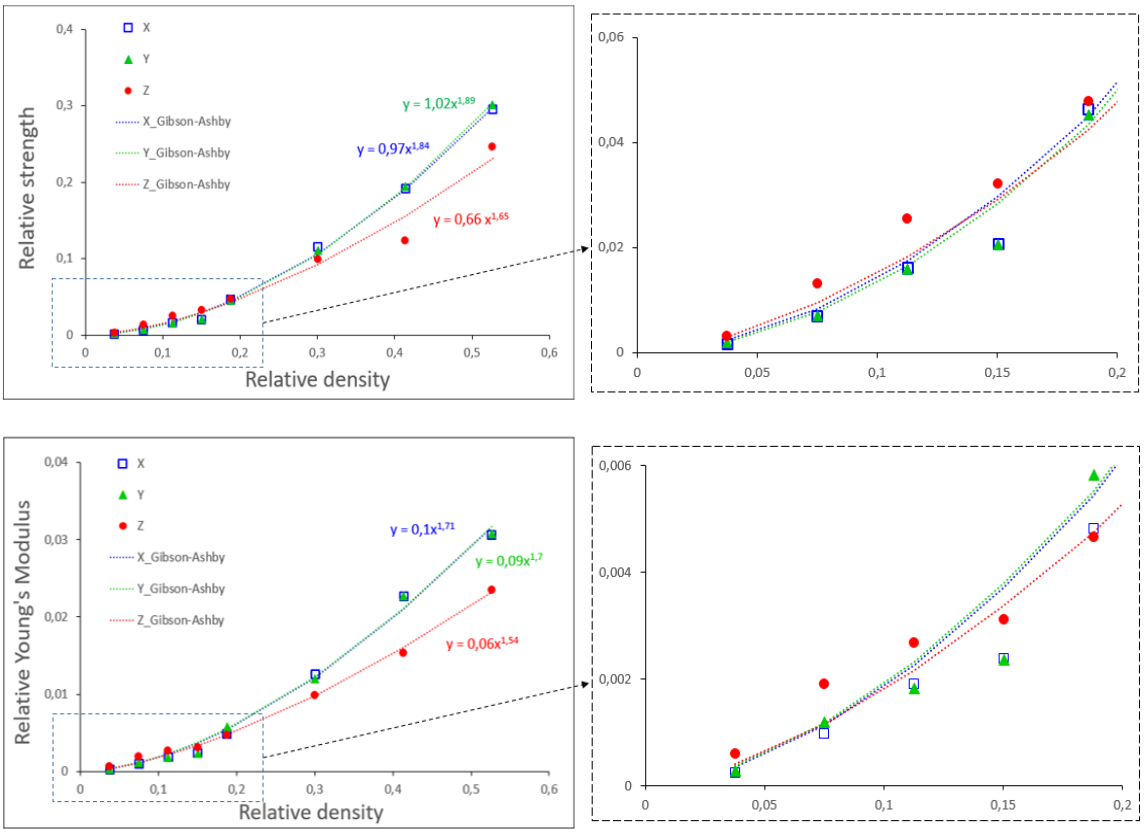

Figure 6.12: Relative strength (σ/σ_0) and Relative modulus (E/E_0) versus relative density (ρ/ρ_0) plots.

The results showed that the FFF process was robust in fact, in most cases, both the compressive strength and Young's Modulus standard deviations were less than 5%. It was found that both the Compressive Strength and Young's Modulus follow a power-law trend as the Gibson-Ashby predictions for bending-dominated structures. Through nonlinear regression and the least squares method, it was possible to obtain the coefficients (*C1* and *C2*) and exponents (*m* and *n*) of Eq. 1 and Eq. 2 of the Gibson-Ashby model. Therefore, it is possible to predict, in good approximation, the compressive strength of printed parts with a value of infill density inside the considered range.

In the present work the isotropy of the compressive behavior of 3D printed Carbon PEEK gyroid lattice structures was evaluated by considering the variation in infill density, i.e. in cell size. The isotropy of the structures was perfectly confirmed in all direction only for ρ equal to 25% thanks to the perfect balance between the stresses to be supported and the dimensions of the unitary cells. For densities below and above 25% isotropy was only found along the x and y directions due to the loss of adhesion between layers along the printing direction (z). In particular, for ρ<25% the delamination occurred due to the

bending of the struts; for $\rho>25\%$ the loss in interlayer adhesion was induced by the buckling of the structures.

In summary, it was demonstrated that it is possible to mitigate the anisotropy of FFF-printed parts (and also of the material) by choosing the infill density that can best support the loads and the process parameters that can improve interlayer adhesion as much as possible. In this way, the Carbon PEEK gyroid lattice structures are very promising for the light-weight purposes and for applications in which the compressive loads are involved.

6.3 Impact behavior and residual strength of 3D printed C-PEEK sandwich panels

The aim of this part of the research was to study the impact behavior of 3D printed C-PEEK sandwich panels having two solid skins and a trabecular core made with a gyroid infill. In particular, the main objective was to evaluate how the impact energy absorption capability of the panel varies as the infill density of the gyroid core varies. The two infill densities tested are 10% and 20%. The reasons why these two infill densities were chosen are:

- They fall in the range in which, according to the results shown previously, the gyroid allows a certain isotropy in compression (see Paragraph 6.2).
- The number of complete unit cells repeated within the core thickness: two for the 10% and four for the 20% (see Figure 6.13). In this way, the comparison between the results obtained for cells of such different sizes, one twice the other, allows to better evaluate the influence of the gyroid core on impact resistance of panels with the same skin construction.
- The cells dimension. The dimensions of the unit cell in both structures, in addition to allowing a notable reduction in the weight of the panel compared to a 100% solid block, allows the solid flat surfaces of the upper skins to be supported, guaranteeing good printing at the core-skin interface. In fact, this is not guaranteed for infills with a density of less than 10% where the size of the cells of the gyroid structure is not sufficient to support the subsequent solid layers which therefore collapse, creating defects especially at the core-skin interface. In those conditions, the gyroid core would not be able to adequately distribute and absorb the impact loads received on the skin.

10%	
20%	

Figure 6.13: Side view of the 3D printed sandwich panels.

6.3.1 Design of Experiment

The sandwich panels with a gyroid-lattice core, were 3D printed using the Roboze One+400 and Roboze C-PEEK filament as feeding material because, thanks to the presence of 10% of chopped carbon fibers, it guarantees less shrinkage of the material and better extrudability in unheated chamber conditions. To facilitate the detachment of the panel from the printing surface without damaging the lower solid skin, a support was printed with the same C-PEEK filament which was subsequently removed by CNC machining. The 3D printing process parameters for both support and specimen are listed in Table 6.7.

The test method followed the ASTM D7136 standard for measuring the damage resistance of a fiber-reinforced polymer matrix composite to a drop-weight impact event. The sample dimensions were 150 mm x 100 mm x 15 mm with 2 mm thick skins and 11mm thick core. Figure 6.14 shows a schematic representation of the sample shape and dimensions. For both gyroid infill densities, a set of six specimens was produced. The impact energy for the two sets of specimens was different and was chosen by carrying out several tests on a sacrificial specimen for each set, until the "Barely Visible Impact Damage" (BVID) conditions were reached.

After the test, non-destructive inspections (NDI) were carried out as follows:

- the indentation of the impact mark was evaluated using a Mitutoyo Absolute comparator (with resolution of 0.01 mm);
- the extent of damage was evaluated and measured using an Epson Perfection V750 PRO scanner;
- ultrasound inspection was used to verify how the damage spread throughout the inside the panel.

Finally, the Compression After Impact test (CAI) was carried out, using the MTS Insight testing machine, to evaluate the residual resistance of the panel according to the ASTM D7137 standard procedure.

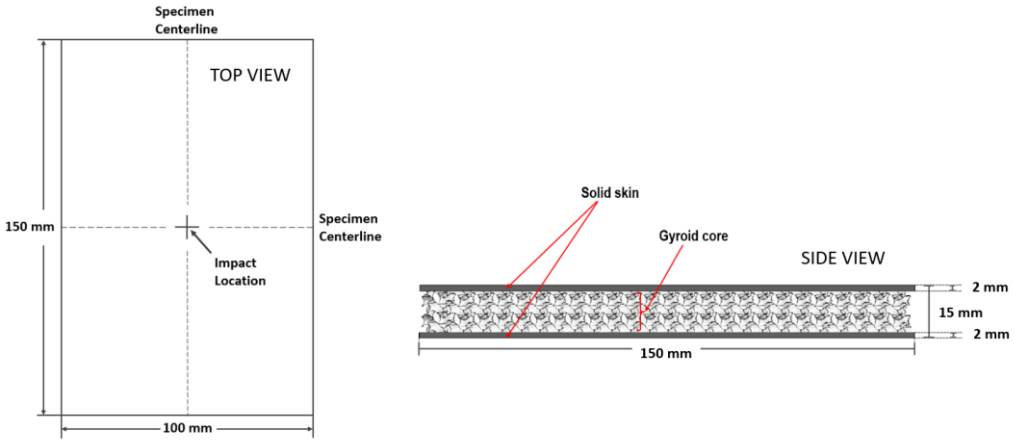

Figure 6.14: Schematic representation of the sandwich structure of the panel: top view (left) and side view (right).

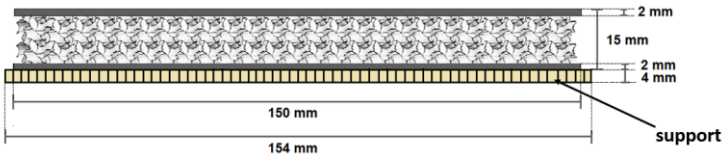

Support		Specimen	
Print speed	30 mm/s	Print speed	26 mm/s
Infill pattern	Zig-zag	Infill pattern	Gyroid
Infill density	15%	Infill density	10% and 20%
Top layers	4	Top thickness	2 mm
Bottom layers	4	Bottom thickness	2 mm
Top/bottom infill pattern	Lines [45, -45]	Top/bottom infill pattern	Lines [45, -45]
Layer height	0,1 mm	Layer height	0,1 mm

Table 6.7: FFF process parameters for both supports and specimens.

6.3.2 Results and Discussion

Low-velocity impact test

The study of the behavior of sandwich panels in low-velocity impact (LVI) conditions was conducted with the drop-weight method according to ASTM D7136 standard. For the impact test was used a machine equipped with a free fall weight: the flat panel is appropriately clamped along the edges to prevent any slippage during the experiment and is hit by an impactor of defined geometry and mass which falls from a given height. In Figure 6.15 a photo of the used system is shown. The impact device used was an Instron Ceast 9350 with an impactor mass of 5,28 kg. For the two set of specimens the impact energy was chosen after various tests on a sacrificial specimen until the BVID conditions were reached. It must be specified that the choice of sacrificial specimens was done after ultrasonic scans in order to use, for this purpose, the samples that had given a worse response and which already had manufacturing defects. The experimental conditions for both groups of specimens are collected in Table 6.8.

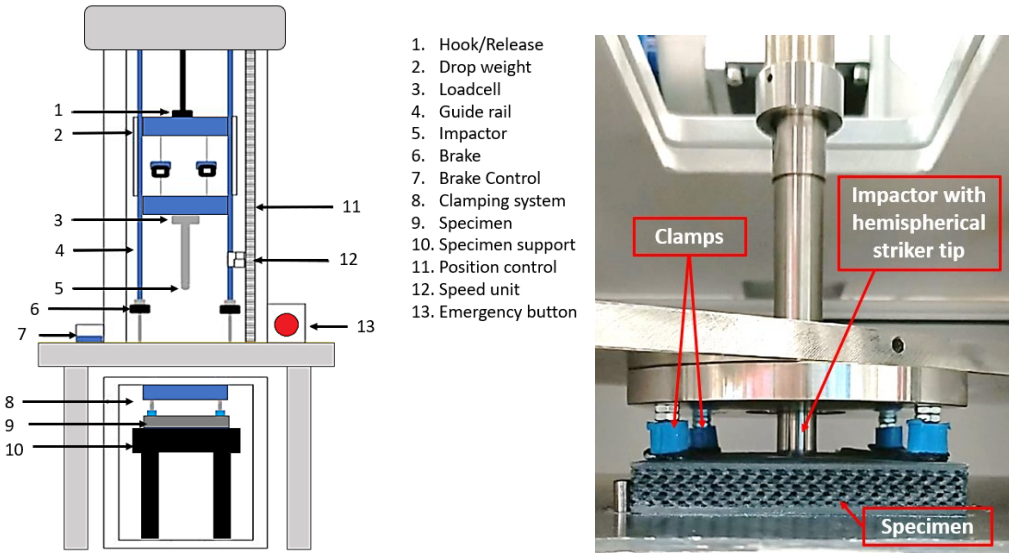

Figure 6.15: Schematic representation of the impact device and a photo of the specimen support and clamping.

	10% dense gyroid	20% dense gyroid
Impact Energy	4 J	6,5 J
Drop height	77,6 mm	126 mm
Mass of the impactor	5,277 Kg	5,277 Kg
Impact speed	1,23 m/s	1,57 m/s

Table 6.8: Impact test conditions.

The history of the collision is reconstructed through the force-time curve, which allows to obtain the maximum energy corresponding to the maximum impact force. In Figure 6.16 all the force-time curves are shown, while the experimental results are reported in Table 6.9.

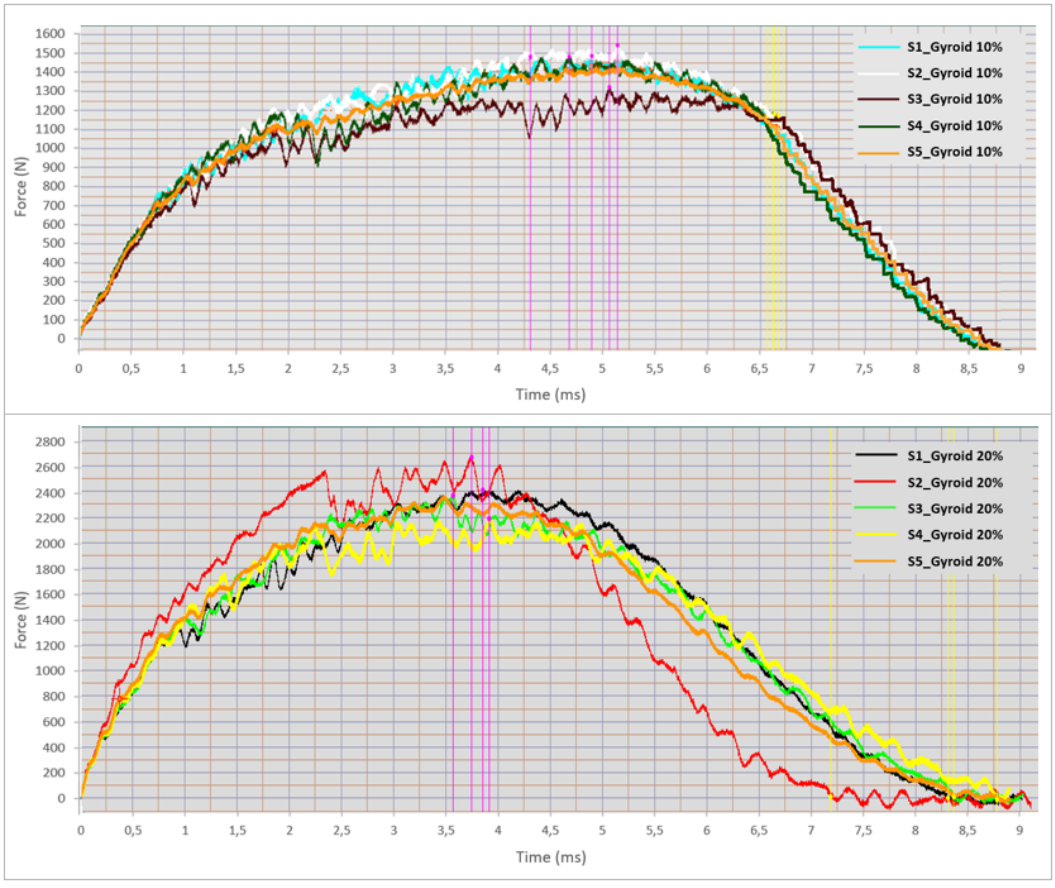

Figure 6.16: Impact Force vs Time curves for both sets of specimens.

Sample ID	F_{max} (N)	t_{max} (ms)	E_{max} (J)	$E_{average}$ (J)	St. dev. (J)
S1_Gyroid 10%	1485,61	4,89	3,55		
S2_Gyroid 10%	1542,54	5,13	3,59		
S3_Gyroid 10%	1322,95	5,06	3,36	3,49	±0,08
S4_Gyroid 10%	1483,89	4,31	3,50		
S5_Gyroid 10%	1481,91	4,68	3,44		
S1_Gyroid 20%	2673,02	2,89	5,30		
S2_Gyroid 20%	2407,34	3,86	5,86		
S3_Gyroid 20%	2662,17	3,75	6,04	5,74	±0,25
S4_Gyroid 20%	2369,39	3,57	5,65		
S5_Gyroid 20%	2185,04	3,92	5,84		

Table 6.9: Impact test results.

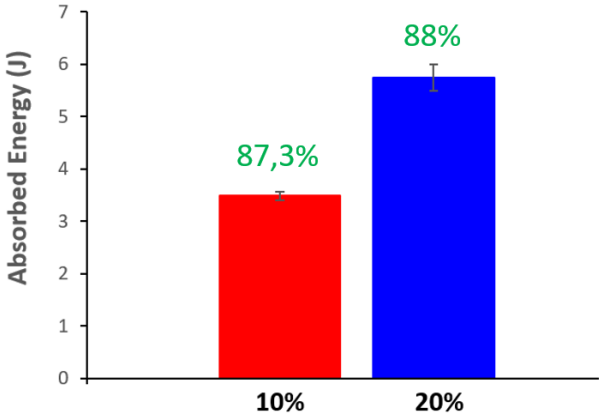

Figure 6.17: Average absorbed energy.

In this section, the force-time and energy absorption capability of the 3D printed gyroid-core sandwich panels were discussed. In particular, the effects of unit cell dimensions on energy absorption capabilities were studied. It must be noted that the two types of structures with different infill densities, respond differently to the impact both in terms of impact energy in BVID conditions and in terms of the time necessary to reach the maximum absorbed energy (Emax). Specifically, the specimens with the 10% core density underwent impacts with an impact energy of 4 J and reached Emax after approximately 5 ms. On the other hand, the specimens with the 20% core density suffered impacts with an impact energy of 6,5 J and reached Emax faster, after approximately 3,6 ms. Furthermore, after the peak force, a more rapid load drop is observed in the case of

the 20%-dense core as compared to the 10%-dense core. However, the percentage of absorbed energy compared to the provided impact energy was 87,3% for the 10%-dense core and 88% for the 20%-dense core with standard deviations in both cases lower than 5%. After the drop-weight test, all structures showed permanent damage visible to the naked eye only on the skin subjected to impact while the opposite skin was intact. The damage was studied using indentation measurements, damage dimensions, ultrasonic NDI to evaluate the damage propagation within the specimen and CAI tests. All results are reported and discussed below.

Non-destructive inspections

For aeronautical applications the impact behavior of the material is of particular interest in relation to its *indentation*. The imprint left by the blunt object is the first sign of the impact visible to the naked eye, and therefore allows to perceive a situation potentially critical by simple visual examination. Obviously, the surface alteration must be sufficient evident: from this need was born the definition of *"Barely Visible Impact Damage" (BVID)*, which generally links the concept of visibility to the depth of the indentation. In the aeronautical sector the concept of BVID refers to the measurement of the maximum depth of the impact mark (i.e. the indentation) which must be less than 1mm. In these conditions, all the imprints left by the impactor were analyzed measuring both the indentations and extent (in terms of diameters) by using a Mitutoyo Absolute comparator (with a resolution of 0.01 mm) and an Epson Perfection V750 PRO scanner, respectively. All the diameter and indentation measures are reported in Table 6.10 and, in Figure 6.18, pictures of the comparator setup and damage extent measurement are shown. The damage pattern found on the samples was a circle with a cross in the center. It resulted very similar to that reported in the ASTM D7136 standard (see Figure 6.18 a), according to which large cracks are formed combined with fiber breakage, but, in this case, since it is a FFF printed sample, it can only be a case of breakage of the extruded filaments which have a similar behavior to the fibers inside a composite material.

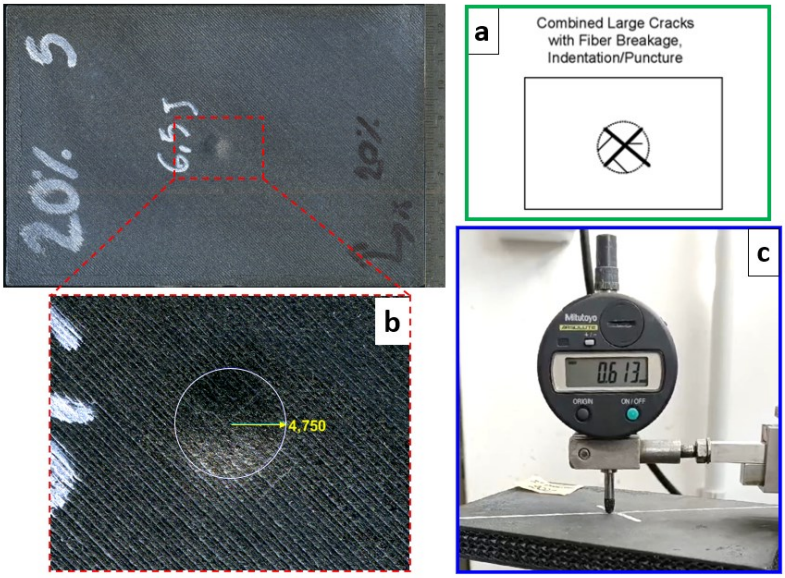

Figure 6.18: Damage Mode according to ASTM D7136 (a); damage extent measurements of the impacted sample: radius (b) and indentation (c).

Sample ID	I (mm)	$I_{average}$ (mm)	St. dev. (mm)	d (mm)	$d_{average}$ (mm)	St. dev. (mm)
S1_Gyroid 10%	0,323			7,01		
S2_Gyroid 10%	0,329			6,79		
S3_Gyroid 10%	0,304	0,31	± 0,01	7,19	6,98	±0,13
S4_Gyroid 10%	0,302			6,89		
S5_Gyroid 10%	0,299			7,02		
S1_Gyroid 20%	0,874			10,98		
S2_Gyroid 20%	0,861			10,41		
S3_Gyroid 20%	0,878	0,86	±0,02	10,78	10,44	±0,52
S4_Gyroid 20%	0,844			10,53		
S5_Gyroid 20%	0,837			9,50		

Table 6.10: Damage extent measurements in terms of indentations (I) and diameters (d).

From Table 6.10 it could be noted that the 10%-dense structures impacted with an energy of 4 J had a smaller damage in terms of both indentation and diameters if compared to the 20%-dense structures impacted with an energy of 6,5 J. In particular, the average indentation and the average diameter were about 64% and 33% lower, respectively. Obviously, this is due to both the difference in energy used for the test and to the difference in response of the two structures with different gyroid densities.

Generally, the failure mechanisms due to impact event in a 3D printed facesheet could essentially be intralayer cracks and interlayer delamination. A campaign of *ultrasonic inspections* was carried out aimed at identifying the evolution of the damage within the impacted panel. A fundamental problem that arises in ultrasonic non-destructive testing is represented by the need to guarantee adequate and constant probe-sample acoustic coupling because the flow of ultrasonic energy in emission and reception is transmitted through it. For this reason, the squirter-based inspection system was used: the ultrasounds are transmitted through a column of water which acts as a coupling agent, wetting the sample. In this way, the ultrasounds are initially transmitted into the water and, after having traveled in it, reach the liquid-sample interface. Figure 6.19 shows a representative image of the operation of the squirter-based ultrasonic testing system: the oscilloscope shows an initial peak relating to the emission of the transducer followed by a second peak relating to the transmission of the signal through the sample. Attenuation of the signal could appear corresponding to the interfaces of defects (having a different acoustic impedance). This procedure has the following advantages:

- The coupling between probe and sample is constant and uniform, guaranteeing uniform sensitivity and stability to the signal
- Pieces even with complex geometry can be tested
- Automated inspection systems can be used.

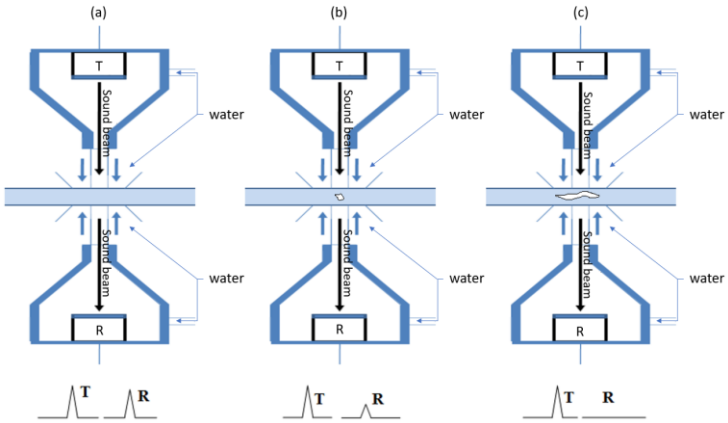

Figure 6.19: Schematic representation of squirter-based ultrasonic system: no defect to be detected (a), small defect (b), big defect (c).

The ultrasound scans were performed in transmission configuration. In this configuration, the ultrasonic signal generated by the emitter passes through the entire thickness of the sample and reaches the receiver. Of course, if the signal meets along its path a

discontinuity, this will reflect part of the energy and the amount of energy that will therefore reach the receiver will be less. In this case, since the samples were not closed by external walls in the central part constituted by the gyroid structure, before testing, they were covered along the perimeter with adhesive tape, to prevent water from entering inside the porosities. The scans were carried out both before the impact in order to identify the test parameters for each sample (signal frequency and intensity) to be used for post-impact scans and verify whether there were defects in the structure, and after the impact test to verify how the impact damage was propagated within the samples. All the results before and after impact are shown in Figure 6.20. The frequency chosen for the inspection of samples at 10% of gyroid density is 2,25 MHz, while for samples at 20% of density it is 1 MHz. From Figure 6.20 it could be noted that the samples named with number "6" for each set, gave very low signals during ultrasound scans, thus they were used as sacrificial specimens to define the impact conditions. Furthermore, it is very evident the difference in the propagation of the impact damage within the sample for the two different sets of specimens. Specifically, samples number 2, 4 and 5 with 20% of gyroid density showed a clear detachment of the upper skin from the trabecular core involving the 40%-60% of the total skin area, whereas samples 1 and 3 showed more localized damage, involving only the 1,7% of the total skin area, with a shape very similar to the mark left by the impactor, visible on the external skin. Post-impact scans of the 10% dense samples showed a generally lower extent of damage than the 20% samples, with localized damage for samples 1, 4 and 5, involving only the 0,3%-0,5% of the total area, somewhat more extensive for samples 2 (2,2% of the sample area), with a detachment of the skin from the gyroid core more evident in sample 3, involving the 7,5% of the total sample area. From these results, the following hypothesis regarding the prevailing damage mechanisms for both types of sandwiches panels could be done:

- For the samples at 10% of core density (tested with an impact energy of 4J), there was the onset of intralayer localized cracks within the impacted facesheet, probably because of a localized failure of the underlying gyroid structure due to vertical cracks and deformations.
- For the samples at 20% of core density (tested with an energy of 6,5J), interlayer delamination/detachment of the impacted skins from the core occurred, probably due to a more extensive propagation of stresses between the adjacent unit cells following the deformation caused by the impact.

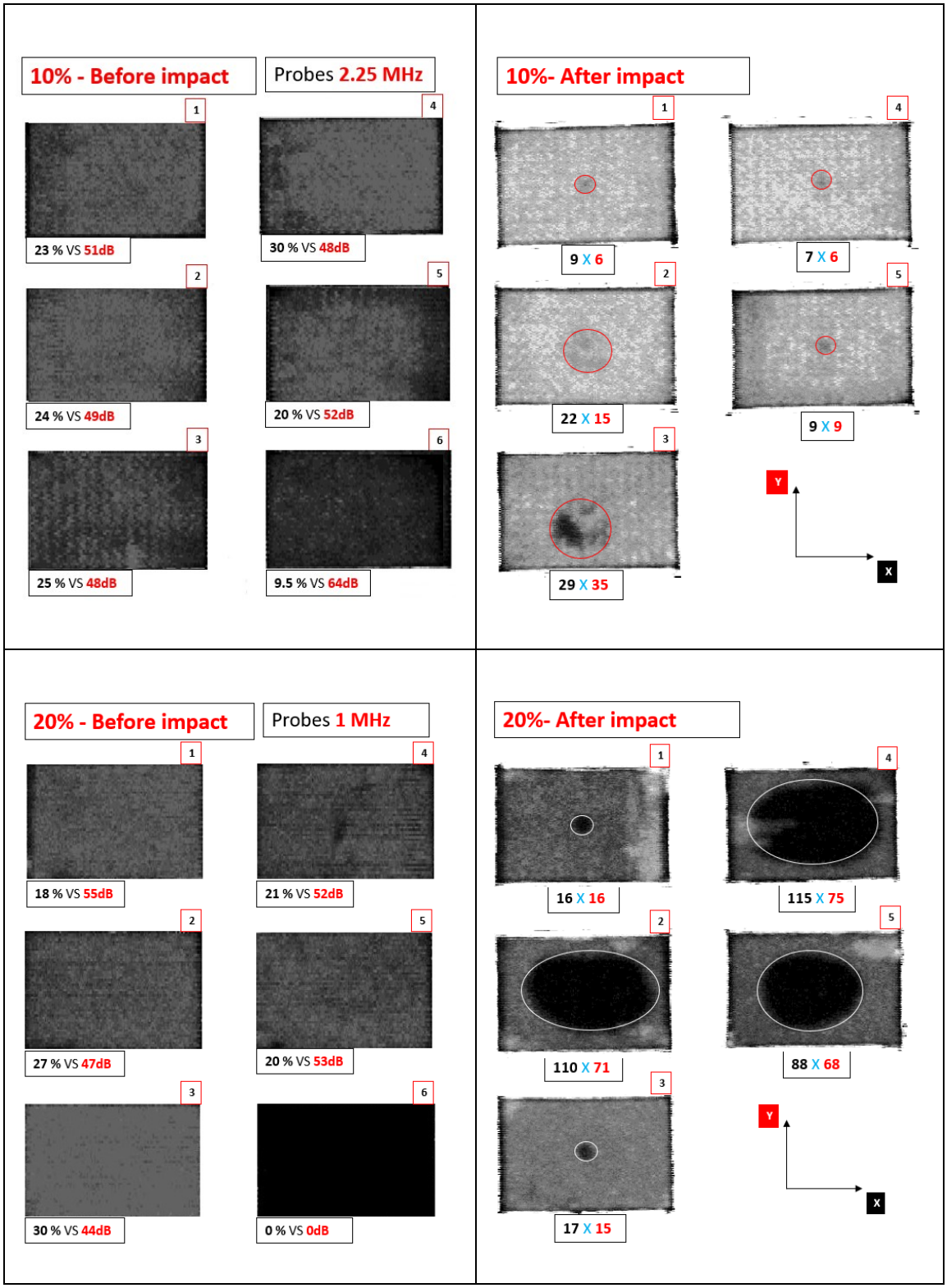

Figure 6.20: Ultrasonic C-scans of all samples before (left) and after (right) impact test.

Compression After Impact test

After having pre-damaged the specimen in the drop-weight impact event, evaluating the damage by measuring the deformation at the point of impact and determining the extent of the damage inside the samples using non-destructive ultrasonic inspections, static compression test for determining the residual compressive strength were performed. The tests were performed using the electromechanical machine MTS Insight equipped with a 300kN loadcell, according to the ASTM D7137, at the test speed of 1,25 mm/min. For these tests, the specimen is mounted on a special tool which allows it to be kept stable on all 4 sides during the execution of the test. Figure 6.21 shows a photo of the sample mounted on the CAI test tool according to the ASTM D7137 standard.

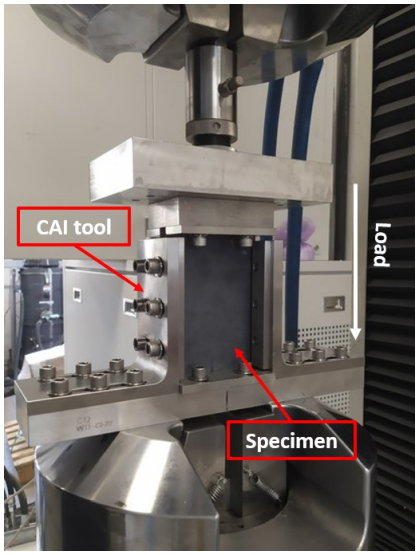

Figure 6.21: Compression after impact test experimental set-up.

Figure 6.22 shows photos of all the CAI tested samples. The stress-strain curves for both sets of samples are shown in Figure 6.23, while all the results in terms of Residual Strength are reported in the Table 6.11.

From the evaluation of the responses to the CAI test of the various panels both in terms of residual strength and failure modes, it is possible to note that:

- All the samples broke due to compression either in the upper or lower part of the specimen, only one (sample 4 with 20% infill density) broke in the center in correspondence with the damage induced by the impact. This allows us to hypothesize that the impact event only affects the impacted skin and its interface

with the trabecular core but does not affect the remaining part of the specimen whose properties remain unchanged. This confirms that the gyroid is a trabecular structure that allows good absorption of impact energy, preventing breakage of the sandwich panel.

- Panels with a 20% dense core exhibited a higher compression strength than panels with a 10% dense core, on average they obtained a 25,7% higher residual resistance. This means that the gyroid core contributes to the compressive resistance of the panel. This assumption is confirmed by the fact that the breakage of the skin occurred after the compression failure of the gyroid structure and therefore by the loss of adhesion at the contact points between the gyroid and the facesheet.
- There is a clear correlation with the results obtained from non-destructive inspections. In fact, the samples that in the ultrasound scans showed a greater extension of the damage (such as samples 2 and 3 for the 10% dense panels and samples 2,4,5 for the 20% dense panels), had a lower compressive strength compared to the panels having a more localized impact damage (such as samples 1 and 4 for the 10% dense panels and 1 and 3 for the 20% dense panels).

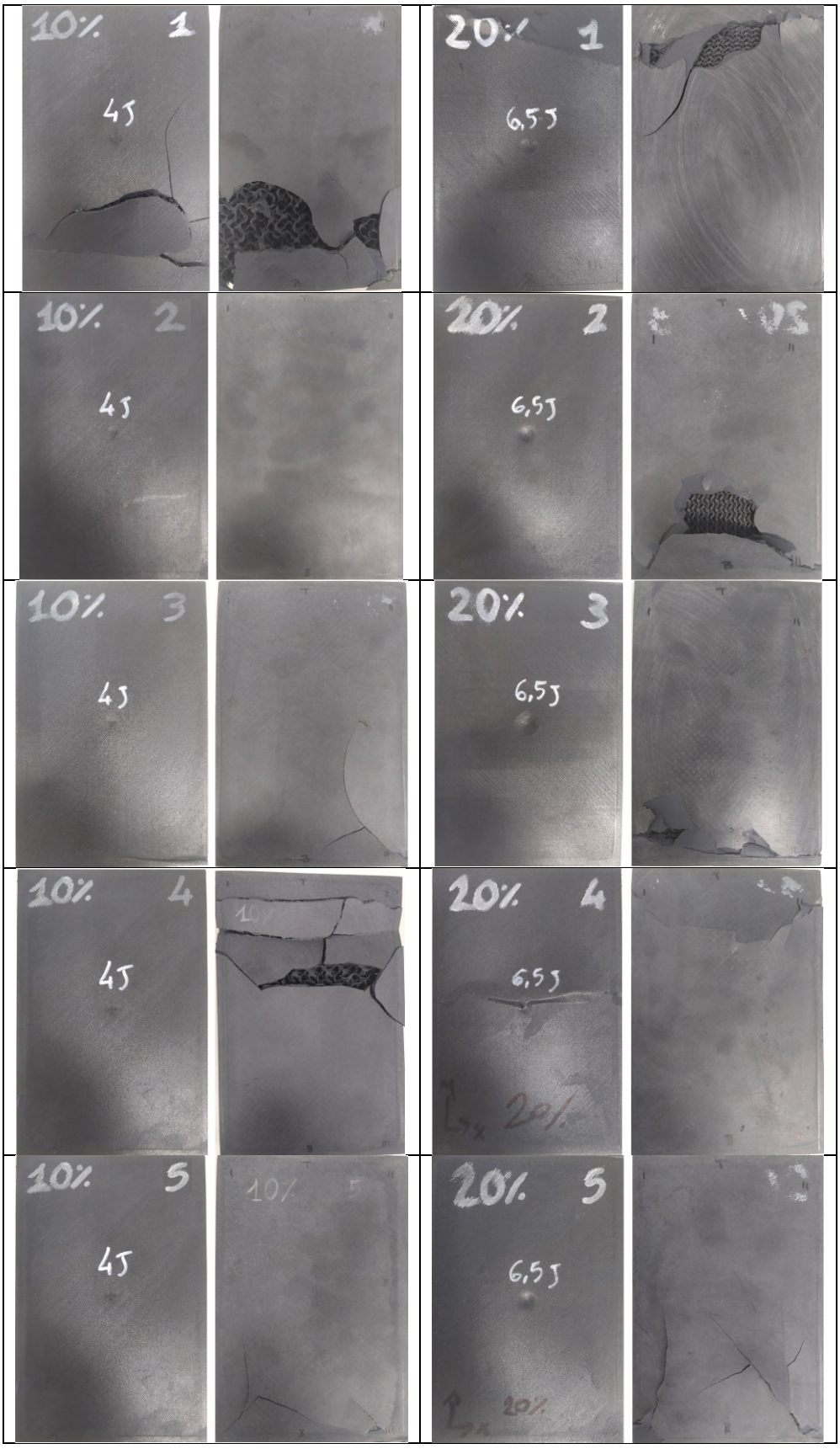

Figure 6.22: Upper and lower sides of CAI-tested samples.

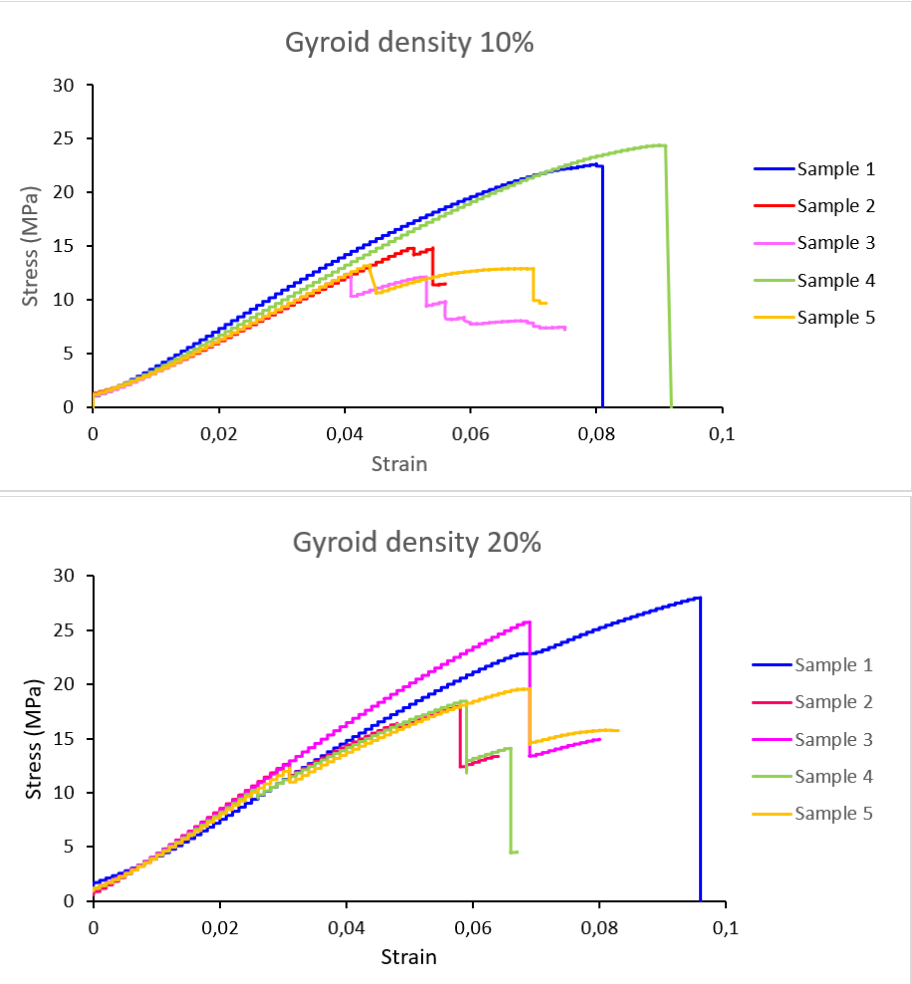

Figure 6.23: CAI stress-strain curves.

Sample ID	Residual Strength (MPa)	R.S. $_{average}$ (MPa)	St. dev. (MPa)
S1_Gyroid 10%	22,7		
S2_Gyroid 10%	14,8		
S3_Gyroid 10%	12,6	17,5	± 5,6
S4_Gyroid 10%	24,4		
S5_Gyroid 10%	13,3		
S1_Gyroid 20%	28,0		
S2_Gyroid 20%	18,1		
S3_Gyroid 20%	25,8	22,0	±4,6
S4_Gyroid 20%	18,5		
S5_Gyroid 20%	19,6		

Table 6.11: CAI test results.

The present preliminary study aimed to understand the mechanical behavior of C-PEEK 3D printed sandwich structures with a gyroid core under a low-velocity impact test and evaluate the influence of the core infill density on the panel mechanical properties. Both non-destructive and destructive experimental studies were performed in order to determine the panels energy absorption capability and failure mechanisms. The results revealed that the infill density has a strong influence on the mechanical properties and failure mechanism of the panel. Specifically, by increasing the core density from 10% to 20%, it was possible to increase the impact energy by 37,5% (from 4 J to 6,5 J), the average absorbed energy by 64,5% and the average residual resistance by 25,7%. Regarding the failure mechanisms of the panels, from the results obtained through ultrasound tests, the panels with the 10% dense core have suffered a more localized failure, probably due to a local failure or deflection in the unit cells of the gyroid immediately underlying the point of impact on the upper skin. This made it possible to limit the spread of the damage to the rest of the structure. Instead, for panels with a 20% dense core, the tensions generated by the deflection of the unit cells below the point of impact have propagated horizontally along the adjacent cells, causing a larger detachment zone between the skin and the core. These findings are still embryonic, it is necessary to test and study the properties of panels with the same geometry but different cores in terms of both density and trabecular structure to understand even better how the properties related to impact resistance vary. Furthermore, with the current solution, where the entire sandwich is 3D printed, it was found that the upper skin gets damaged first, indicating that the impact absorption effect given by the porous structure is not fully exploited. For this reason, to better evaluate the effect given by the gyroid core, it is planned to test it in sandwich panels with skins made of another material, for example panels of cured composite material or aluminum plates. However, this study paves the way for the development of innovative 3D printed sandwich panels in materials and geometries to obtain more resilient and energy-absorbing structures with a higher stiffness-to-weight ratio.

7 Conclusions and future developments

In the present research work, the initial study of the process parameters with the aim of optimizing the properties of PEEK 3D printed via FFF served to understand the phenomena that most influence the properties of the material, mainly linked to the formation of crystallites, the adhesion between the filament being extruded and the previous one which has already solidified. In this sense, high temperatures and low nozzle movement speeds play a fundamental role in lowering the polymer cooling rate, guaranteeing better mechanical properties. Considering the limits of the technology which do not allow total optimization of the process, and knowing the need of industry to reduce the production times of printed parts as much as possible, it was decided to test a surface treatment via cold atmospheric plasma. The aim was to increase interlayer adhesion using for example higher printing speeds and lower temperatures instead of the optimized ones. For this research, an in-depth study of the characterization of plasma-treated surfaces was undertaken as the treatment parameters varied: time and distance of the torch from the surface to be treated. In particular, the characterization involved thermal imaging to verify the temperature reached during the treatment, FTIR spectroscopy to understand the changes in the chemical composition of the material induced by the plasma, contact angle measurements to evaluate the increase in wettability and therefore in surface energy , and SEM imaging to highlight any changes in surface morphology. Among the most interesting results of this preliminary characterization, the appearance of polar functional groups was found which allow the formation of hydrogen bonds with the subsequently deposited polymer, strengthening the chemical bond at the interface, and the formation of crystallites on the surface which improve the mechanical interlocking. To demonstrate what was hypothesized, mechanical shear tests were carried out which revealed an increase of even more than 30% in resistance for the treated samples compared to the untreated ones. This study deserves to be further explored, but it paves the way for a new vision of industrial production using FFF, faster but more effective thanks to an almost instantaneous treatment of surfaces. The plasma treatment used in this study, in addition to being effective in a few seconds, adds the advantage of being a green chemical treatment, not making use of solvents and/or toxic precursor gases but using ambient air, and requiring low power consumption for the activation energies involved.

Subsequently, a characterization study of 3D printed C-PEEK gyroid structures was carried out, interesting from an industrial point of view because gyroid structures bring several advantages including: having a high strength-to-weight ratio and being isotropic. In fact, with this study it was demonstrated that the use of gyroid infill pattern for 3D printed parts, in addition to the possibility to make them lighter with unchanged mechanical resistance (resulting in savings in both material costs and production times), can mitigate the mechanical anisotropy caused by the technology and the use of anisotropic materials. The research was conducted starting from a study on the variation in the compressive strength of the structures as the infill density varied, subsequently compression tests along the x and y axes served to evaluate their potential isotropy. The results showed that: i) the compression behavior follows the trend of bending-dominated structures according to the Gibson-Ashby model, ii) with 70% of infill it was obtained the same strength-to-weight ratio that would be obtained with the 100% full structure, saving 30% of time and material, iii) at 25% of infill density the gyroid structure shows mechanical isotropy in all directions. Starting from these results, it was decided to test the low-velocity impact absorption properties of 3D printed sandwich structures having a gyroid core with 10% and 20% infill. This preliminary research showed that the impact energy that the panel could withstand increases as the density of the filling increases but that the damage found propagated less in panels with lower density. However, further investigations are necessary to better investigate the propagation of the damage within the core and on the lower skin of the sandwich. In this regard, Computed Tomography (CT scan) and pulse-echo ultrasound methods could provide more specific and accurate information. In addition to this, an optimization study of the panel design can be very useful in making the most of the advantages of the gyroid structure in energy absorption.

Overall, this thesis study served to better understand the behavior of high-performance polymeric materials such as PEEK and its composite C-PEEK when processed by FFF, and how to best exploit its properties to bring the use of this Additive Manufacturing technology within industrial production processes of aeronautical interest. Future developments will include the study and design of 3D printed PEEK and C-PEEK parts for aeronautical use, for example for the production of molds, tools or end-use products. The aims are to make the production of these objects smarter and more flexible both from a geometric and mechanical properties point of view, as well as to promote the sustainability and circular economy of the company. The latter is an increasingly

important objective for modern companies and, in the production of components in composite material, thermoplastic matrices certainly have the great advantage of being able to be more easily recycled, reused, repaired and remodeled almost infinite times without compromising the properties of the material.

Other future developments could be:

- The development of a predictive model for the mechanical performance of printed parts knowing the printing parameters, material and geometry
- The formulation of a thermoplastic matrix material filled with fibers recovered from the recycling of production waste
- The investigation of other surface treatment methods that can increase interlayer adhesion or reduce voids as much as possible, making the part mechanically more resistant.

References

[1] S. K. Georgantzinos, G. I. Giannopoulos, K. Stamoulis e S. Markolefa, «Composites in Aerospace and Mechanical Engineering,» *Materials,* vol. 16, n. 22, p. 7230, 2023.

[2] B. Parveez, M. I. Kittur, I. A. Badruddin, S. Kamangar, M. Hussien e M. A. Umarfarooq, «Scientific Advancements in Composite Materials for Aircraft Applications: A Review,» *Polymers,* vol. 14, n. 22, p. 5007, 2022.

[3] A. Asyraf, M. R. Ishak, S. M. Sapuan e Y. N., «Comparison of static and long-term creep behaviors between balau wood and glass fiber reinforced polymer composite,» *Fibers and Polymers,* vol. 22, pp. 793-803, 2021.

[4] B. Wang e H. Gao, «Fibre Reinforced Polymer Composites,» *Advances in Machining of Composite Materials: Conventional and Non-conventional Processes. Cham: Springer International Publishing,* pp. 15-43, 2021.

[5] A. Korycki, F. Carassus, O. Tramis, C. Garnier, T. Djilali e F. Chabert, «Polyaryletherketone Based Blends: A Review,» *Polymers,* vol. 15, n. 19, p. 3943, 2023.

[6] M. Rinaldi, T. Ghidini, F. Cecchini, A. Brandao e F. Nanni, «Additive layer manufacturing of poly(ether ether ketone) via FFF,» *Composites Paet B: Engineering,* vol. 145, p. 162–172, 2018.

[7] A. van Grootel, J. Chang, B. L. Wardle e E. Olivetti, «Manufacturing variability drives significant environmental and economic impact: The case of carbon fiber reinforced polymer composites in the aerospace industry,» *Journal of Cleaner Production,* vol. 261, 2020.

[8] A. Gloria, R. Montanari, M. Richetta e A. Varone, «Alloys for aeronautic applications: State of the art and perspectives,» *Metals,* vol. 9, n. 6, p. 662, 2019.

[9] A. Thakur, «Fatigue behavior and fracture mechanism of a hot rolled AA7020 aluminum alloy,» *nternational Journal of Current Engineering and Technology,* vol. 3, pp. 401-404, 2019.

[10] M. Paz Martínez-Viademonte, S. T. Abrahami, T. Hack, M. Burchardt e H. Terryn, «A review on anodizing of aerospace aluminum alloys for corrosion protection,» *Coatings,* vol. 10, n. 11, 2020.

[11] J. T. Burns, J. J. Jones, A. D. Thompson e J. W. Locke, «Fatigue crack propagation of aerospace aluminum alloy 7075-T651 in high altitude environments,» *International Journal of Fatigue,* vol. 106, pp. 196-207, 2018.

[12] A. Straubinger, R. Rothfeld, M. Shamiyeh, K. D. Büchter, J. Kaiser e K. O. Plötner, «An overview of current research and developments in urban air mobility–Setting the scene for UAM introduction,» *Journal of Air Transport Management,* vol. 87, 2020.

[13] A. Liberacki, B. Trincone, G. Duca, L. Aldieri, C. P. Vinci e F. Carlucci, «The Environmental Life Cycle Costs (ELCC) of Urban Air Mobility (UAM) as an input for sustainable urban mobility,» *Journal of Cleaner Production,* vol. 389, 2023.

[14] «Material and Process Selection Charts,» [Online]. Available: http://users.fs.cvut.cz/libor.benes/vyuka/engineeringmaterials/2-Materials-Charts-2010.pdf. [Consultato il giorno 06 08 2024].

[15] E. Oromiehie, B. G. Prusty, P. Compston e G. Rajan, «Automated fibre placement based composite structures: Review on the defects, impacts and inspections techniques,» *Composite Structures,* vol. 224, 2019.

[16] I. Hamerton e J. Kratz, «The use of thermosets in modern aerospace applications,» *Thermosets,* pp. 303-340, 2018.

[17] U. P. Breuer, Commercial aircraft composite technology, vol. 115, Springer International Publishing, 2016.

[18] M. R. Sheikhi, H. Aygun e O. Altuntas, «Aeroengines: Principles, Components, and Eco-friendly Trends,» *Materials, Structures and Manufacturing for Aircraft,* pp. 127-151, 2022.

[19] F. Ribeiro, J. Sena-Cruz e A. P. Vassilopoulos, «Tension-tension fatigue behavior of hybrid glass/carbon and carbon/carbon composites,» *International Journal of Fatigue,* vol. 146, 2021.

[20] T. A. Sebaey, M. Bouhrara e N. O'Dowd, «Fibre alignment and void assessment in thermoplastic carbon fibre reinforced polymers manufactured by automated tape placement,» *Polymers,* vol. 13, n. 3, p. 473, 2021.

[21] L. Iorio, F. Quadrini, N. Gallo e L. Santo, «Out-of-autoclave molding of carbon fiber laminates by consolidation with shape memory polymer foams,» *Journal of Composite Materials,* vol. 57, n. 26, pp. 4147-4156, 2023.

[22] O. A. Ekuase, N. Anjum, V. O. Eze e O. I. Okoli, «A review on the out-of-autoclave process for composite manufacturing,» *Journal of Composites Science,* vol. 6, n. 6, p. 172, 2022.

[23] S. Hassani, M. Mousavi e A. H. Gandomi, «Structural health monitoring in composite structures: A comprehensive review,» *Sensors,* vol. 22, n. 1, p. 153, 2021.

[24] Q. Miao, Z. Dai, G. Ma, F. Niu e D. Wu, «Effect of consolidation force on interlaminar shear strength of CF/PEEK laminates manufactured by laser-assisted forming,» *Composite Structures,* vol. 266, 2021.

[25] M. Barile, L. Lecce, M. Iannone, S. Pappadà e P. Roberti, «Thermoplastic composites for aerospace applications,» *Revolutionizing aircraft materials and processes,* pp. 87-114, 2020.

[26] R. B. Rigby, «Polyetheretherketone,» in *Engineering thermoplastics*, CRC Press, 2020, pp. 299-314.

[27] A. Korycki, F. Carassus, O. Tramis, C. Garnier, T. Djilali e F. Chabert, «Polyaryletherketone Based Blends: A Review,» *Polymers,* vol. 15, n. 19, 2023.

[28] D. G. Brady e H. W. Hill, «Polyphenylene sulfide,» in *Engineering Thermoplastics*, CRC Press, 2020, pp. 201-234.

[29] I. W. Serfaty, «Polyetherimide,» in *Engineering Thermoplastics*, CRC Press, 2020, pp. 283-297.

[30] A. S. Pouzada, Selection of thermoplastics, William Andrew Publishing, 2021.

[31] K. Ramaswamy, V. Modi, P. S. Rao, P. P. Martin, C. T. McCarthy e R. M. O'Higgins, «An investigation of the influence of matrix properties and fibre–matrix interface behaviour on the mechanical performance of carbon fibre-reinforced PEKK and PEEK composites,» *Composites Part A: Applied Science and Manufacturing,* vol. 165, p. 107359, 2023.

[32] J. Krishnasamy, R. Alagirusamy e G. Thilagavathi, «Potential Application Areas for Thermoplastic Composites,» in *Flexible Towpregs and Their Thermoplastic Composites*, CRC Press, 2022, pp. 397-414.

[33] P. M. Angelopoulos, M. Samouhos e M. Taxiarchou, «Functional fillers in composite filaments for fused filament fabrication; a review,» *Materials Today: Proceedings,* vol. 37, pp. 4031-4043, 2021.

[34] N. Van de Werken, H. Tekinalp, P. Khanbolouki, S. Ozcan, A. Williams e M. Tehrani, «Additively manufactured carbon fiber-reinforced composites: State of the art and perspective,» *Additive Manufacturing,* vol. 31, p. 100962, 2020.

[35] I. Gibson, D. Rosen, B. Stucker, M. Khorasani, I. Gibson, D. Rosen e M. ... Khorasani, «Material extrusion,» *Additive Manufacturing Technologies,* pp. 171-201, 2021.

[36] A. Curmi e A. Rochman, «Miniaturized fused granulate fabrication of polyether ether ketone (PEEK),» *Progress in Additive Manufacturing,* vol. 9, n. 4, pp. 1265-1275, 2024.

[37] J. M. T. A. R. L. M. C. &. D. X. Pappas, « A comparative study of pellet-based extrusion deposition of short, long, and continuous carbon fiber-reinforced polymer composites for large-scale additive manufacturing,» *Journal of Manufacturing Science and Engineering,* vol. 143, n. 7, p. 071012, 2021.

[38] L. Fontana, A. Giubilini, R. Arrigo, G. Malucelli e P. Minetola, «Characterization of 3D printed polylactic acid by fused granular fabrication through printing accuracy, porosity, thermal and mechanical analyses,» *Polymers,* vol. 14, n. 17, p. 3530, 2022.

[39] P. Q. K. Nguyen, J. Panta, T. Famakinwa, R. C. Yang, A. Ahmed, M. Stapleton, D. Sassaman, S. Snabes e C. Craff, «Influences of printing parameters on mechanical properties of recycled PET and PETG using fused granular fabrication technique,» *Polymer Testing,* vol. 132, p. 108390, 2024.

[40] C. M. Vicente, M. Sardinha, L. Reis, A. Ribeiro e M. Leite, «Large-format additive manufacturing of polymer extrusion-based deposition systems: Review and applications,» *Progress in Additive Manufacturing,* vol. 8, n. 6, pp. 1257-1280, 2023.

[41] J. Brackett, Y. Yan, D. Cauthen, V. Kishore, J. Lindahl, T. Smith, T. Sudbury, Z. Ning, H. Kunc e C. Duty, «Characterizing material transitions in large-scale Additive Manufacturing,» *Additive Manufacturing,* vol. 38, p. 101750, 2021.

[42] K. Babaremu, A. Adediji, N. Olumba, S. Okoya, E. Akinlabi e M. Oyinlola, «Technological Advances in Mechanical Recycling Innovations and Corresponding Impacts on the Circular Economy of Plastics,» *Environments,* vol. 11, n. 3, p. 38, 2024.

[43] J. S. Sohn, Y. Ryu, C. S. Yun, K. Zhu e S. W. Cha, « Extrusion compounding process for the development of eco-friendly SCG/PP composite pellets,» *Sustainability,* vol. 11, n. 6, p. 1720, 2019.

[44] S. Singamneni, M. P. Behera, D. Truong, M. J. Le Guen, E. Macrae e K. Pickering, «Direct extrusion 3D printing for a softer PLA-based bio-polymer composite in pellet form,» *Journal of Materials Research and Technology,* vol. 15, pp. 936-949, 2021.

[45] A. Sanchez Ramirez, M. E. Islán Marcos, F. Blaya Haro, R. D'Amato, R. Sant e J. Porras, «Application of FDM technology to reduce aerodynamic drag,» *Rapid Prototyping Journal,* vol. 25, n. 4, pp. 781-791, 2019.

[46] S. Salifu, D. Desai, O. Ogunbiyi e K. Mwale, «Recent development in the additive manufacturing of polymer-based composites for automotive structures—A review,» *Materials Today: Proceedings,* vol. 119, n. 11, pp. 6877-6891, 2022.

[47] L. M. Galantucci, A. Pellegrini, M. G. Guerra e F. Lavecchia, «3D printing of parts using metal extrusion: an overview of shaping debinding and sintering technology,» *Advanced Technologies and Materials,* vol. 47, n. 1, pp. 25-32, 2022.

[48] K. Günaydın e H. S. Türkmen, «Common FDM 3D printing defectsa,» *International congress on 3D printing (additive manufacturing) technologies and digital industry,* pp. 19--21, April 2018.

[49] M. Doshi, A. Mahale, S. K. Singh e S. Deshmukh, «Printing parameters and materials affecting mechanical properties of FDM-3D printed Parts: Perspective and prospects,» *{Materials Today: Proceedings,* vol. 50, pp. 2269--2275, 2022.

[50] I. Gajdoš, E. Spišák, L. Kaščák e V. Krasinskyi, «Surface finish techniques for FDM parts,» in *Materials science forum*, Trans Tech Publ, 2015, pp. 45-48.

[51] I. Gajdoš, E. Spišák, L. Kaščák e V. Krasinskyi, «The surface quality improvement methods for FDM printed parts: a review,» *Fused deposition modeling based 3D printing,* pp. 167-194, 2021.

[52] A. Karimi, D. Rahmatabadi e M. Baghani, «Various FDM mechanisms used in the fabrication of continuous-fiber reinforced composites: a review,» *Polymers,* vol. 16, n. 6, p. 831, 2024.

[53] A. El Magri, S. Vanaei e S. Vaudreuil, «An overview on the influence of process parameters through the characteristic of 3D-printed PEEK and PEI parts,» *High Performance Polymers,* vol. 33, n. 8, pp. 862-880, 2021.

[54] M. Rinaldi, T. Ghidini, F. Cecchini, A. Brandao e F. Nanni, «Additive layer manufacturing of poly (ether ether ketone) via FDM,» *Composites Part B: Engineering,* vol. 145, pp. 162-172, 2018.

[55] A. Das, C. A. Chatham, J. J. Fallon, C. E. Zawaski, E. L. Gilmer, C. B. Williams e M. J. Bortner, «Current understanding and challenges in high temperature additive manufacturing of engineering thermoplastic polymers,» *Additive Manufacturing,* vol. 34, p. 101218, 2020.

[56] M. Spoerk, C. Holzer e J. Gonzalez-Gutierrez, «Material extrusion-based additive manufacturing of polypropylene: A review on how to improve dimensional inaccuracy and warpage,» *Journal of Applied Polymer Science,* vol. 137, n. 12, p. 48545, 2020.

[57] B. Hu, X. Duan, Z. Xing, Z. Xu, C. Du, H. Zhou e B. ... Shan, «Improved design of fused deposition modeling equipment for 3D printing of high-performance PEEK parts,» *Mechanics of Materials,* vol. 137, p. 103139, 2019.

[58] M. Vaezi e S. Yang, «Extrusion-based additive manufacturing of PEEK for biomedical applications,» *Virtual and Physical Prototyping,* vol. 10, n. 3, pp. 123-135, 2015.

[59] W. Z. Wu, P. Geng, J. Zhao, Y. Zhang, D. W. Rosen e H. B. Zhang, «Manufacture and thermal deformation analysis of semicrystalline polymer polyether ether ketone by 3D printing,» *Materials Research Innovations,* vol. 18, n. sup5, pp. S5-12, 2014.

[60] L. Jin, J. Ball, T. Bremner e H. J. Sue, «Crystallization behavior and morphological characterization of poly (ether ether ketone),» *Polymer,* vol. 55, n. 20, pp. 5255-5265, 2014.

[61] C. Yang, X. Tian, D. Li, Y. Cao, F. Zhao e C. Shi, «Influence of thermal processing conditions in 3D printing on the crystallinity and mechanical properties of PEEK material,» *Journal of Materials Processing Technology,* vol. 248, pp. 1-7, 2017.

[62] P. Wang, B. Zou, H. Xiao, S. Ding e C. Huang, «Effects of printing parameters of fused deposition modeling on mechanical properties, surface quality, and microstructure of PEEK,» *Journal of Materials Processing Technology,* vol. 271, pp. 62-74, 2019.

[63] S. Ding, B. Zou, W. P. e H. Ding, «Effects of nozzle temperature and building orientation on mechanical properties and microstructure of PEEK and PEI printed by 3D-FDM,» *Polymer Testing,* vol. 78, p. 105948, 2019.

[64] K. Rahman, T. Letcher e R. Reese, «Mechanical properties of additively,» *Proceedings of the ASME 2015 International Mechanical Engineering Congress and Exposition (IMECE 2015),* vol. 57359, p. V02AT02A009, 13-19 November 2015.

[65] M. F. Arif, S. Kumar, K. M. Varadarajan e W. J. Cantwell, «Performance of biocompatible PEEK processed by fused deposition additive manufacturing,» *Materials & Design,* vol. 146, pp. 249-259, 2018.

[66] G. Cicala, A. Latteri, B. Del Curto, A. Lo Russo, G. Recca e S. Farè, «Engineering thermoplastics for additive manufacturing: A critical perspective with experimental evidence to support functional applications,» *Journal of applied biomaterials & functional materials,* vol. 15, n. 1, pp. 10-18, 2017.

[67] R. Wang, K. J. Cheng, R. C. Advincula e Q. Chen, «On the thermal processing and mechanical properties of 3D-printed polyether ether ketone,» *MRS Communications,* vol. 9, pp. 1046-1052, 2019.

[68] C. Y. Liaw, J. W. Tolbert, L. W. Chow e M. Guvendiren, «Interlayer bonding strength of 3D printed PEEK specimens,» *Soft matter,* vol. 17, n. 18, pp. 4775-4789, 2021.

[69] B. Neuhaus, M. K. Idris, P. Naderi, Y. El-Hajj e G. Grau, «Low-Roughness 3D-Printed Surfaces by Ironing for the Integration with Printed Electronics,» *Advanced Engineering Materials,* vol. 26, n. 3, p. 2301711, 2024.

[70] G. Stano, A. Pavone, M. A. Jafor, K. Matalgah, G. Percoco e T. J. Fleck, «Enhancing the sensitivity of 3D printed sensors via ironing and void reduction,» *Virtual and Physical Prototyping,* vol. 19, n. 1, p. e2331153, 2024.

[71] Y. Shang, Q. Xu, B. Jiang, Y. Yang, X. Liu, Z. Jiang, C. Yu, X. Li e H. Zhang, «Slowing crystallization to enhance interlayer strength of 3D printed poly (ether ether ketone) parts by molecular design,» *Additive Manufacturing,* vol. 59, p. 103104, 2022.

[72] Q. Xu, W. Xu, Y. Yang, X. Yin, C. Zhou, J. Han, X. Li, Y. Shang e H. Zhang, «Enhanced interlayer strength in 3D printed poly (ether ether ketone) parts,» *Additive Manufacturing,* vol. 55, p. 102852, 2022.

[73] Q. Li, W. Zhao, B. Niu, Y. Wang, X. Wu, J. Ji, Y. Li, T. Zhao, H. Li e G. Wang, «3D printing high interfacial bonding polyether ether ketone components via pyrolysis reactions,» *Materials & Design,* vol. 198, p. 109333, 2021.

[74] R. Rane, Enhancing Tensile Strength of FDM parts using Thermal Annealing and Uniaxial Pressure, The University of Texas at Arlington, 2018.

[75] S. Bhandari, R. A. Lopez-Anido e D. J. Gardner, «Enhancing the interlayer tensile strength of 3D printed short carbon fiber reinforced PETG and PLA composites via annealing,» *Additive Manufacturing,* vol. 30, p. 100922, 2019.

[76] A. Andreu, S. Kim, J. Dittus, M. Friedmann, J. Fleischer e Y. J. Yoon, «Hybrid material extrusion 3D printing to strengthen interlayer adhesion through hot rolling,» *Additive Manufacturing,* vol. 55, p. 102773, 2022.

[77] N. Sabyrov, A. Abilgaziyev e M. H. Ali, «Enhancing interlayer bonding strength of FDM 3D printing technology by diode laser-assisted system,» *The International Journal of Advanced Manufacturing Technology,* vol. 108, pp. 603-611, 2020.

[78] J. Yao, A. Duongthipthewa, X. Xu, M. Liu, Y. Xiong e L. Zhou, «Interlayer bonding improvement of PEEK and CF-PEEK composites with laser-assisted fused deposition modeling,» *Composites Communications,* vol. 45, p. 101819, 2024.

[79] A. Uşun, B. B. Vatandaş e R. Gümrük, «Enhanced mechanical properties of continuous carbon fiber reinforced polyether-ether-ketone composites via infrared preheating and high fiber volume fraction,» *Additive Manufacturing,* vol. 89, p. 104289, 2024.

[80] V. Kishore, C. Ajinjeru, A. Nycz, B. Post, J. Lindahl, V. Kunc e C. Duty, «Infrared preheating to improve interlayer strength of big area additive manufacturing (BAAM) components,» *Additive Manufacturing,* vol. 14, pp. 7-12, 2017.

[81] C. C. Shih, M. Burnette, D. Staack, J. Wang e B. L. Tai, «Effects of cold plasma treatment on interlayer bonding strength in FFF process,» *Additive Manufacturing,* vol. 25, pp. 104-111, 2019.

[82] M. Zarei, M. M. H. Nikoo, R. Alizadeh e A. Askarinya, «Synergistic effect of CaCO3 addition and in-process cold atmospheric plasma treatment on the surface evolution, mechanical properties, and in-vitro degradation behavior of FDM-printed PLA scaffolds,» *Journal of the Mechanical Behavior of Biomedical Materials,* vol. 149, p. 106239, 2024.

[83] H. Narahara, Y. Shirahama e H. Koresawa, «Improvement and evaluation of the interlaminar bonding strength of FDM parts by atmospheric-pressure plasma,» *Procedia Cirp,* vol. 42, pp. 754-759, 2016.

[84] A. V. Nastuta, M. Asandulesa, I. Spiridon, C. D. Varganici, R. Huzum e I. Mihaila, «Effects of Atmospheric Pressure Plasma Jet on 3D-Printed Acrylonitrile Butadiene Styrene (ABS),» *Materials,* vol. 17, n. 98, p. 1848, 2024.

[85] T. D. McLouth, S. M. Gustafson, H. I. Kim e R. J. Zaldivar, «Enhancement of FDM ULTEM® 9085 bond strength via atmospheric plasma treatment,» *Journal of Manufacturing Processes,* vol. 66, pp. 179-188, 2021.

[86] «Piezobrush PZ3 brochure,» [Online]. Available: https://www.intertronics.co.uk/wp-content/uploads/2020/04/PZ3-Brochure.pdf.

[87] M. Rakhshbahar e M. Sinapius, «A novel approach: combination of automated fiber placement (AFP) and additive layer manufacturing (ALM),» *Journal of Composites Science,* vol. 2, n. 3, p. 42, 2018.

[88] A. Alghamdi, T. Maconachie, D. Downing, M. Brandt, M. Qian e M. Leary, «Effect of additive manufactured lattice defects on mechanical properties: an automated method for the enhancement of lattice geometry,» *The International Journal of Advanced Manufacturing Technology,* vol. 108, pp. 957-971, 2020.

[89] W. H. Meeks III e H. Rosenberg, «The geometry of periodic minimal surfaces,» *Comment. Math. Helvetici,* vol. 68, n. 538-578, pp. 8-11, 1993.

[90] M. Arsentev, E. Topalov, S. Balabanov, E. Sysoev, I. Shulga, M. Akhmatnabiev, M. Sychov, E. Skorb e M. Nosonovsky, «Crystal-Inspired Cellular Metamaterials and Triply Periodic Minimal Surfaces,» *Biomimetics,* vol. 9, n. 5, p. 285, 2024.

[91] A. Panesar, M. Abdi, D. Hickman e I. Ashcroft, «Strategies for functionally graded lattice structures derived using topology optimisation for additive manufacturing,» *Additive manufacturing,* vol. 19, pp. 81-94, 2018.

[92] J. Song, M. Wang, D. Li e J. Zhang, «Deformation and Energy Absorption Performance of Functionally Graded TPMS Structures Fabricated by Selective Laser Melting,» *Applied Sciences,* vol. 14, n. 5, p. 2064, 2024.

[93] M. Z. Saghir e M. Yahya, «Convection Heat Transfer and Performance Analysis of a Triply Periodic Minimal Surface (TPMS) for a Novel Heat Exchanger,» *Energies,* vol. 17, n. 17, p. 4275, 2024.

[94] X. Liu, B. Zou, H. Xing e C. Huang, «The preparation of ZrO2-Al2O3 composite ceramic by SLA-3D printing and sintering processing,» *Ceramics International,* vol. 46, n. 1, pp. 937-944, 2020.

[95] J. Wang, C. Shi, N. Yang, H. Sun, Y. Liu e B. Song, «Strength, stiffness, and panel peeling strength of carbon fiber-reinforced composite sandwich structures with aluminum honeycomb cores for vehicle body,» *Composite Structures,* vol. 184, pp. 1189-1196, 2018.

[96] V. T. Le, N. San Ha e N. S. Goo, «Advanced sandwich structures for thermal protection systems in hypersonic vehicles: A review,» *Composites Part B: Engineering,* vol. 226, p. 109301, 2021.

[97] M. Al Rifaie, H. Abdulhadi e A. Mian, «Advances in mechanical metamaterials for vibration isolation: A review.,» *Advances in Mechanical Engineering,* vol. 14, n. 3, p. 16878132221082872, 2022.

[98] A. Al-Fatlawi, K. Jármai e G. Kovács, «Optimum design of solar sandwich panels for satellites applications,» in *Vehicle and Automotive Engineering 3: Proceedings of the 3rd VAE2020*, Miskolc, Hungary, Springer , 2021, pp. 427-442.

[99] K. Zhao, P. Okolo, E. Neri, P. Chen, J. Kennedy e G. Bennett, «Noise reduction technologies for aircraft landing gear-A bibliographic review,» *Progress in Aerospace Sciences,* vol. 112, p. 100589, 2020.

[100] H. Eschen, M. Harnisch e T. Schüppstuhl, «Flexible and automated production of sandwich panels for aircraft interior,» *Procedia manufacturing,* vol. 18, pp. 35-42, 2018.

[101] Y. Chai, W. Gao, B. Ankay, F. Li e C. Zhang, «Aeroelastic analysis and flutter control of wings and panels: a review,» *International Journal of Mechanical System Dynamics,* vol. 1, n. 1, pp. 5-34, 2021.

[102] M. Sahib, G. Kovács e S. Szávai, «Weight optimization of all-composite sandwich structures for automotive applications,» in *Vehicle and Automotive Engineering*, Springer International Publishing, 2022, pp. 720-733.

[103] A. Arasun, S. Subramaniyan e P. Kongphan, «Potential use of sandwich structure for biomedical applications: A review,» in *AIP Conference Proceedings*, vol. 2955, 2023.

[104] F. X. Irisarri, C. Julien, D. Bettebghor, F. Lavelle, Y. Guerin e K. Mathis, «A general optimization strategy for composite sandwich structures,» *Structural and Multidisciplinary Optimization,* vol. 63, pp. 3027-3044, 2021.

[105] Y. Zhang, M. Xiao, X. Zhang e L. Gao, «Topological design of sandwich structures with graded cellular cores by multiscale optimization,» *Computer Methods in Applied Mechanics and Engineering,* vol. 361, p. 112749, 2020.

[106] I. Ferreira, M. Machado, F. Alves e A. Torres Marques, «A review on fibre reinforced composite printing via FFF,» *Rapid Prototyping Journal,* vol. 25, n. 6, pp. 972-988, 2019.

[107] L. Novakova-Marcincinova, J. Novak-Marcincin, J. Barna e J. Torok, «Special materials used in FDM rapid prototyping technology application,» in *2012 IEEE 16th International Conference on Intelligent Engineering Systems (INES)*, 2012, pp. 73-76.

[108] P. Wang, B. Zou, S. Ding, L. Li e C. Huan, «Effects of FDM-3D printing parameters on mechanical properties and microstructure of CF/PEEK and GF/PEEK,» *Chinese Journal of Aeronautics,* vol. 34, n. 9, pp. 236-246, 2021.

[109] B. Aloyaydi, S. Sivasankaran e A. Mustafa, «Investigation of infill-patterns on mechanical response of 3D printed poly-lactic-acid,» *Polymer Testing,* vol. 87, p. 106557, 2020.

[110] M. M. S. &. K. A. Moradi, «3D printed parts with honeycomb internal pattern by fused deposition modelling; experimental characterization and production optimization,» *Metals and Materials International,* vol. 25, pp. 1312-1325, 2019.

[111] J. Kiendl e C. Gao, «Controlling toughness and strength of FDM 3D-printed PLA components through the raster layup,» *Composites Part B: Engineering,* vol. 180, p. 107562, 2020.

[112] M. Nabipour e B. Akhoundi, «An experimental study of FDM parameters effects on tensile strength, density, and production time of ABS/Cu composites,» *Journal of Elastomers & Plastics,* vol. 53, n. 2, pp. 146-164, 2021.

[113] A. Dey e N. Yodo, « A systematic survey of FDM process parameter optimization and their influence on part characteristics.,» *Journal of Manufacturing and Materials Processing,* vol. 3, n. 3, p. 64, 2019.

[114] H. Bakhtiari, M. Nikzad e M. Tolouei-Rad, «Influence of three-dimensional printing parameters on compressive properties and surface smoothness of polylactic acid specimens,» *Polymers,* vol. 15, n. 18, p. 3827, 2023.

[115] M. Timoumi, N. Barhoumi, A. Znaidi, A. Maazouz e K. Lamnawar, «Mechanical behavior of 3D-printed PEEK and its application for personalized orbital implants with various

infill patterns and densities,» *Journal of the mechanical behavior of biomedical materials,* vol. 136, p. 105534, 2022.

[116] A. Nabavi-Kivi, M. R. Ayatollahi e N. Razavi, «Investigating the effect of raster orientation on fracture behavior of 3D-printed ABS specimens under tension-tear loading.,» *European Journal of Mechanics-A/Solids,* vol. 99, p. 104944, 2023.

[117] E. Yasa e K. Ersoy, «Dimensional accuracy and mechanical properties of chopped carbon reinforced polymers produced by material extrusion additive manufacturing,» *Materials,* vol. 12, n. 23, p. 3885, 2019.

[118] «Anisotropy in 3D printing,» [Online]. Available: https://www.protolabs.com/en-gb/resources/blog/considerations-for-3d-printed-part-orientation/.

[119] J. Feng, J. Fu, X. Yao e Y. He, «Triply periodic minimal surface (TPMS) porous structures: from multi-scale design, precise additive manufacturing to multidisciplinary applications,» *International Journal of Extreme Manufacturing,* vol. 4, n. 2, p. 022001, 2022.

[120] Z. Qin, G. S. Jung, M. J. Kang e M. J. Buehler, «The mechanics and design of a lightweight three-dimensional graphene assembly,» *Science advances,* vol. 3, n. 1, p. e1601536, 2017.

[121] T. Maconachie, R. Tino, B. Lozanovski, M. Watson, A. Jones, C. Pandelidi e M. ... Leary, «The compressive behaviour of ABS gyroid lattice structures manufactured by fused deposition modelling.,» *The International Journal of Advanced Manufacturing Technology,* vol. 107, pp. 4449-4467, 2020.

[122] X. Li, L. Xiao e W. Song, « Compressive behavior of selective laser melting printed Gyroid structures under dynamic loading,» *Additive Manufacturing,* vol. 46, p. 102054, 2021.

[123] S. Kanwar e S. Vijayavenkataraman, «Design of 3D printed scaffolds for bone tissue engineering: A review,» *Bioprinting,* vol. 24, p. e00167, 2021.

[124] B. I. Oladapo, J. F. Kayode, P. Karagiannidis, N. Naveed, H. Mehrabi e K. O. Ogundipe, «Polymeric composites of cubic-octahedron and gyroid lattice for biomimetic dental implants,» *Materials Chemistry and Physics,* vol. 289, p. 126454, 2022.

[125] S. Kanwar e S. Vijayavenkataraman, « Design of 3D printed scaffolds for bone tissue engineering: A review,» *Bioprinting,* vol. 24, p. e00167, 2021.

[126] H. Spece, T. Yu, A. W. Law, M. Marcolongo e S. M. Kurtz, «3D printed porous PEEK created via fused filament fabrication for osteoconductive orthopaedic surfaces,» *Journal of the mechanical behavior of biomedical materials,* vol. 109, p. 103850, 2020.

[127] H. Ramos, R. Santiago, S. Soe, P. Theobald e M. Alves, «Response of gyroid lattice structures to impact loads,» *International Journal of Impact Engineering,* vol. 164, p. 104202, 2022.

[128] S. G. Khiavi, B. M. Sadeghi e M. Divandari, «Effect of topology on strength and energy absorption of PA12 non-auxetic strut-based lattice structures,» *journal of materials research and technology,* vol. 21, pp. 1595-1613, 2022.

[129] M. F. Ashby, «The properties of foams and lattices,» *Philosophical Transactions of the Royal Society A: Mathematical, Physical and Engineering Sciences,* vol. 364, n. 1838, pp. 15-30, 2006.

[130] I. Maskery, N. T. Aboulkhair, A. O. Aremu, C. J. Tuck e I. A. Ashcroft, « Compressive failure modes and energy absorption in additively manufactured double gyroid lattices,» *Additive Manufacturing,* vol. 16, pp. 24-29, 2017.

[131] E. Yang, M. Leary, B. Lozanovski, D. Downing, M. Mazur, A. Sarker e M. ... Brandt, «Effect of geometry on the mechanical properties of Ti-6Al-4V Gyroid structures fabricated via SLM: A numerical study,» *Materials & Design,* vol. 184, p. 108165, 2019.

[132] A. Yánez, A. Herrera, O. Martel, D. Monopoli e H. Afonso, « Compressive behaviour of gyroid lattice structures for human cancellous bone implant applications,» *Materials Science and Engineering: C,* vol. 68, pp. 445-448, 2016.

[133] D. W. Abueidda, M. Elhebeary, C. S. A. Shiang, S. Pang, R. K. A. Al-Rub e I. M. Jasiuk, «Mechanical properties of 3D printed polymeric Gyroid cellular structures: Experimental and finite element study,» *Materials & Design,* vol. 165, p. 107597, 2019.

[134] S. Higuera, R. Miralbes e D. Ranz, «Mechanical properties and energy–absorption capabilities of thermoplastic sheet gyroid structures,» *Mechanics of Advanced Materials and Structures,* vol. 29, n. 25, pp. 4110-4124, 2022.

[135] J. Zhang, X. Chen, Y. Sun, Y. Wang e L. Bai, «Sound-absorption and mechanical properties of multisheet Gyroid lattice structures by stereolithography,» *Composite Structures,* vol. 325, p. 117589, 2023.

[136] Z. Huang, J. Chen, Y. Huo e J. Zhao, «The Thermal Properties, Mechanical Performances and Crystallization behaviors of Poly (aryl Ether Ketone) Copolymers by the effect of Ether/Ketone Ratio,» *Journal of Polymer Materials,* vol. 38, n. 3/4, pp. 257-269, 2021.

[137] K. Rodzeń, A. McIlhagger, B. Strachota, A. Strachota, B. J. Meenan e A. Boyd, «Controlling crystallization: a key factor during 3D printing with the advanced semicrystalline polymeric materials PEEK, PEKK 6002, and PEKK 7002,» *Macromolecular Materials and Engineering,* vol. 308, n. 7, p. 2200668, 2023.

[138] T. Liu, X. Tian, Y. Zhang, Y. Cao e D. Li, «High-pressure interfacial impregnation by micro-screw in-situ extrusion for 3D printed continuous carbon fiber reinforced nylon composites,» *Composites Part A: Applied Science and Manufacturing,* vol. 130, p. 105770, 2020.

[139] M. Luo, X. Tian, J. Shang, W. Zhu, D. Li e Y. Qin, «Impregnation and interlayer bonding behaviours of 3D-printed continuous carbon-fiber-reinforced poly-ether-ether-ketone composites,» *Composites Part A: Applied Science and Manufacturing,* vol. 121, pp. 130-138, 2019.

[140] H. Ning, N. Lu, A. A. Hassen, K. Chawla, M. Selim e S. Pillay, «A review of Long fibre thermoplastic (LFT) composites.,» *International Materials Reviews,* vol. 65, n. 3, pp. 164-188, 2020.

[141] Y. Kim e O. O. Park, «Effect of fiber length on mechanical properties of injection molded long-fiber-reinforced thermoplastics,» *Macromolecular Research,* vol. 28, pp. 433-444, 2020.

[142] H. L. Tekinalp, V. Kunc, G. M. Velez-Garcia, C. E. Duty, L. J. Love, A. K. Naskar e S. ... Ozcan, «Highly oriented carbon fiber–polymer composites via additive manufacturing,» *Composites Science and Technology,* vol. 105, pp. 144-150, 2014.

[143] A. A. Hassen, R. B. Dinwiddie, S. Kim, H. L. Tekinalp, V. Kumar, J. Lindahl e V. ... Kunc, «Anisotropic thermal behavior of extrusion-based large scale additively manufactured carbon-fiber reinforced thermoplastic structures,» *Polymer Composites,* vol. 43, n. 6, pp. 3678-3690, 2022.

[144] L. J. Love, C. E. Duty, B. K. Post, R. F. Lind, P. D. Lloyd, V. Kunc e C. A. ... Blue, «Breaking barriers in polymer additive manufacturing,» Oak Ridge National Lab.(ORNL), Oak Ridge, TN (United States), Manufacturing Demonstration Facility (MDF), 2015.

[145] D. Veazey, T. Hsu e E. D. Gomez, «Next generation high-performance carbon fiber thermoplastic composites based on polyaryletherketones,» *Journal of applied polymer science,* vol. 134, n. 6, 2017.

[146] E. A. Hassan, L. Yang, T. H. Elagib, D. Ge, X. Lv, J. Zhou e S. ... Zhu, «Synergistic effect of hydrogen bonding and π-π stacking in interface of CF/PEEK composites,» *Composites Part B: Engineering,* vol. 171, pp. 70-77, 2019.

[147] X. Wang, Z. Huang, M. Lai, L. Jiang, Y. Zhang e H. Zhou, «Highly enhancing the interfacial strength of CF/PEEK composites by introducing PAIK onto diazonium functionalized carbon fibers,» *Applied Surface Science,* vol. 510, p. 145400, 2020.

[148] «PEEK datasheet,» [Online]. Available: https://rimas3d.com/wp-content/uploads/2020/05/TDS-Peek.pdf.

[149] «C-PEEK datasheet,» [Online]. Available: https://rimas3d.com/wp-content/uploads/2020/05/TDS-CarbonPeek.pdf.

[150] A. Bahar, S. Belhabib, S. Guessasma, F. Benmahiddine, A. E. A. Hamami e R. Belarbi, «Mechanical and thermal properties of 3D printed polycarbonate,» *Energies,* vol. 15, n. 10, p. 3686, 2022.

[151] «PC-S datasheet,» [Online]. Available: https://www.crea3d.com/it/kimya/886-1135-kimya-pc-s-750g.html.

[152] «Roboze 3D printers,» [Online]. Available: https://rimas3d.com/wp-content/uploads/2020/03/Rimas_Stampanti_FDM_gamma_Roboze.pdf.

[153] D. Korzec, F. Hoppenthaler e S. Nettesheim, «Piezoelectric direct discharge: Devices and applications,» *Plasma,* vol. 4, n. 1, pp. 1-41, 2020.

[154] D. Korzec, D. Neuwirth e S. Nettesheim, «Generation of negative air ions by use of piezoelectric cold plasma generator,» *Plasma,* vol. 4, n. 3, p. 29, 2021.

[155] P. Dimitrakellis e E. Gogolides, «Hydrophobic and superhydrophobic surfaces fabricated using atmospheric pressure cold plasma technology: A review,» *Advances in colloid and interface science,* vol. 254, pp. 1-21, 2018.

[156] M. Behnecke, V. Steinert e S. Petersen, «Surface characterisation of PEEK and dentin, treated with atmospheric non-thermal PDD plasma, applicable for dental chair-side procedures,» *Plasma,* vol. 4, n. 3, pp. 389-398, 2021.

[157] M. S. H. Akash e K. Rehman, «Differential scanning calorimetry,» *Essentials of pharmaceutical analysis,* pp. 199-206, 2020.

[158] A. El Magri, K. El Mabrouk, S. Vaudreuil, H. Chibane e M. E. Touhami, «Optimization of printing parameters for improvement of mechanical and thermal performances of 3D printed poly (ether ether ketone) parts,» *Journal of Applied Polymer Science,* vol. 137, n. 37, p. 49087, 2020.

[159] «DSC 250-TA instruments,» [Online]. Available: https://www.tainstruments.com/wp-content/uploads/DSC-250-291x291.png.

[160] «Optical microscope,» [Online]. Available: https://edinst.com/wp-content/uploads/2023/07/Fig-2-1024x766.png.

[161] «Hirox RH-2000 digital optical microscope,» [Online]. Available: https://www.mikrosistem.com.tr/eng/urun-mikroskop-hirox-3d-dijital-mikroskoplar-rh-2000-1164.

[162] «Scanning Electron Microscopy,» [Online]. Available: https://www.nanoscience.com/techniques/scanning-electron-microscopy/.

[163] «Zeiss Sigma 300 VP - SEM,» [Online]. Available: https://encrypted-tbn0.gstatic.com/images?q=tbn:ANd9GcTCHJK_3wIKoD5fuqxCyEc_z9dn-zks1wly0g&s.

[164] «Michelson's interferometer,» [Online]. Available: https://www.wikiwand.com/en/articles/Fourier_transform_infrared_spectroscopy.

[165] «Perkinermer FTIR spectrometer,» [Online]. Available: https://www.wardsci.com/store/product/8888413/spectrum-twotm-ftir-spectrometer-software.

[166] R. Ridwan, A. R. Prabowo, N. Muhayat, T. Putranto e J. M. Sohn, «Tensile analysis and assessment of carbon and alloy steels using fe approach as an idealization of material fractures under collision and grounding,» *Curved and Layered Structures,* vol. 7, n. 1, pp. 188-198, 2020.

[167] «MTS machine 370.25 Landmark Load Frame,» [Online]. Available: https://www.mts.com/en/products/materials/dynamic-materials-test-systems/landmark-servohydraulic.

[168] «Instron 5582,» [Online]. Available: https://www.hydraulicuniversaltestingmachine.com/tag/instron-5582.

[169] «Instron Ceast 9350,» [Online]. Available: https://www.instron.com/en-in/-/media/literature-library/products/2014/07/upgrade-your-drop-tower.pdf.

[170] «CAI test tool,» [Online]. Available: https://www.zwickroell.com/industries/composites/compression-after-impact-cai/.

[171] M. T. M. Khairi, S. Ibrahim, M. A. M. Yunus e M. Faramarzi.

[172] V. Triminì, S. Varetti, G. Percoco, S. G. Corvaglia, N. Gallo e I. Scavo, «Evaluation of the influence of process parameters on crystallinity and tensile strength of 3D printed PEEK parts,» *Proceedings of the Institution of Mechanical Engineers, Part C: Journal of Mechanical Engineering Science,* p. 09544062231198784, 2023.

[173] W. Z. Wu, P. Geng, J. Zhao, Y. Zhang, D. W. Rosen e H. B. Zhang, «Manufacture and thermal deformation analysis of semicrystalline polymer polyether ether ketone by 3D printing,» *Materials Research Innovations,* vol. 18, n. sup5, pp. S5-12, 2014.

[174] J. Han, J. Tong, X. Tian, L. Xia e D. Ma, « Thermal simulation and warping deformation experimental study of peek in material extrusion,» *Macromolecular Theory and Simulations,* vol. 30, n. 2, p. 2000055, 2021.

[175] A. Moustaghfir, E. Tomasella, E. Bêche, J. Cellier e M. Jacquet, «Adhesion of ZnO and Al2O3 coatings on polycarbonate,» *Plasma Processes and Polymers,* vol. 4, n. S1, pp. S359-S363, 2007.

[176] A. Wilson, I. Jones, F. Salamat-Zadeh e J. F. Watts, «Laser surface modification of poly (etheretherketone) to enhance surface free energy, wettability and adhesion,» *nternational Journal of Adhesion and Adhesives,* vol. 62, pp. 69-77, 2015.

[177] «Online Protractor,» [Online]. Available: https://www.ginifab.com/feeds/angle_measurement/.

[178] A. Al Khatib, R. Le-Franc, J. P. Guin e J. F. Coulon, «Investigating the thermal effects of plasma surface treatment on crystallinity and mechanical behavior of PEEK,» *Polymer Degradation and Stability,* vol. 216, p. 110500, 2023.

[179] T. J. Coogan e D. O. Kazmer, «Prediction of interlayer strength in material extrusion additive manufacturing,» *Additive Manufacturing,* vol. 35, p. 101368, 2020.

[180] T. J. Coogan e D. O. Kazmer, «Healing simulation for bond strength prediction of FDM,» *mRapid Prototyping Journal,* vol. 23, n. 3, pp. 551-561, 2017.

[181] M. Benedetti, A. Du Plessis, R. O. Ritchie, M. Dallago, N. Razavi e F. Berto, «Architected cellular materials: A review on their mechanical properties towards fatigue-tolerant

design and fabrication,» *Materials Science and Engineering: R: Reports,* vol. 144, p. 100606, 2021.

[182] S. A. Tyagi e M. Manjaiah, «Additive Manufacturing of Titanium-Based Lattice Structures for Medical Applications – A Review,» *Bioprinting,* vol. 30, p. e00267, 2023.

[183] S. Varetti, «Study and development of an innovative L-PBF demonstrator and an anti-ice solution based on trabecular structures,» 24 03 2021. [Online]. Available: https://iris.polito.it/handle/11583/2836780.

List of Tables

List of Figures